3.1 Introduction

The AA7075 is an age-hardenable alloy of the 7xxx series, which is not only technologically important, because of its high specific strength, but also scientifically fascinating due to ageing-assisted transition precipitation. Literature reported an inseparable relationship between the nature of precipitates (size, shape, morphology, orientation, volume fraction, and density) and the mechanical properties of the alloys subjected to aging treatments. Therefore, understanding the nature of precipitates is primitive before applying the alloys in industrial applications. Precipitation sequences, nucleation, and growth behaviors of the equilibrium and metastable precipitates were widely reported in the 7xxx series of Al-alloys. For instance, Kartz et al. [143], reported precipitation sequences in terms of vacancy-rich clusters as: *SSSS (α)- VRC- η' ($MgZn_2$)- η ($MgZn_2$)*. The combined work of Berg et al. [48], Stiller et al. [47], and Jiang et al. [144], suggested precipitation sequence in terms of the solute and vacancy-rich clusters as: *Solid solution (α)-GP-I zone (SRC)-GP-II zone (VRC)- η' ($MgZn_2$)- η($MgZn_2$).* On the other hand, precipitation sequence with a higher Zn/Mg ratio (≥2) was reported as SSSS (α)-GP zone (coherent)-η' (semi-coherent)-η(in-coherent)[18,145–147]. The alloys with a lower Zn/Mg ratio (≤2) form the coherent body-centered tetragonal T phase which changes the precipitation sequences as *SSSS (α) -GP zones - T' or η' and T or η* [35].

Among all the transition (*GP zone, η'*), and equilibrium (*η*) precipitates, the *GP zones* display two variants, GP-I (solute-rich clusters, Mg rich), and GP-II (vacancy-rich clusters, Zn rich). The combined work of Sha et al. [46], Bendo et al. [148], Godard et al. [149], and Chung et al. [68], displays 4, and13 variants of the η'($MgZn_2$, $η'_{1-4}$), and η ($MgZn_2$, $η_{1-11}$), respectively. The stacking structures in the $η_1$, and $η_2$ types of precipitates were analyzed, by Bendo et al. [148] , Marioara et al. [150] , and the Xu et al. [151], in the Al-Zn-Mg-Cu alloys.

They found that η_1 and η_2 possess the zig-zag C14 (...RR^{-1} RR^{-1}….) type atomic configurations. Here, R is the rhombic unit. On the other hand, R^{-1} depicts the inversely projected rhombic units. Chung et al. [74] studied the structures, and growth mechanisms of the η precipitates in creep age formed 7050 Al-alloy using the Cs corrected HRTEM imaging in STEM mode. The layer-by-layer growth of η precipitates, which was supplied with the precursor, e.g. Zn, Cu, and Mg solute atoms. The AA7075T7352 is an over-aged, precipitation-strengthened 7075 Al-alloys designed to obtain the high work hardening exponent (n), as well as the UTS/ YS ratio, which is the strong function of the precipitation process. The nucleation, and growth behaviors of phases, precipitation process, and associated defect structures during their formation, and phase transformation were not revealed for AA7075T7352. Therefore, one part of this chapter is attributed to the study of the nucleation and growth behaviors of precipitates, their nature, and the precipitation process in AA7075T7352 using the transmission electron microscope.

The appropriate design of heat treatments (under-aging T4, peak aging T6, over-aging T73, and retrogression and re-aging (RRA)) [47,87,152], combinations of deformation, and heat treatment [20,31,153], are some of the methods used to modify the precipitation characteristics for improving the performances of the alloy. The former alters the precipitation process (size, shape, and distribution) [25,154,155]. Whereas, the latter helps attain the desired properties by changing the nature of precipitates, and microstructures [21,31,156]. Therefore, it is worth studying the nature of precipitates in the T4, T6, and T73 tempered 7075 Al alloys.

The heat treatments, and heat treatment followed by deformation also promote texture development which influences the mechanical properties, however effect of texture in heat-treated specimens is less than the deformed one. Chen et al. [31], reported Cube {001}<100>,

Goss {011}<100>, and P{011}<122> recrystallization texture, and α-fiber in peak-aged 7xxx series Al-alloy. Nayan et al. [157], and Liu et al.[158], reported deformation textures e.g. Goss{011}<100>, S{123}<634>, and Cu{112}<111>, after cross rolling and asymmetric rolling in AA2195 and AA2524 and . Zhang et al. [159], and Nayan et al. [157], reported recrystallization textures, e.g., Goss {011}<100>, Cube {001}<100>, and P {011}<122> textures [159], adopted by the combinations of both deformation and heat treatments.

Due to thermal gradients, and precipitation, residual stress also develops after heat treatments [160]. For, instance, Sun et al. [161], reported a 10.5% reduction in residual stress due to artificial ageing at 120°C for 15 h. Robinson et al. [13], found enhanced residual stress with an increasing cooling rate in 7449 Al alloy. Moreover, reduction was noticed, while increasing the coolant temperature in the same alloy. Peak ageing of alloy (120°C for 48 h) further gives reduced residual stress of ~8%, while the overaged sample shows a reduction of about ~5%. Residual stress severely influences the strength, fatigue, and stress corrosion cracking (SCC) resistance significantly [13,161,162]. However, residual stress data are not available for 7075 Al alloy for under-ageing (T4), peak-ageing(T6), over-ageing (T73) as well as T7352 temper. Therefore, it is necessary to measure the residual stress of 7075 Al alloy under different tempered conditions. The peak aged (T6) 7017 Al-alloy displays fine (5 nm) η' precipitates in the matrix, and coarse (36 nm) η precipitates in the grain boundary, without any precipitation-free zone (PFZ) that results in a high yield strength of 546 MPa [88]. The over-aged (T7) alloy shows coarsened (10 nm) η' precipitates in the matrix and η precipitates of 90 nm size in grain boundaries with wide PFZ, thus reducing the yield strength of 460 MPa [88]. Highly over-aged (T73) alloy further reduces yield strength to 385 MPa [88]. Even though the mechanical properties of many 7xxx alloys are reported

[88,163–167], very limited information about the tensile properties of 7075 Al is available in the literature. Therefore, it is essential to study the tensile properties of 7075 Al alloy in its T4, T6, and T73 tempered conditions for the structure-property correlations.

Tensile flow, and work hardening behavior of hot cross-rolled AA7010 Al-alloy, and peak-aged conditions are studied [168]. Both the Ludwigson and a generalized Voce–Bergström relation display work-hardening behaviors of alloy. However, the uniform elongation is overestimated by the Ludwigson fit but severely underestimated in the peak-aged state [168]. Peak-aged material follows Ludwigson behavior, but hot rolled sheet displays Voce-Bergstrom [168]. The work-hardening behavior of 7075Al was analyzed at different temperatures (25-300°C) using the Kocks-Mecking and Crussard-Jaoul models [169]. Flow curves in hardening regimes were predicted using constitutive models [170–174]. The plastic deformation of AA7075 Al alloy was dominated by one slope of stage III in the Kocks-Meck plot [126,169]. Work hardening behavior of aged 7075 Al alloys of different stages are essential for plastic deformation, but detailed flow behavior is not available. Therefore, it is important to study the flow behavior of 7075 Al alloy of T4, T6, and T73 tempered conditions. Therefore, the second part of this chapter deals with studying the nature of precipitates, determination of residual stress and texture, tensile properties, flow, and work hardening behaviors of 7075 Al alloy in the T4, T6, and T73 tempered conditions to find structure-property correlations.

The alloys employed in the cyclic loading environments as airframe structural components also require a precise study of dislocation behavior, on the account of strain and temperature. The dislocation behavior of the cubic close-packed metallic systems was well investigated in the literature. For instance, the evolution of the dislocation tangles, slip band, planar array of dislocations, dense dislocation walls (DDWs~), dislocation cell (DC) structures,

geometrically necessary dislocations (GNDs~) in Al-Mg-Si alloy. Dynamic strain aging behaviors of the 7xxx series alloy were studied [175]. Various aspects of the precipitate growth and their dissolutions have been reported in some of the work [176–178]. One of the recent works has also proven that tensile stress decelerates the coarsening of the precipitates, whereas, compressive stress accelerates the diffusion of the solute atoms thereby allowing the growth of precipitates [179]. Changes in precipitation kinetics, after stress-aging response, were studied [179], and it was found that the precipitate density in the peak-aged alloy was higher than in the traditional aging state. Further, two-slope deformations characteristics are reported in 7xxx series Al-alloys [90], as well as in the Ni-based super-alloys [180,181]. Formation of dislocation loops/ forest dislocation/ accumulated dislocation seems to be the characteristics of low to medium strain hardening exponent [92, 93, 95].

In contrast, the dislocation tangles, slip band, dislocation cell, and Taylor lattice structures are observed in the alloy of the medium to high strain hardening exponent [92, 95, 96]. Hence, many of the precipitate variants and dispersoids observed in the 7xxx series Al-alloys [135,182,183], their size, shape, morphology, and orientations may have strong influences on the nature of deformation and the stress corrosion cracking performances [45,46,48,183]. Therefore, materials subjected to monotonic or cyclic loadings during practice require characterization of the dislocations and the resulting precipitation behaviors [184–186].

The aforementioned literature review and a plethora of research work carried out by a few other groups [147,175–177,179] indicate that enough studies are available related to microstructures and precipitation behavior. However, widespread investigations in terms of the complex interplay of the dislocation structure evolution during tensile straining of the AA7075T7352 aluminum alloy on the strengthening/ hardening mechanisms and deformation characteristics as well as stress corrosion cracking (SCC) performance are

seriously lacking. Therefore, the third part of this chapter deals with some of the issues associated with the nature of precipitation processes, and dislocation structures evolution on account of partial deformation of 2%, 6%, and 10% tensile true strain at room temperature.

In this chapter, the overall studies are divided into three major parts: **the first part** is attributed to the electron microscopy of precipitates in AA7075T7352. In this part, nucleation and growth behavior of precipitates were studied using the bright and dark field TEM imaging, and high-resolution transmission electron microscope (HR-TEM). The chemistry of precipitates was analyzed with the help of the HAADF-STEM imaging technique.

The second part pertains to the dislocation behavior of AA7075T7352, which has been studied with the help of a partial amount of tensile straining of 2%, 6%, and 10% true plastic strain (ε_P).

The third part is related to the comparative precipitation behavior, texture characteristics, and flow behaviors of AA7075 in the under-aged (T4), peak-aged (T6), over-aged (T73), and T7352 tempers.

3.2 Results

3.2.1 Part I Electron microscopy of precipitates in AA7075T7352

Fig. 3.1 shows the XRD pattern of AA7075T7352 Al-alloys. Analyzes of the peaks confirm the presence of the high-intensity peaks (111, 200, 220, and 311) of α-Al (cF4 structures, PDF#85-1327), and less intense crystalline peaks (002, 002, and 004) of the η, η' and η respectively. Added to this, Al_2Cu (θ) intermetallic is also observed.

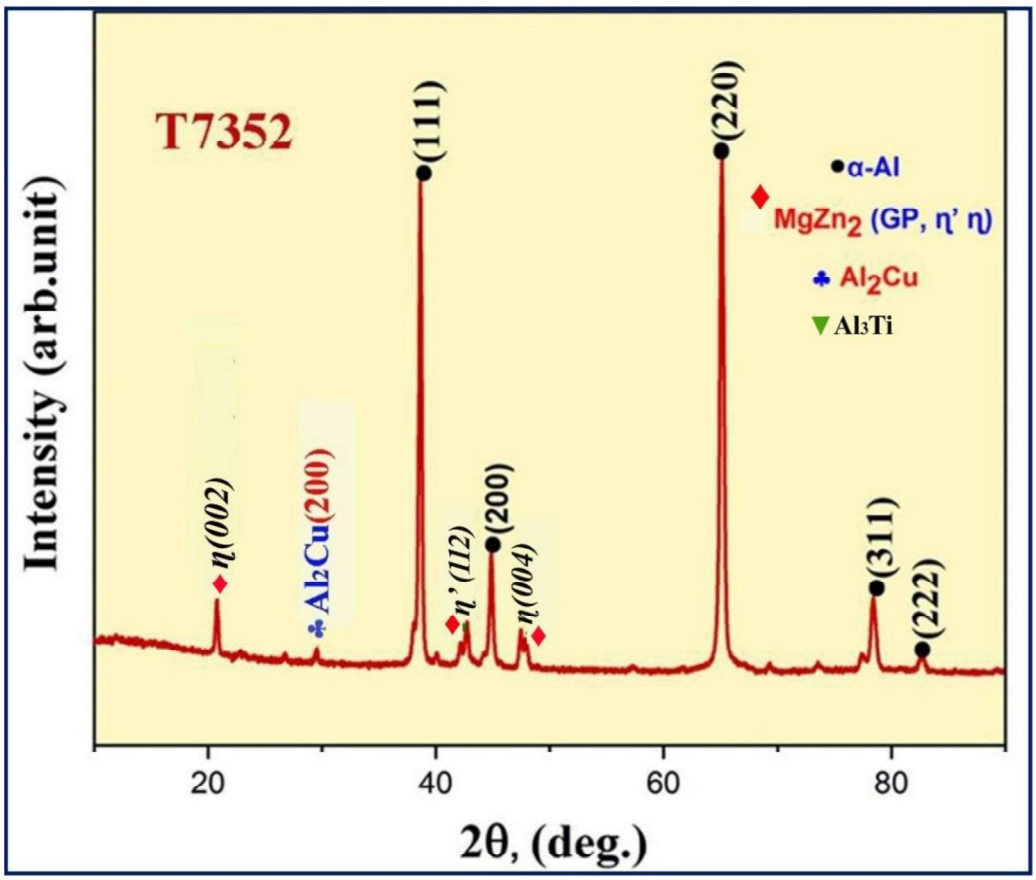

Fig. 3.1. X-ray diffraction patterns of the AA7075T7352 Al-alloy.

Such analysis were performed, on account of the d-spacing value of the major phases, and the JCPDS card number which is given in Table 3.1, along with their crystallographic information.

Table 3.1 d-spacing value of precipitates, and their respective JCPDS card number

SN	d-spacing value(Å)	Phases	Reflection	Space group	Point group	Pearson Symbol
01.	2.33	α-Al F.C.C.	111(PDF# 85-1327)	$Fm\bar{3}m$ (140),	$m\bar{3}m$	cF4
02.	1.43	α-Al F.C.C.	220 (PDF# 85-1327)	$Fm\bar{3}m$ (140),	$m\bar{3}m$	cF4
03.	1.22	α-Al F.C.C.	311(PDF# 85-1327)	$Fm\bar{3}m$ (140),	$m\bar{3}m$	cF4
04.	4.29	$MgZn_2$*(η)*	002 (PDF#65-3578)	$P6_3/mmc$ (194),	6/ mmm	hP12
05.	2.12	$MgZn_2$*(η')*	201 (PDF# 77-1177)	$P6_3/mmc$ (194),	6/ mmm	hP12
06.	2.15	$MgZn_2$*(η)*	004 (PDF# 77-1177)	$P6_3/mmc$ (194),	6/ mmm	hP12
07.	2.82	Al_2CuMg	022(PDF#652504)	Cmcm (63)		oS16
08.	1.41	Al_3Zr	220(PDF#65-2750)			

The α-Al belongs to the space group and point group symmetry of $Fm\bar{3}m$ (140), and $m\bar{3}m$ respectively, and is denoted by the Pearson symbol of the cF4 structure class. On the other hand, η' and η belong to the Laves phase ($MgZn_2$) of C14 type and relate to the space-group, and point-group symmetry of $P6_3/mmc$ (194), and 6/ mmm alternatively, which is denoted by the Pearson symbol of hP12 structure class. The Al_2Cu phase refers to the space group and point group symmetry of I4/mcm (140), and 4/mmm alternatively which was denoted by the Pearson symbol of tI12. The Al_2CuMg phase belongs to the space group of Cmcm (63) and is denoted by the Pearson symbol of oS16. The crystallographic information of precipitates as well as intermetallic are given in Figs. 3.2 a-d.

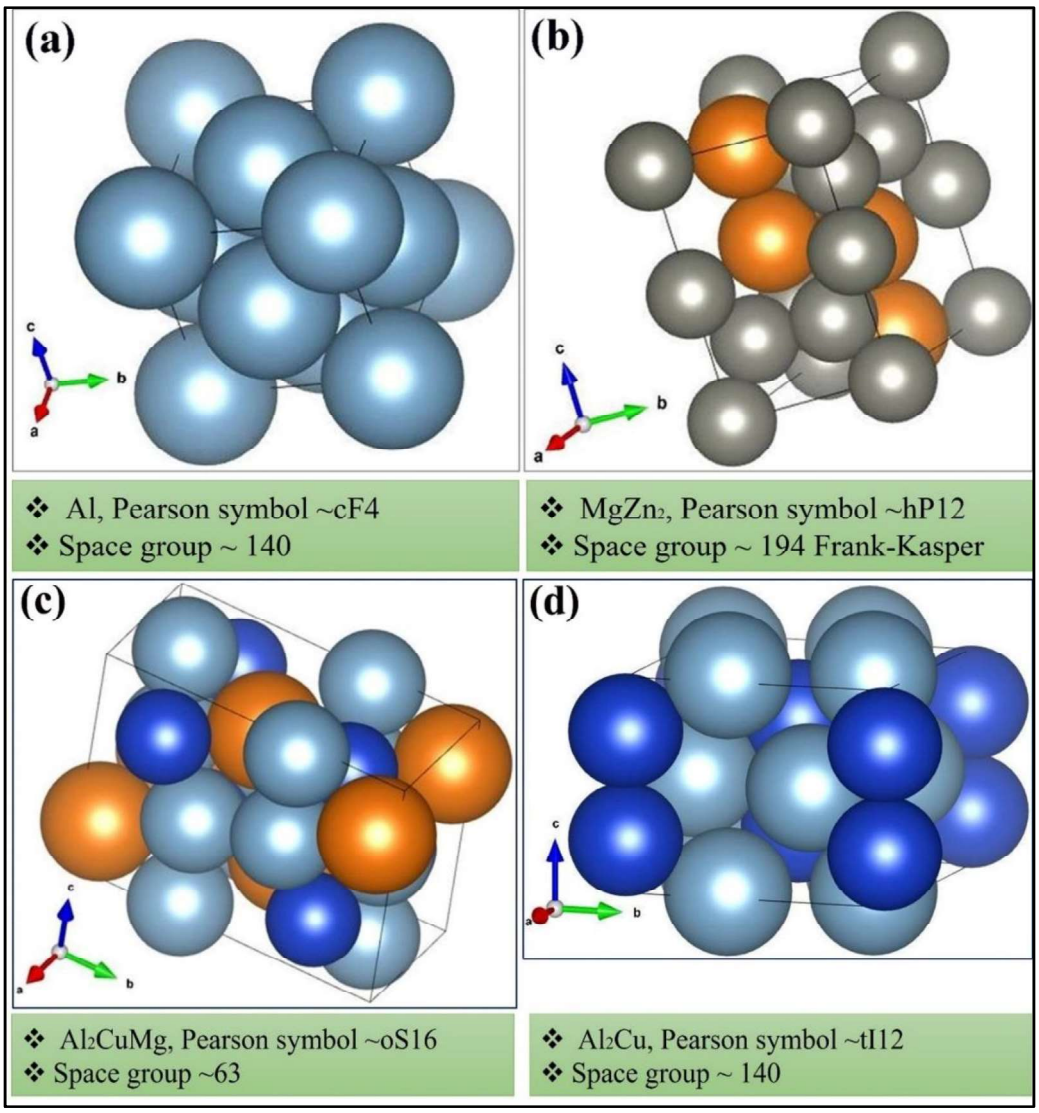

Figs. 3.2 a-d Lattice position of the cubic α-Al (a), hcp structures $MgZn_2$ (b), Al_2CuMg (c), an Al_2Cu phase (d).

Fig. 3.3a shows a bright-field TEM image, from one of the regions along 111 zone-axis of α-Al. the rod type η precipitates and strip morphology showing preferred orientation along 110 of α-Al are noticed in addition to the presence of dislocation in some of the regions. Corresponding SAEDPs~ are given in Fig. 3.3b. Sharp spots of α-Al <220> with six-fold symmetry, and weak spots attributed to η' and η precipitates are noticed. Streaking along 110 of α-Al is another notable feature in this, which indicates the presence of stacking fault

in alloys. Fig. 3.3c shows a dark field TEM micrograph, from weak spot DF-1, very close to $20\bar{2}$. Presence of rod type η' precipitates (Length = 76±9 μm, Width =52±6 μm) which join together along 110 of α-Al, and form new precipitates (total 7 precipitates, with nearly the same dimension) along the faces. Some precipitates are also joined across the interface and form a bigger precipitate by changing the lattices at the adjoining interface. Fig. 3.3d shows dark field TEM images, from the less intense diffuse spot DF-2. Plate/ strip type precipitates with average size of (L= 160±7 nm, W=15±3.5 nm) showing preferred orientation along $1\bar{2}1$ of α-Al is noticed. The length of a few strip-type precipitates shows double multiplicity (2* 160 = 320 nm), along $1\bar{1}0$ of α-Al. Fig. 3.3e shows a bright-field TEM image, from another region along 111 zone axis of α-Al. The presence of rod-type η', preferably oriented along 110 of α-Al, and strip-type precipitates showing preferred orientation along $1\bar{1}0$ of α-Al is observed. Corresponding SAEDPs~ are given in Fig. 3.3f. The presence of sharp DPs of α-Al, <220> with 6-fold symmetry, and weak spots of precipitates are noticed, and weak spots are very close to <220> spots of α-Al.

Fig. 3.3g shows a dark field TEM image from DF-3 (weak spot very close to $20\bar{2}$ of α-Al). The existence of rod-like, η' precipitates with an average length of 205±12 nm, along $1\bar{1}0$ of α-Al, and an average length of 351± 20 nm, along 110, showing in-situ nucleation assisted growth of it. Fig. 3.3h shows a dark field TEM image, from DF-4 (very close to $0\bar{2}2$ of α-Al). The presence of sharp dispersoids of Al_3Zr (DO_3) along with strip type η precipitates showing preferred orientation along $1\bar{1}0$ of α-Al is noticed. The dispersoids display high brightness in the DF-TEM micrograph. The precipitates show structural and micro-structural inhomogeneities in the alloy matrix. Such variation, in the size and shape of precipitates along different orientations is due to variation in activation energy of atomic diffusion arises due to differences in interfacial energy.

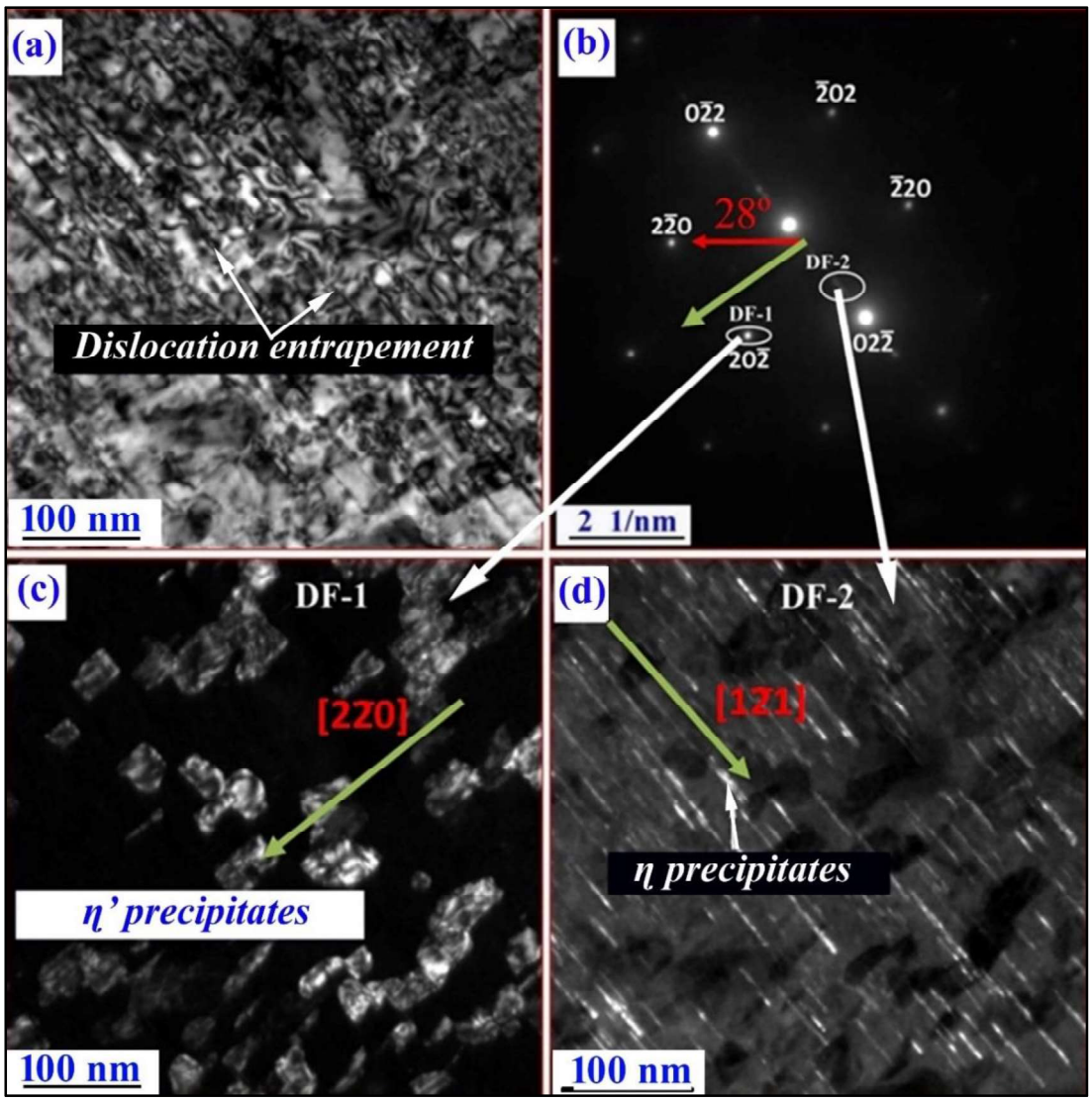

Figs. 3.3a-h. Precipitation behavior: (a)bright-field TEM micrograph, (b)corresponding SAEDP along the $[111]_{Al}$ zone – axis,(c) dark-field TEM micrograph corresponding to diffraction spot DF1, (d)dark-field TEM micrograph from diffraction spot DF-2, (e)bright-field TEM images from another region, (f) corresponding SAEDPs along the $[111]_{Al}$ zone-axis, (g) dark-field TEM images from DF-3, (h)dark –field TEM images from DF-4.

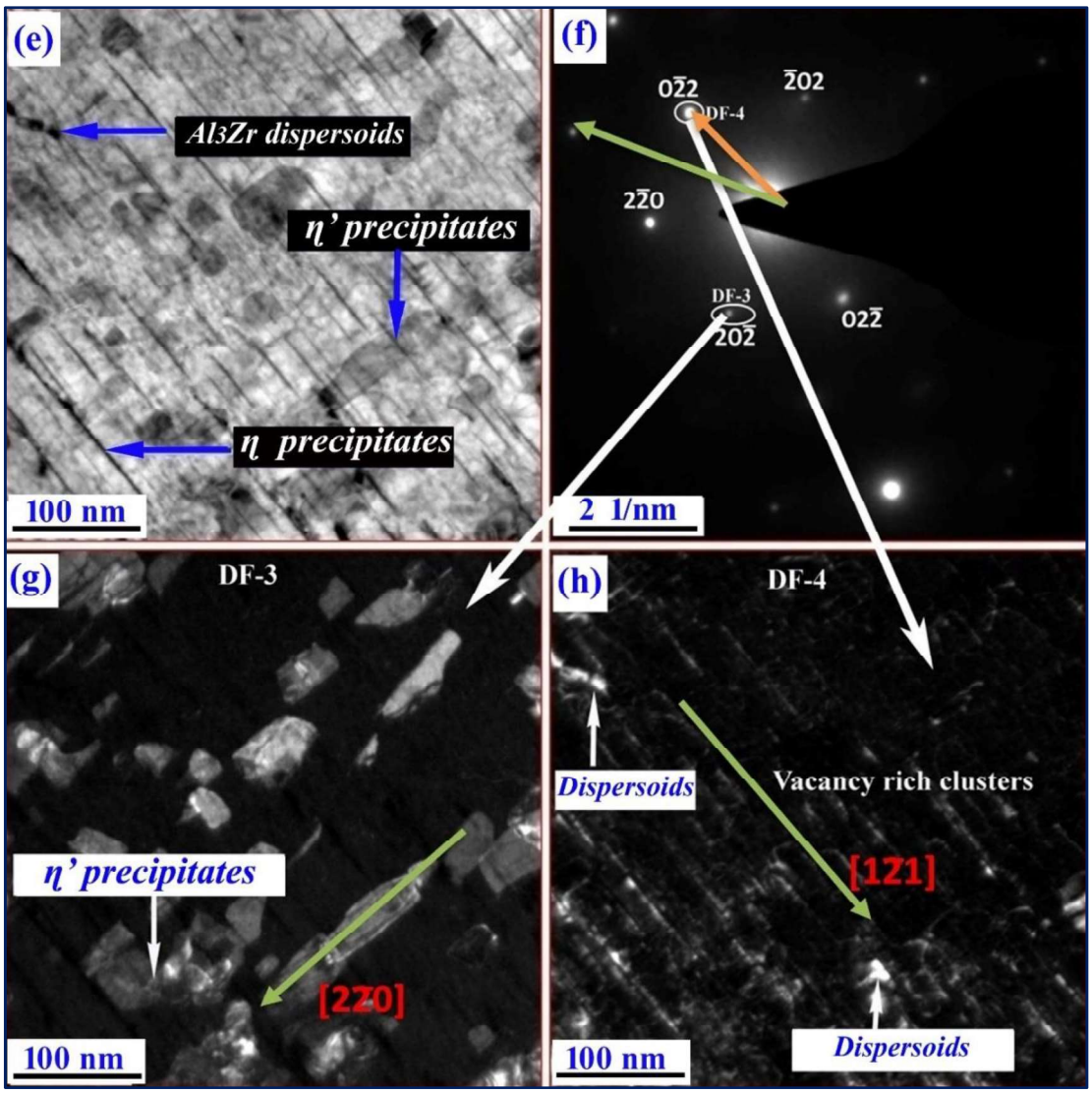

Figs. 3.3 a-h Continued……

Figs. 3.4a-c displays an HRTEM micrograph, from one of the regions of plate shape precipitates. The presence of stacking fault-type features was observed. The lattice spacing between two α-Al 111 lattice matrix fringes is measured to be 2.33 Å. A Fast Fourier Transform (FFT) image from one of the regions is shown in Fig. 3.10b. Streaking along $1\bar{1}0$ of α-Al is observed. This also shows the presence of stacking fault, during nucleation of η precipitates. The region containing stacking fault during nucleation of η precipitate is seen

in the Inverse Fast Fourier Transform (IFFT) TEM image in Fig. 3.10c, which follows the alternate stacking sequences of a-b. The "a" is related to a layer containing the bright contrast and pertains to Zn rich region. Whereas, "b" pertains to the layer with dark contrast and showing the layer rich in Mg one. This also indicates that the 13 layers of η precipitates substitute a total of 12 layers of α-Al. Such internal structures depict full compatibility with η-$MgZn_2$ precipitate. The differences in the d-spacing value of matrix (d~α-Al) and precipitates (d~η- $MgZn_2$) result in the lattice strain/ dislocation, thus forming the stacking fault during nucleation of η precipitate.

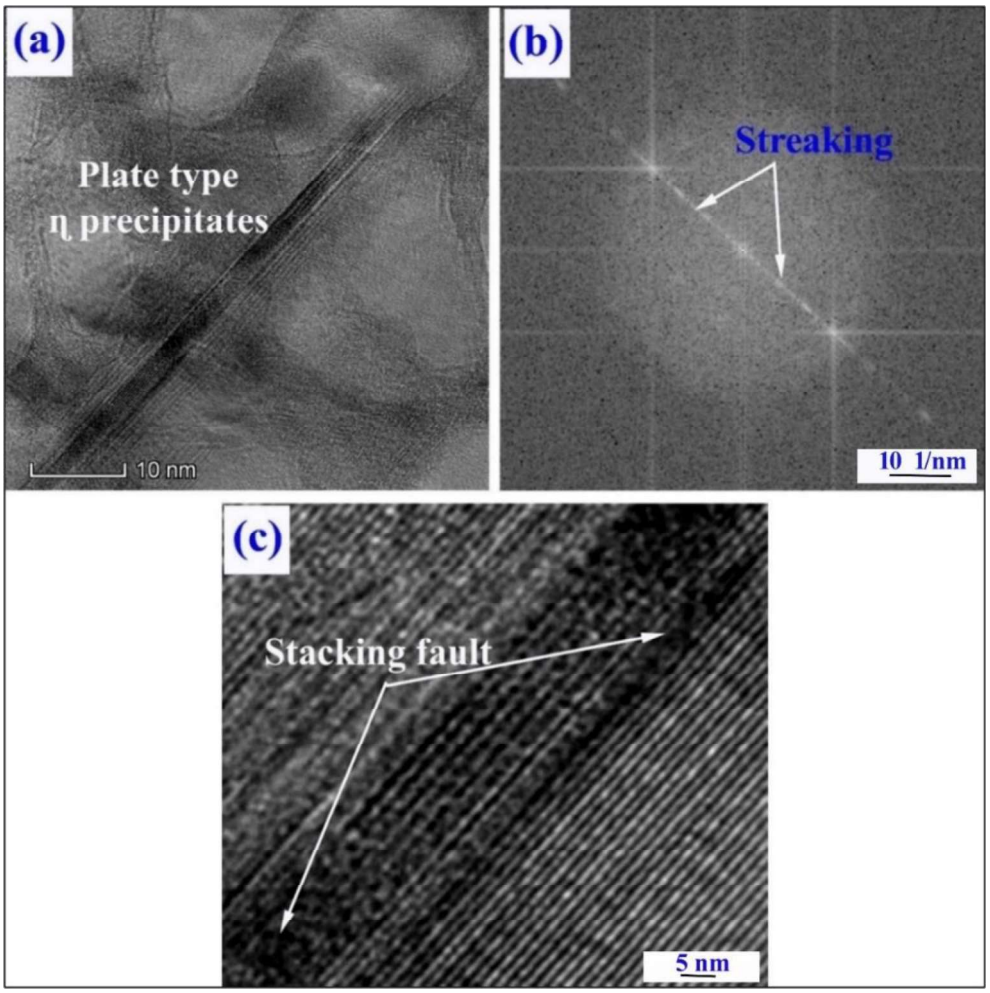

Figs. 3.4a-c. (a) HRTEM image of plate type η precipitate, (b)FFT from the selected region of precipitate, (c) respective IFFT TEM image.

Fig. 3.5a displays high angle annular dark field (HAADF) TEM micrograph of rod type η' precipitates joining at the interface. Their chemistry was analyzed in STEM mode, and shown in Figs.3.5b-c. The presence of a region rich with Zn and Mn is observed, but the magnitude of Mg is more than the Zn. Fig. 3.5d shows the HAADF TEM image of strip type η precipitates. The chemistry was analyzed in STEM mode and demonstrated in Figs.3.5e, f, g. The presence of Mg, Zn, and Zr were noted but precipitates were rich with Zn compared to Mg.

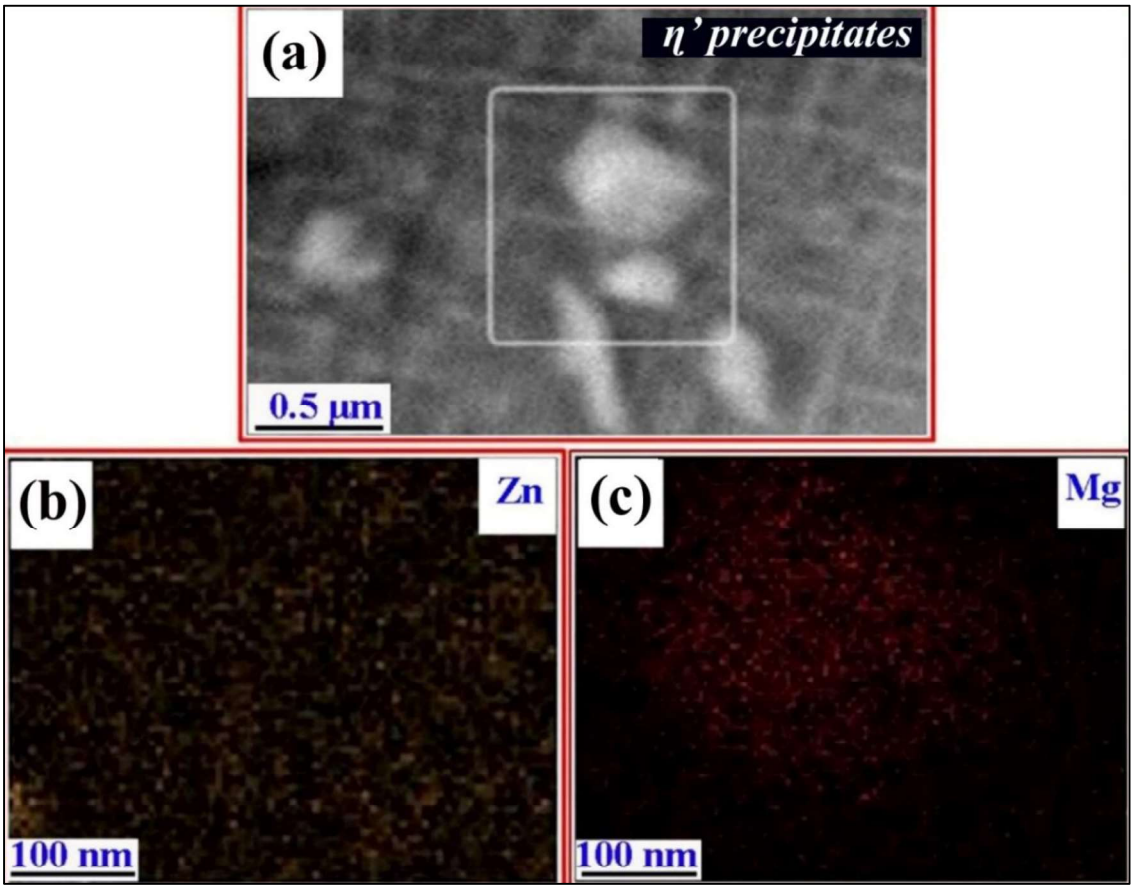

Figs. 3.5a-g. HAADF STEM-EDS of η' and η precipitates: (a) HAADF image of η' precipitates joining in the interface, (b, c) analyzed chemistry in STEM mode, showing Zn map in (b), and Mg map in (c), (d) HAADF image of η phase, (e,f,g) analyzed chemistry in the STEM mode, display Zn rich map in (e), Mg-rich map in (f), and Zr rich map in (g).

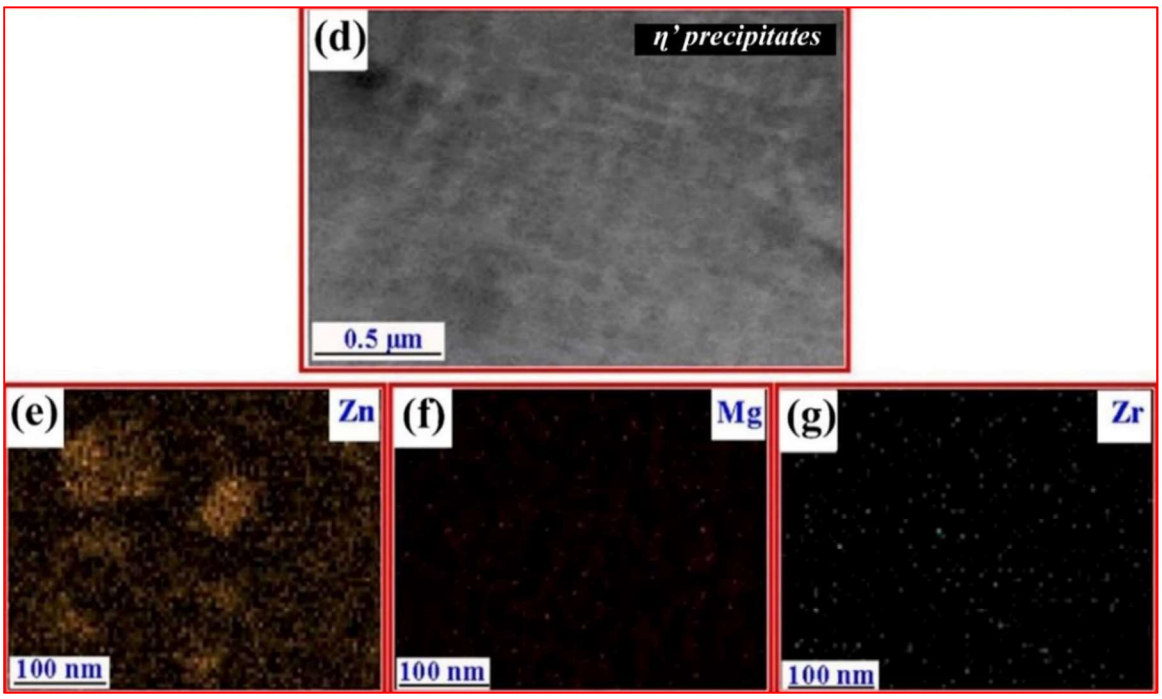

Figs. 3.5a-g. Continued……

Fig. 3.6a shows a bright field TEM micrograph, from another region of specimen along [112] zone-axis of α-Al. The intersecting plate-like η precipitates at 90° and non-intersecting η precipitates are observed in this. Some of the intersecting η precipitates display dark contrast in comparison to non-intersecting η precipitates. The first kind of precipitate shows two different orientations along 110 and $11\bar{1}$ of α-Al. Whereas, second-type precipitates display preferred oriemtation along $\bar{1}10$ of α-Al. Corresponding SAEDPs~ are given in Fig. 3.6b. The sharp spots of α-Al with 4-fold symmetry, and weak spots of η' and η precipitates with 4-fold symmetry are noticed in this. Fig. 3.6c shows a dark field TEM image, from weak spot DF-5. The two differently oriented but intersecting η precipitates along $\bar{1}10$, and $11\bar{1}$ of α-Al, but the average length of precipitates (L_{av}=359±22 nm) along $\bar{1}10$ is more than that of $11\bar{1}$ of α-Al (283±25 nm), showing preferred growth along $\bar{1}10$ of α-Al. Some of the η precipitates with light contrast are parallel along $11\bar{1}$ of α-Al, and the precipitates with bright contrast are parallel along 110 of α-Al. Differently oriented η shows the formation of

precipitate variants. This arises due to differences in interfacial energy during nucleation of precipitates. Fig. 3.6d shows a dark field TEM micrograph, from DF-6. The plate type of η precipitates with average length and width of 144± 5 nm and 43±10 nm is observed. This displays the preferred orientation along $11\bar{1}$ of the α-Al. None of the precipitates joined at the interface, indicating the separated nucleation mechanisms. Fig. 3.6e depicts the bright field TEM image from another region. Differently oriented laths like Al_2CuMg intermetallic and plate type η are observed. Added to this, the presence of dislocation is also seen in some of the regions (marked by a white arrow). Corresponding SAEDPs~ are given in Fig. 3.6f. Sharp spots of α-Al, with 4-fold symmetry, and weak twin spots of η precipitates are noticed. Fig. 3.6g displays a dark field TEM image from DF-7. The plate-like η precipitates are observed. This displays two different orientations along the $\bar{1}10$ and $11\bar{1}$ of a-Al. All of them freely nucleated without joining at the interface. Such observations indicate the separated nucleation mechanisms. The average length of η precipitates along 110 of α-Al is 187±14 nm. The average length of η precipitates along $11\bar{1}$ of α-Al is 160± 10 nm showing preferred nucleation along 110 of α-Al.

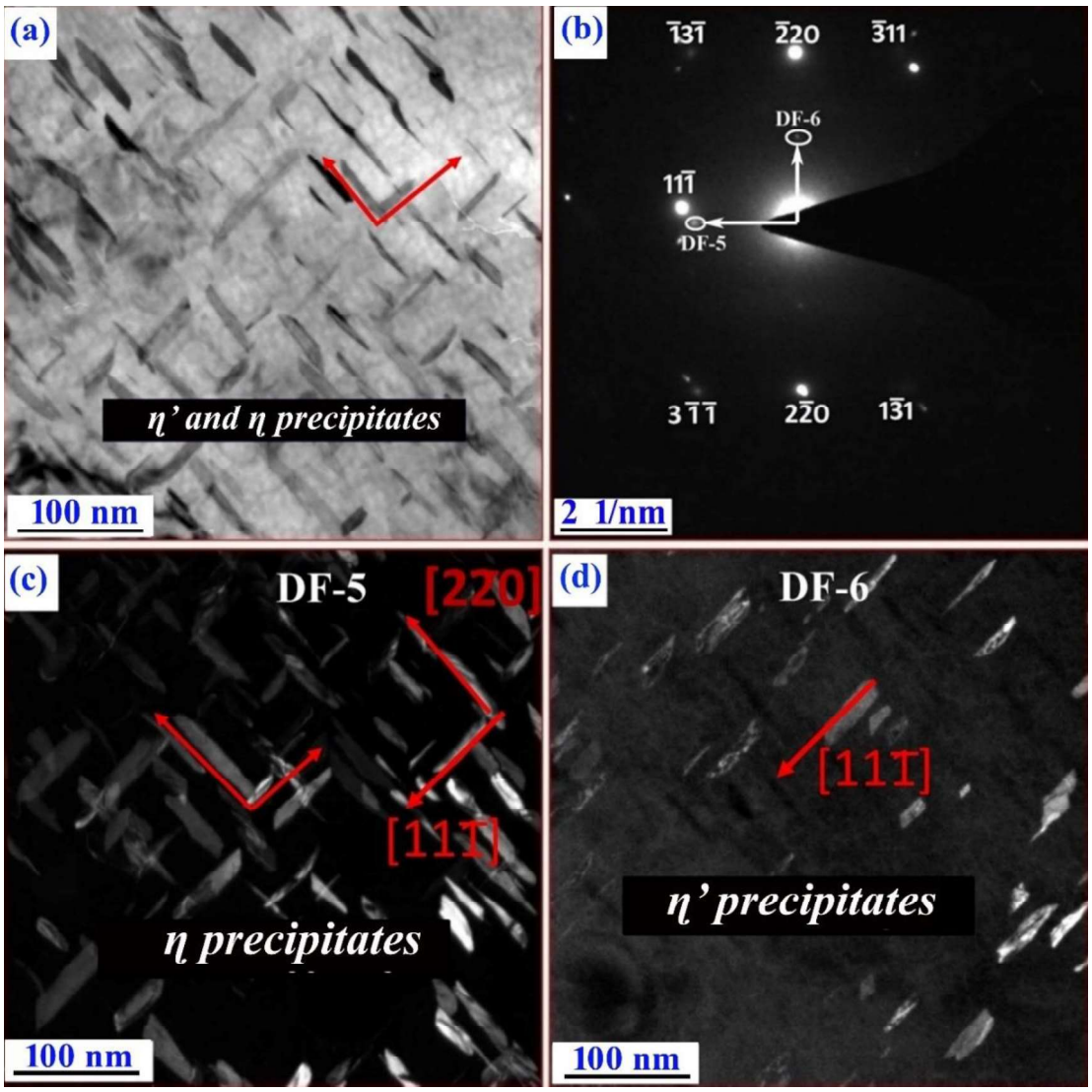

Fig. 3.6a-g Precipitation behavior: (a) bright-field TEM images,(b)corresponding SAEDPs~ along $[112]_{Al}$ zone-axis,(c)dark-field TEM image from DF-5, (d)dark-field TEM image from DF-6, (e) bright-field TEM image from another area, (f) respective SAEDPs~ along $[112]_{Al}$, (g) dark-field TEM image from spot DF-7.

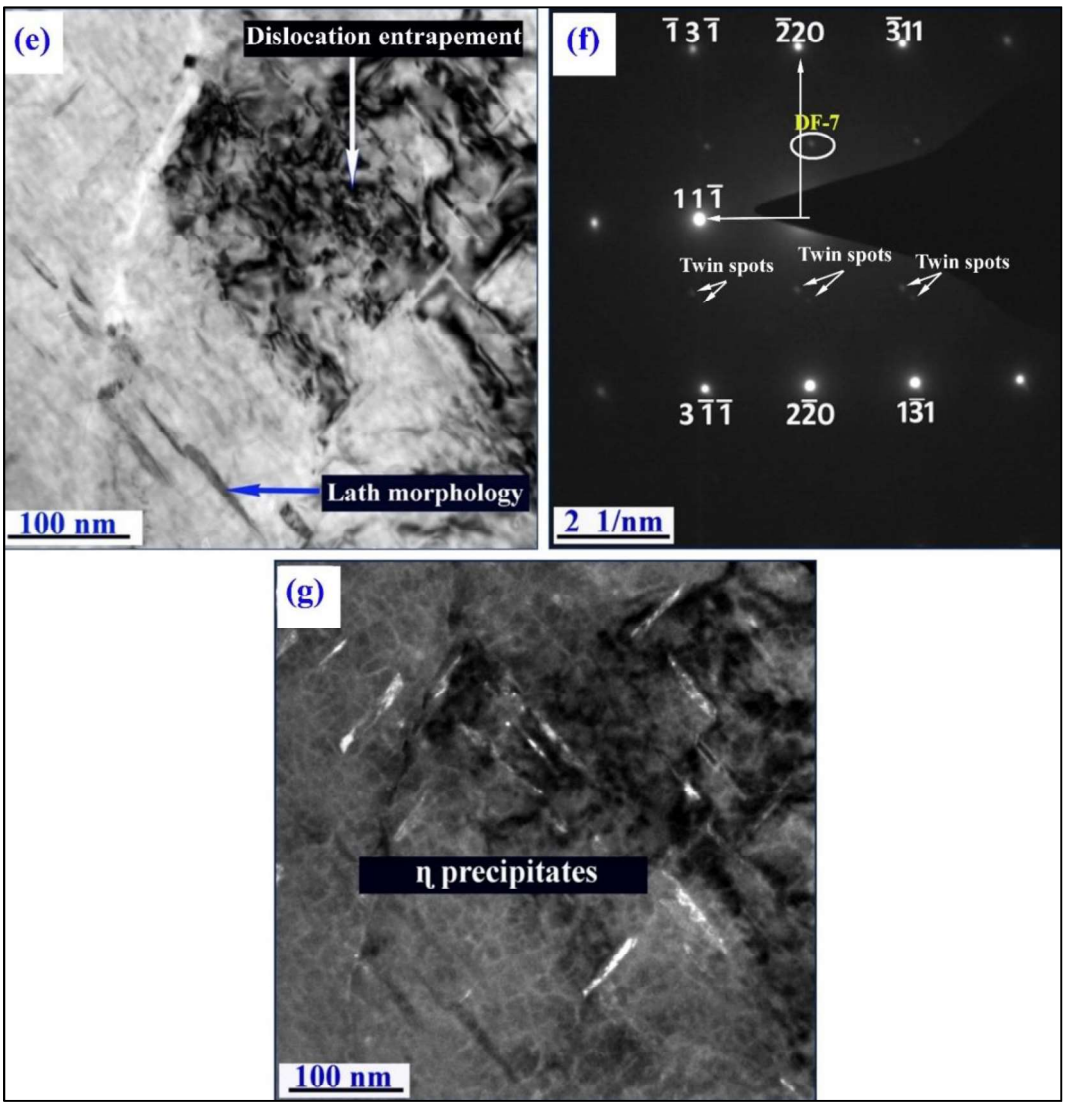

Figs. 3.6a-g Continued……

Fig. 3.7a shows a bright field TEM image, taken from the 110 zone-axis, of α-Al. The existence of lath morphology of Al_2CuMg precipitate is a noteworthy observation. Respective SAEDPs~ are shown in Fig. 3.7b. Sharp spots of α-Al and weak spots of Al_2CuMg are noticed in this. Dark-field TEM image taken from DF-8, a less intense spot, shows lath-like morphology of Al_2CuMg precipitate, displaying preferred orientation along $1\bar{1}1$ of α-Al in Fig. 3.7c, and none of the precipitates are joining at the interface.

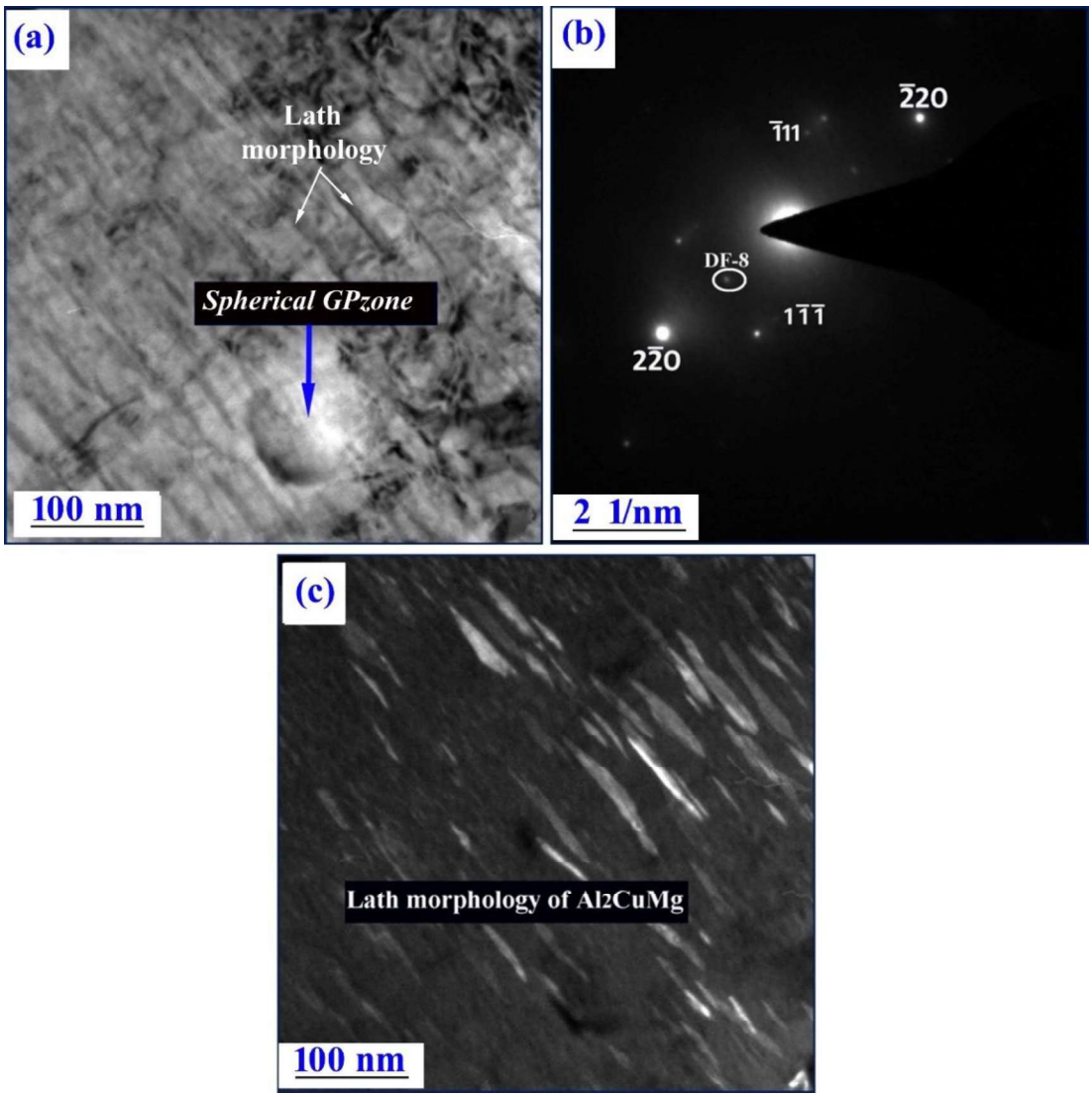

Figs. 3.7 a-c. Precipitation behavior: (a) bright-field TEM micrograph, (b) corresponding SAEDPs along the $[110]_{Al}$ zone axis, (c) dark-field TEM micrograph from diffraction spot DF-8.

Figs. 3.8a-f display STEM EDS area mapping of transition precipitates (*η' (rod), and η (plate)*). The phases rich in Zn, Mg, and Cu are noticed. Added to this, the lean presence of Zr, Cr, Mn, and Fe were also observed.

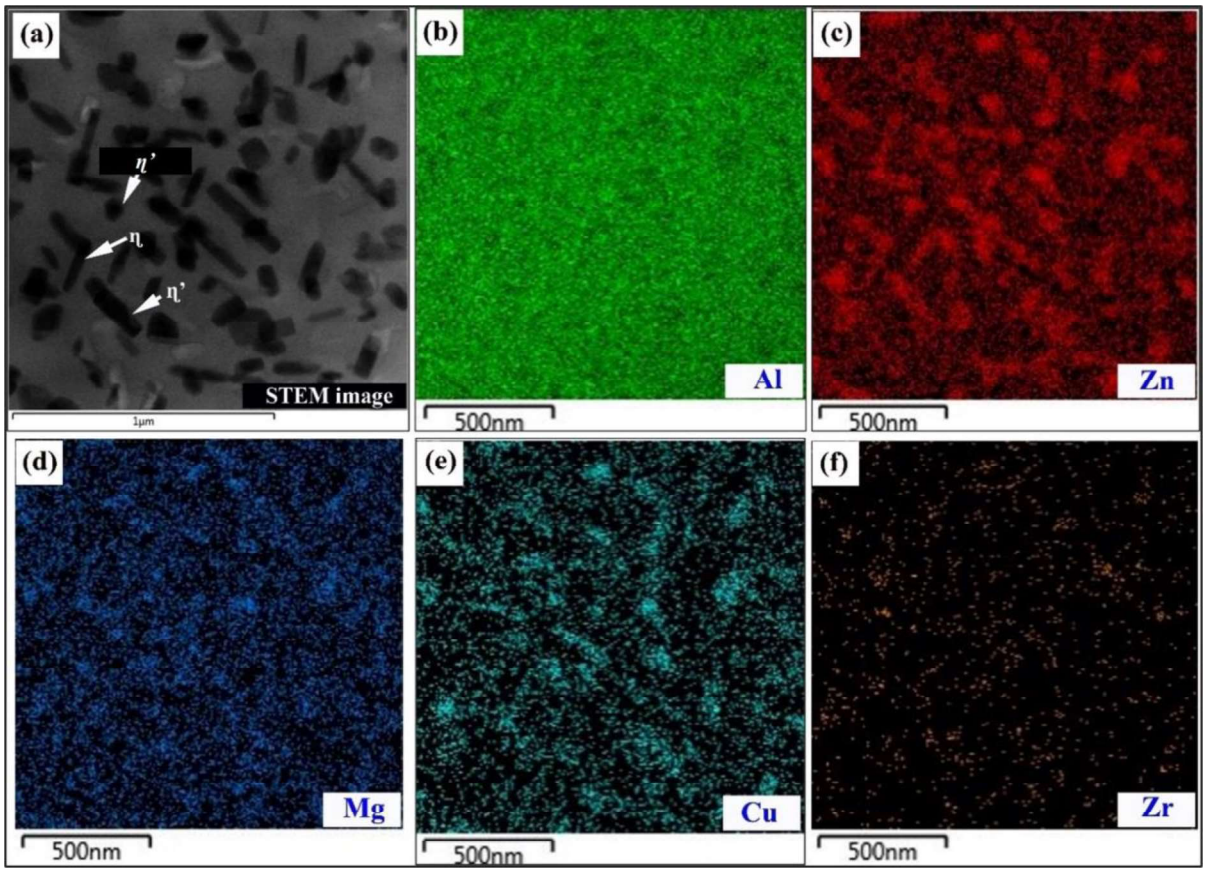

Fig. 3.8a-f STEM EDS area mapping of precipitates in AA7075T7352, the presence of the Zn, Mg, and Cu-rich precipitates are observed.

Fig. 3.9a shows a high-angle annular dark field (HAADF) TEM image from another region of the specimen, containing the η' (rod), and η (plate) precipitates. The overall area is scanned in STEM mode, and the elemental presence of Al, Zn, Mg, Cu, and Zr was observed in Figs. 3.9b-f. Fig. 3.9 g shows the energy count map, from the overall region, which displays a high energy count for Zn, followed by the Mg and Cu. Low energy counts for Mg, Cu, and Zr are also seen, and the analyzed chemical composition is shown in the inset of this figure.

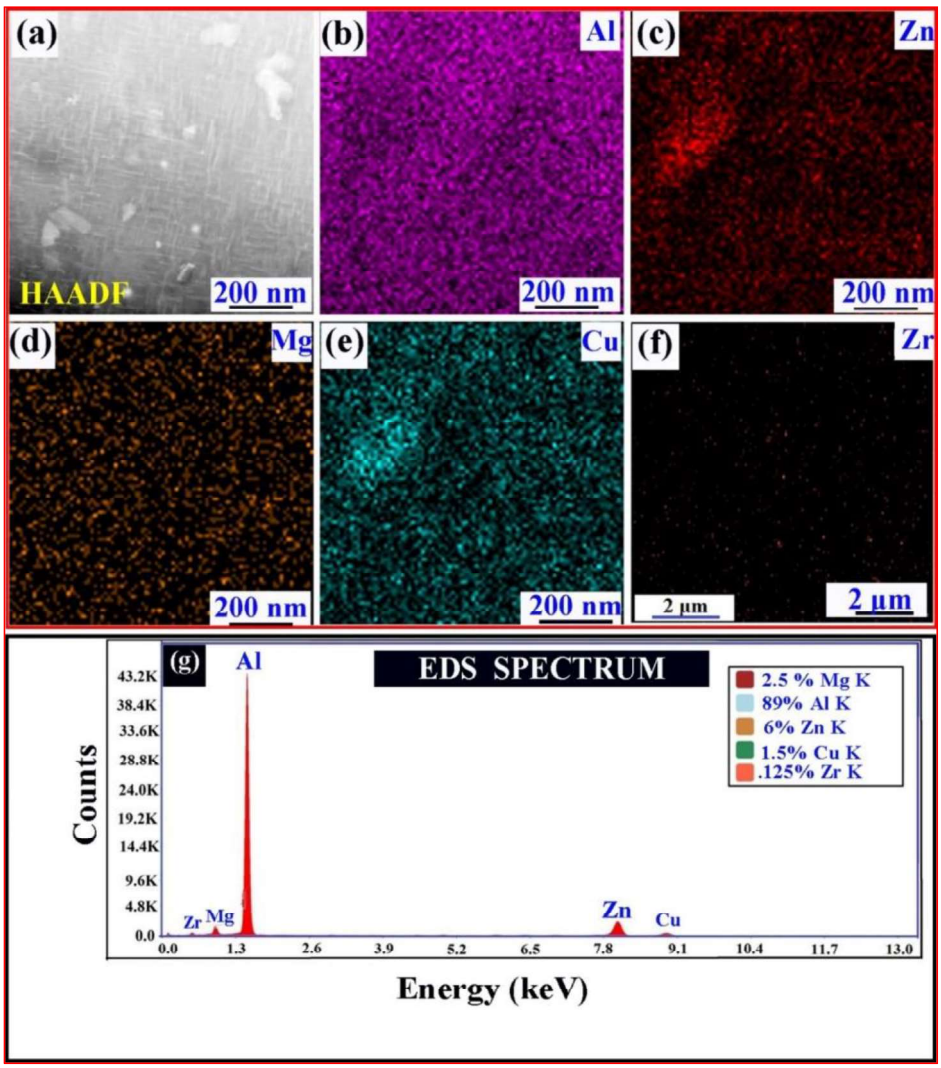

Figs. 3.9 a-g. HAADF STEM-EDS elemental mapping of precipitates in AA7075T7352, from the region consisting of spherical, rod, plate, and lath type precipitates: (a) HAADF Image, (b) Al map, (c) Zn map, (d) Mg map, (e) Cu map, (f) Zr map and (g) energy count map of the region.

Figs. 3.10a shows point spectrum maps of η' (rod) and η (plate) precipitates. The respective chemistry obtained from spectrum 1 is shown in Fig. 3.10b. The chemistry confirms the presence of precipitate rich in Zn, Mg, and Cu, but lean in the Al. Fig. 3.10c shows the chemistry of plate type precipitates showing light contrast, from spectrum 2. These indicate the formation of precipitates rich in Mg, Zn, and Cu, but lean in the Al. However, their magnitude is less than that of spectrum 1. The major finding from this analysis is the presence of Cu in addition to the Mg and Zn in the η' and η precipitates. This indicates the formation of η' and η precipitates with different chemistry, and shows changes in the contrast.

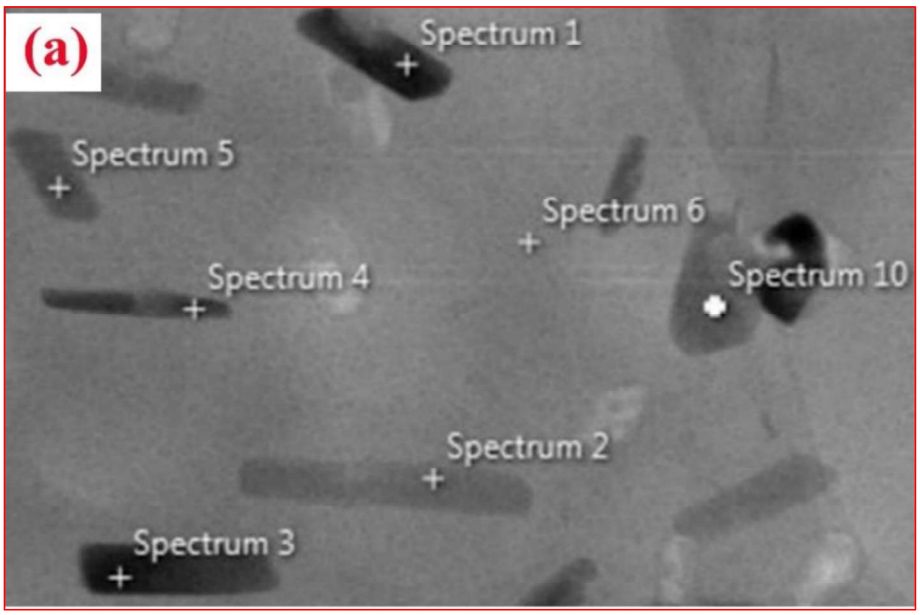

Figs. 3.10a-c Spectrum of precipitates in AA7075T7352 (a), chemistry of spectrum 1(b), chemistry of spectrum 2 (c).

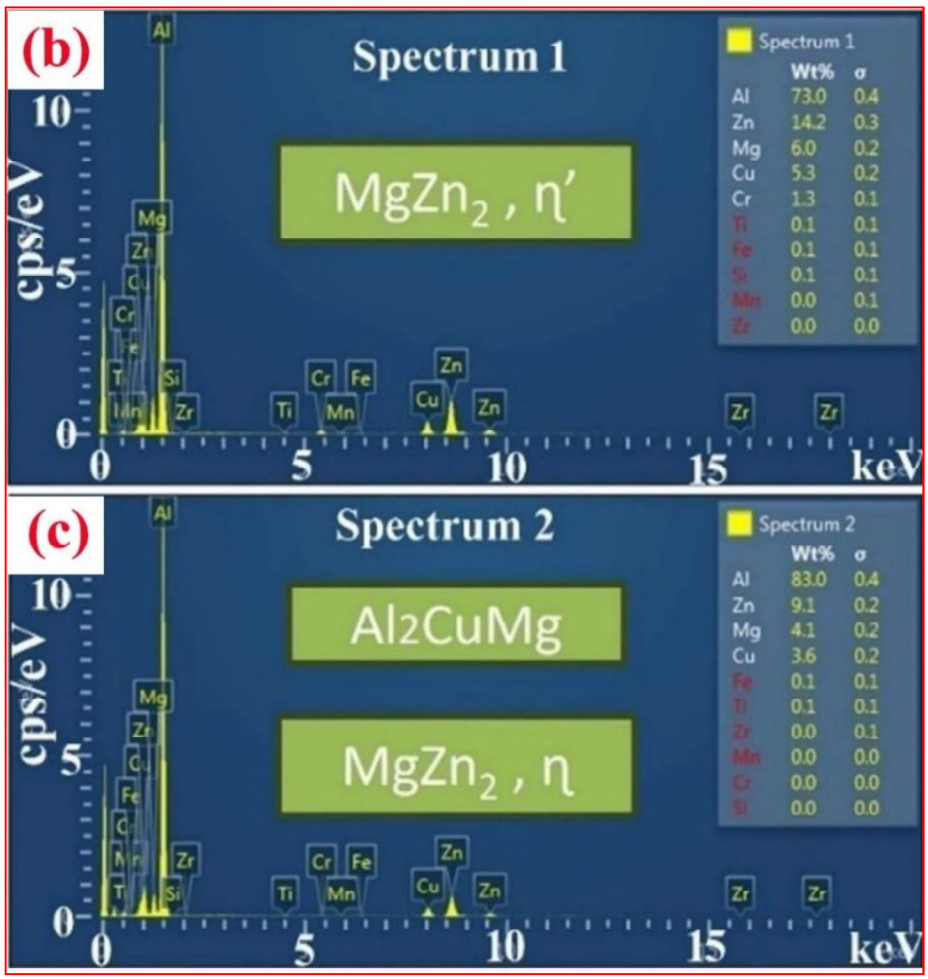

Figs. 3.10 a-c. Continued……

Fig. 3.11a displays an HRTEM image from another area, consisting of the transition precipitates. The presence of rotational Moire fringes is mainly observed. The Moire fringes indicate the presence of lattice misfit/ dislocation in precipitates, therefore showing the formation of precipitates with semi-coherent (η') and in-coherent (η) in nature on the account of lattice misfit between matrix and precipitates. FFT diffractogram from region 1 shown in Fig, 3.11b displays a group of twin spots, which are characteristic features of rotational Moire fringes. The region consisting of the dislocation, and rotational Moire fringes with increased lattice misfit with α-Al matrix were seen in Inverse Fast Fourier transform (IFFT) diffractogram in Fig. 3.11c. Fig. 3.11d depicts the presence of an FFT diffractogram from

region 2, which also shows a group of weak twin spots, displaying the presence of rotational moire fringes. The respective, IFFT pattern shows Moire fringes with less lattice misfit, and pertain to semi-coherent (η') precipitate in Fig. 3.11a-e.

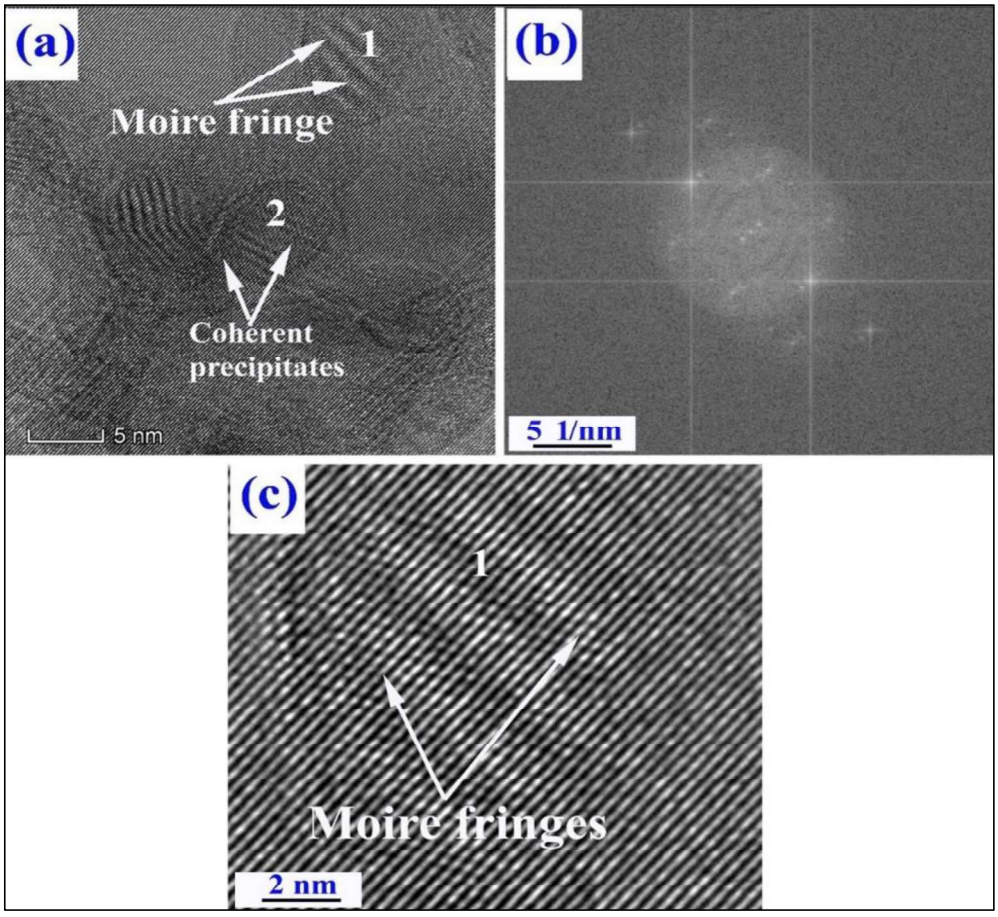

Figs. 3.11a-e HRTEM images of metastable precipitates (a), respective fast Fourier transform (FFT) diffractogram (b), inverse fast Fourier transform (IFFT) (c), FFT from region 2(d), IFFT from region 2.

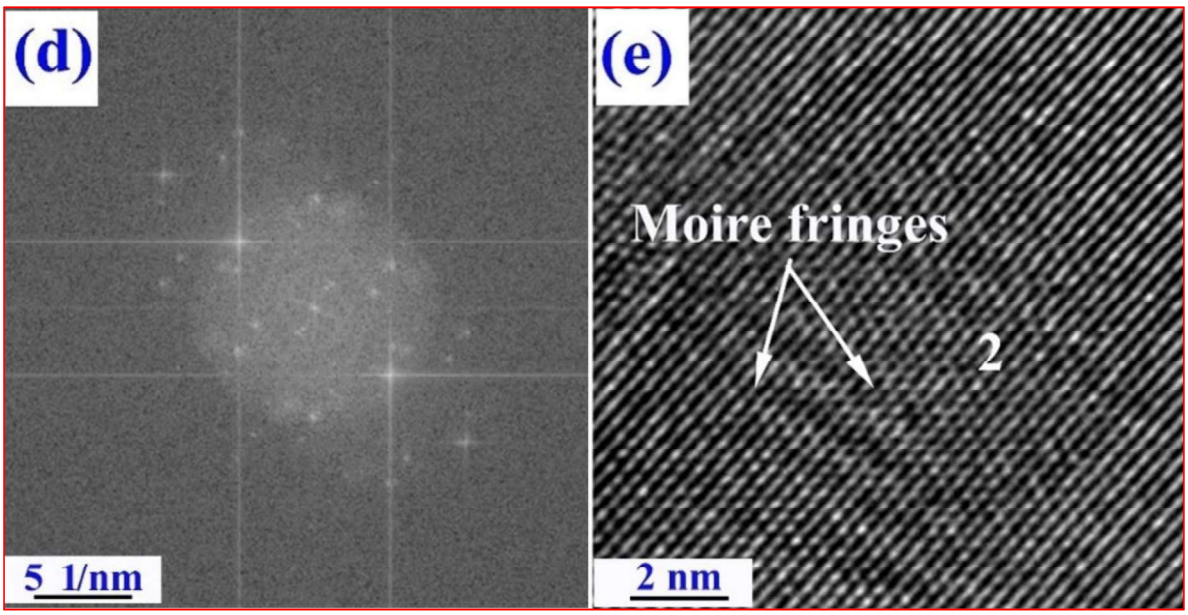

Figs. 3.11a-e Continued…….

3.2.2 Part II Dislocation behaviors of AA7075T7352, after interrupted test at 2%, 6% and 10% tensile true strain

Fig. 3.12a-d shows XRD patterns of as-received, as well as partially tensile strained specimens D2, D3, and D4 respectively. Presences of the solid solution phases of α-Al along with the transition precipitates of $MgZn_2$ (*η' and η*) and intermetallics of Al_2Cu were seen in the as-received state (PFD# 77-1177, 65-3578 and Fig. 12a). At 0.02 tensile true straining, reduced intensity of transition precipitates (GP-Zone and η') are observed, and 111 peak of α-Al is major XRD reflection in Fig. 3.12b. At tensile true strain of 0.06, the absence of the GP zones and reduction in the intensity of η' and η phases were revealed and 200 of α-Al is the Major XRD reflection in this state as displayed in Fig. 3.12c. Re-appearance of the GP-Zone peak at 2θ position of 20° and 44° respectively. Reduction in the intensity of η' and η phases was also seen corresponding to a tensile true strain of 0.1. The 220 of the α-Al is the major XRD reflection in this case, as described in Fig. 3.12d.

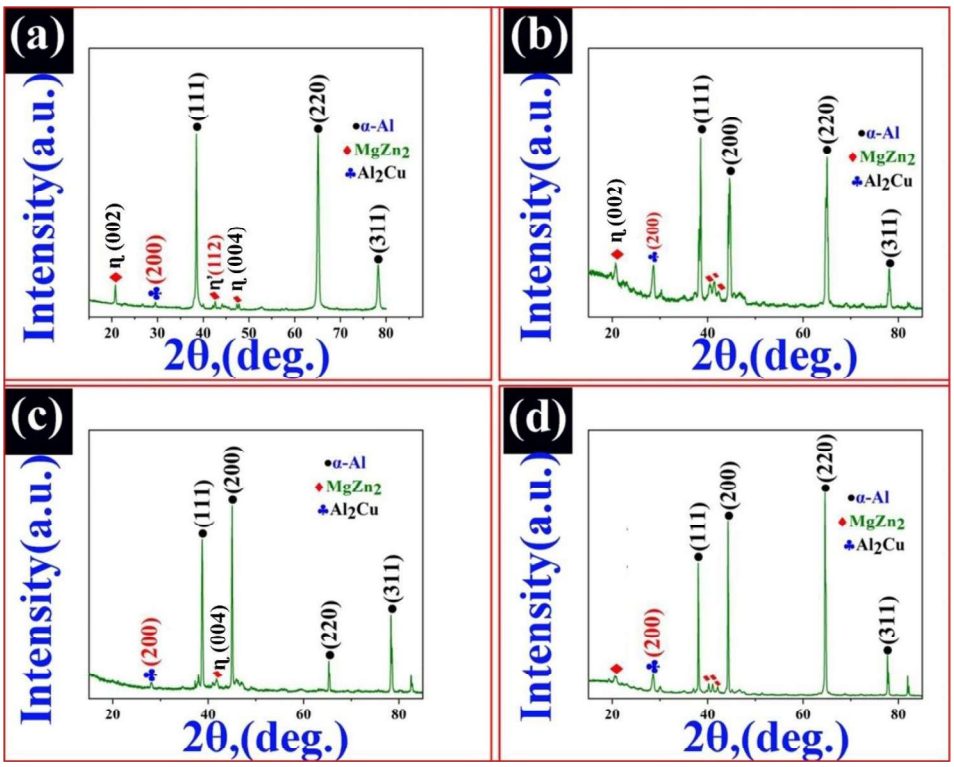

Fig. 3.12a-h. X-ray diffraction patterns of the as received as well as partially tensile strained specimens: (a) as received AA7075T7352 Al-alloy, (b) Partial tensile true straining corresponding to 0.02, (c) Tensile true straining corresponding to 0.06, and (d) Tensile true strain corresponding to 0.1, (e-h) enlarged XRD patterns of the partially deformed specimens between 39º to 44º.

Figs. 3.12 (e-h) displays an enlarged x-ray diffraction (XRD) pattern of the transition precipitates (, η' and η) within 2θ angular range of~ 39° to 43°. High-intensity XRD reflection of all transition precipitates (η' and η) was shown in the as-received state (Fig. 3.12e). Reduced intensity of the η' phases and 2nd–order reflection (002) of η is seen in the XRD pattern of D_2 (Fig. 3.12f). Maximum reduced intensity of η' phase and η (2nd–order XRD reflection of 002) were also clearly shown in D_3 (Fig. 3.12g). Further, evolution of the 2nd-order XRD reflection of η and slightly enhanced intensity of η' phase was observed in D_4 (Fig. 3.12h). There were no significant changes in the intensity of the 2nd peak of η phase in all the above cases (Figs. 3.12e-h).

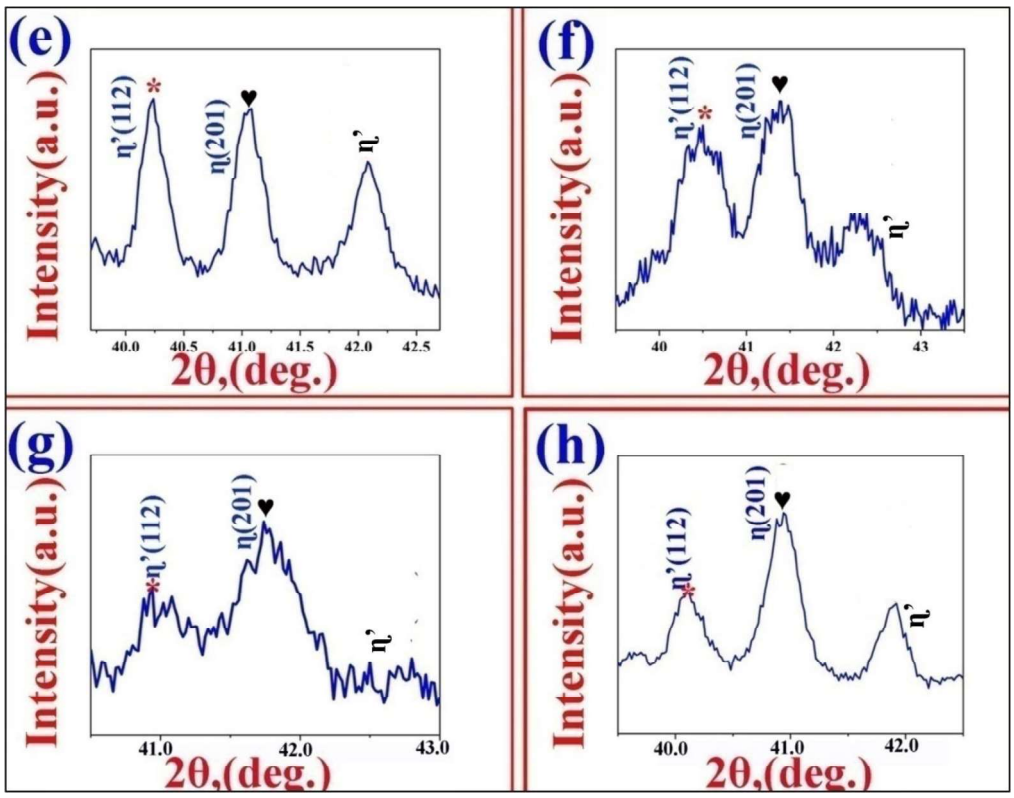

Figs. 3.12a-h. Continued……

Figs. 3.13a, c, e, g shows bright-field TEM images, and Figs. 13.3 b, d, f, h depicts respective selected area electron diffraction patterns. In Fig. 3.12 precipitates are shown in bright-field images, and corresponding spots are also shown in respective selected area electron diffraction patterns (SAEDPs). Spots from η' by white color, and η by yellow color. Fig. 3.12a depicts the precipitation behavior of as-received (un-strained) aluminum alloy, AA7075T7352. The presence of precipitates with rod, and plate-like morphologies, which are randomly distributed throughout the α-Al matrix was noticed. Corresponding SAEDPs ~ were given in Fig. 3.12b. Diffraction patterns (DPs) with sharp spots depict the α-Al matrix. On the other hand, DPs~ having weak spots encircled in white, and yellow prevail to the η', and η precipitates respectively. The high-intensity spot as encircled in red pertains to the 220 of α-Al. All the transition precipitates (η' and η) are giving diffraction spots (Fig.

3.12 b) in SAEDP of as-received alloy. Fig. 3.12c shows a bright-field TEM micrograph of the 0.02 tensile strained specimen D_2. The presence of dense dislocation, and a very smaller number of precipitates with rod, and plate-like morphologies were seen. SAEDPs~ analogous to these are given in Fig. 3.12d. Existences of sharp, and weak spots were also seen in this. However, their intensities were much less in comparison to the as-received condition. The spot locations (220 of α-Al) as denoted by 1, 2, and 3 and η' as encircled in white do not give the diffraction spot. Only η and some of the 220 spots of the α-Al, denoted by 4, 5, and 6 give the diffraction spots (Fig. 3.12d) in SAEDP of D_2. One notices that the average length and width of the rod-like precipitates are 380±19 nm, and 180±13 nm respectively. On the other hand, the length and width of the plate-type precipitates are170± 14nm, and 30±3nm alternatively. At 0.02 tensile straining, the average length, and width of the rod-type precipitates are 150±6nm, and 60±4nm respectively. On the other hand, the length, and width of the precipitates with plate morphologies were 170±14 nm and 30±3 nm respectively. Further, at 0.06 tensile straining, in Fig.3.12e, the absence of the spherical and rod-type precipitates is seen. However, dislocation entrapment at the interface of α-Al and η precipitates was also seen. Therefore, measurement of the size is quite difficult in this state. Due to the fully shear-resistant nature of the η phase, the size remains the same (length 167±8 nm, width =31±2nm). On the other hand, the phases having rod morphology may be partially dissolved. Furthermore, at 0.1 tensile true straining, in Fig. 3.12g, the size of very small dynamically formed spherical precipitates is 30±2nm. Whereas, the length and width of rod-type precipitates are 186±9 nm, and 90±7 nm respectively. Moreover, the length and width of plate-type precipitates are 168±10nm, and 30±2nm respectively.

Further, Fig. 3.12e displays a bright-field TEM micrograph of the 0.06 tensile strained specimen D_3. The presence of the rod and plate-like precipitates surrounded by the

dislocations was noticed in this. SAEDPs~ related to this are given in Fig. 3.12f. Occupancy of the high-intensity super-lattice diffraction spots was noted in this. Only α-Al and η give the diffraction spots (Fig. 3.12f) in SAEDP of D_3. Similarly, Fig. 3.12g illustrates a bright-field TEM micrograph of the 0.1tensile strained specimen D_4. Agglomeration of small precipitates along with a plate and rod-like morphologies were seen in this. The amount of rod type of precipitates is high as compared to the other plate-like precipitates as shown in the elliptical and rectangular boxes. SAEDPs~ corresponding to these are given in Fig. 3.12h. The 220 spots of α-Al, as encircled in red, gives the high-intensity diffraction spot, η' and η are giving low-intensity spots (Fig. 3.12h) in SAEDP of D_4. The presence of sharp and randomly distributed weak spots were notable features in this. Sharp spots, as encircled in the white, are related to the α-Al matrix.

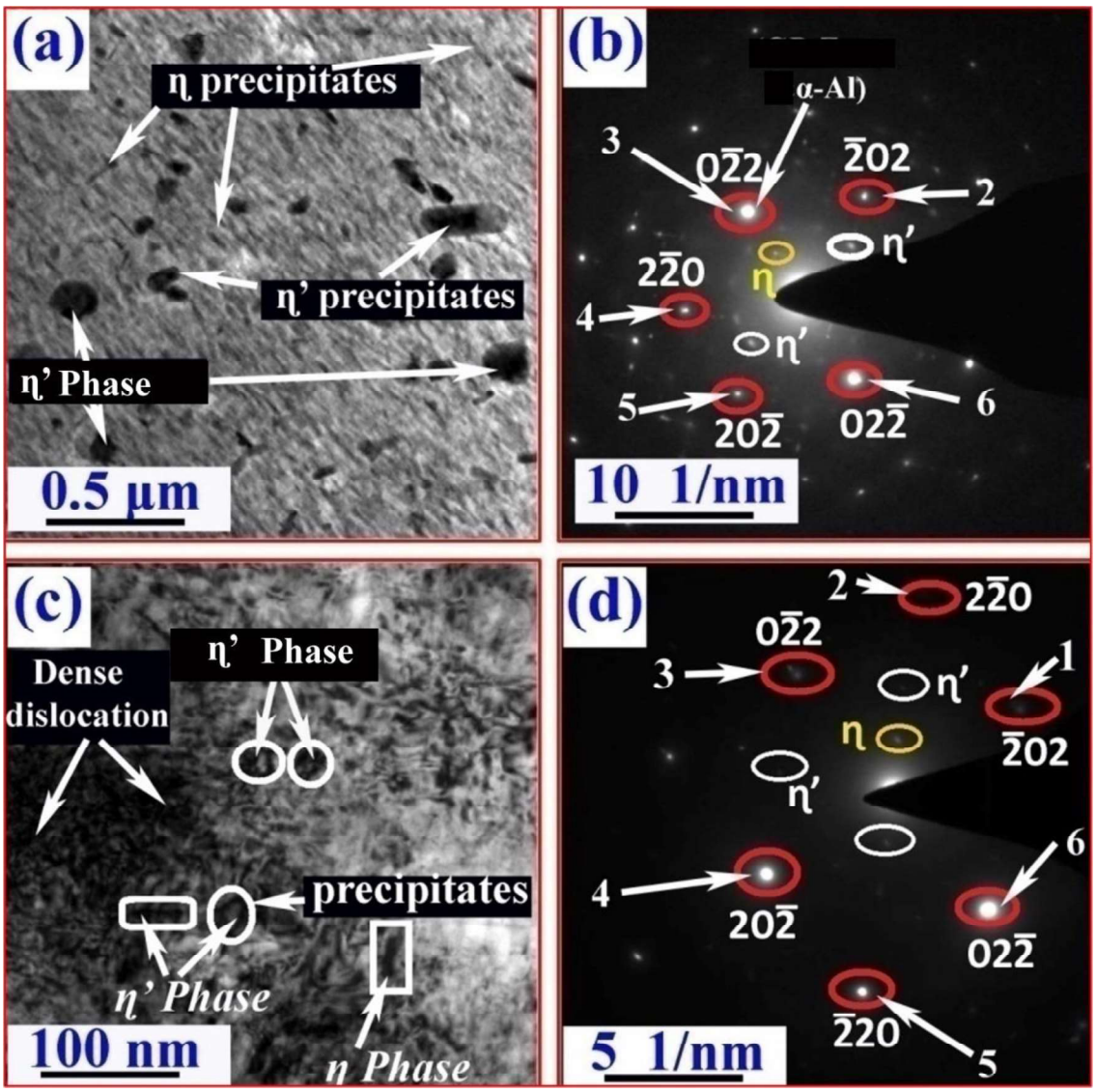

Figs. 3.13a-h. Precipitation behavior: (a,c,e,g,) bright-field TEM micrograph of the as-received as well as tensile strained specimens D1, D2, and D3 respectively, (b,d,f,h) their corresponding selected area electron diffraction patterns.

However weak spots are of the precipitate particles or solute atoms. Further, analyses of diffraction spot patterns show the presence of α-Al matrix along with second phase particles of the$MgZn_2$(η' and η). One noticed that ηare showing 3rd-order lattice-multiplicity (3*1.43Å of α-Al_{220}= 4.29Å of the η) concerning 220 diffraction spot of α-Al (PDF#77-1177 and # 85-1327 respectively) as shown in the Figs. 3.12 b, d, h.

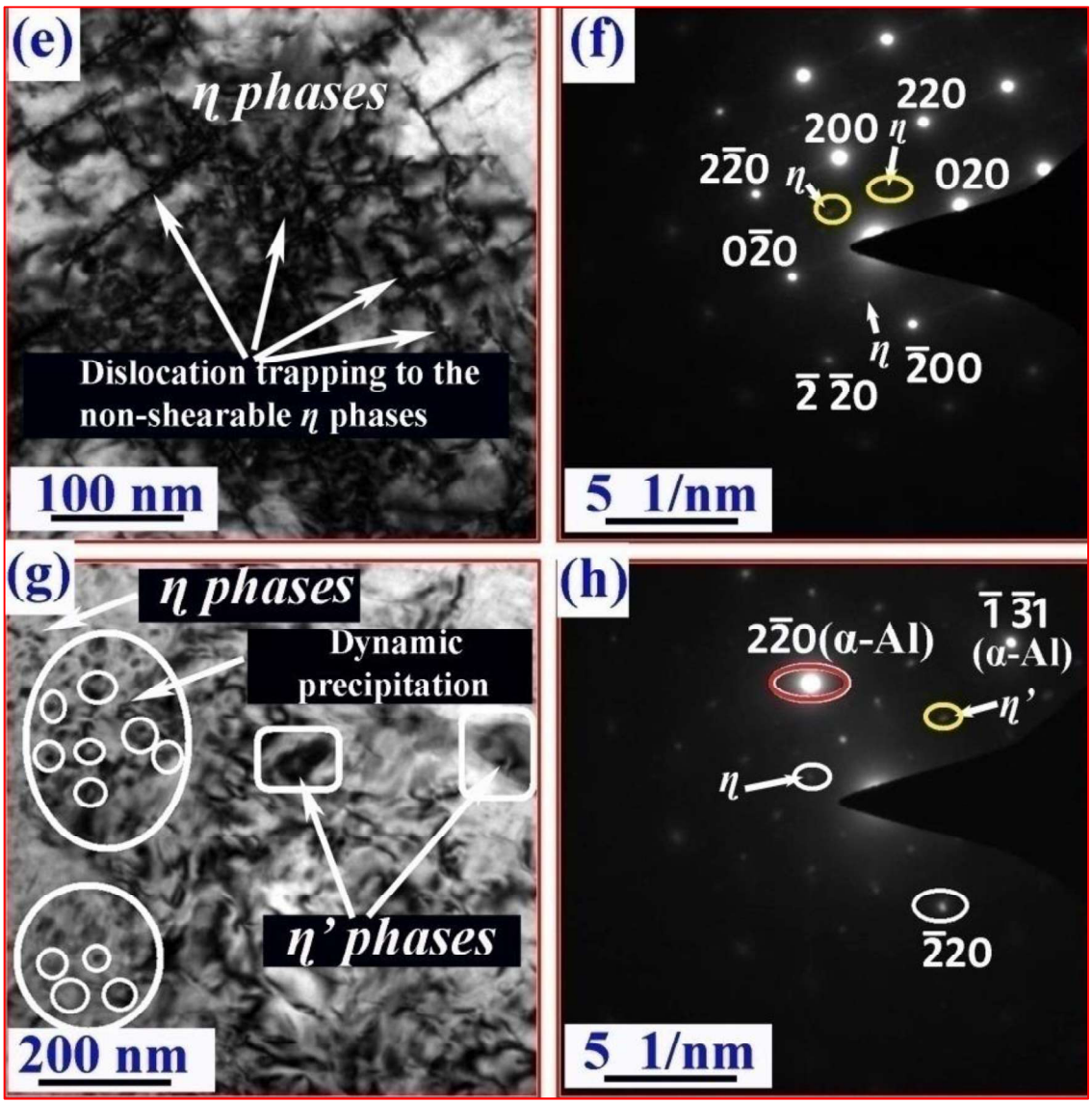

Figs. 3.13 a-h Continued……

The size of the precipitates was measured using the Image-J software and their values are given in Table 3.2.

Table 3.2 Size of precipitates of the as-received, D_2, D_3, and D_4 specimens.

Type of Precipitates/samples	**As-received, D_1**	**D_2**	**D_3**	**D_4**
True strain		**0.02**	**0.06**	**0.1**
Size		nm	nm	nm
η' Precipitates (Rod) Length, L= Width,W=	 380±19 180±13	 150±6 60±4	 -	 Re-precipitated 186±9 90±7
η Precipitates (Plate) Length, L= Width,W=	 170±14 30±3	 165±7 28±2	 167±8 31±2	 168±10 30±2

Tensile straining of the specimen $D_1$was applied till fracture. The material failed at 17% ±0.5 total elongation (EL). other mechanical properties e.g., YS, UTS, and UTS/ YS ratio were calculated (Table 3.3). True strain corresponding to necking is found to be 0.16.

Table 3.3 Tensile properties of the fractured specimen D_1 of AA7075T7352

Specimen	**YS (MPa)**	**UTS (MPa)**	**% EL**	**UTS/YS**
Failed specimen *(D_1)*	385±7	438±2	14±0.5	1.14

Dislocation behaviors of alloy could also be seen, respective to the tensile true strain of 0.02, 0.06, and 0.1, below the maximum percentage elongation, in Figs. 3.14-16. Fig. 3.14a displays the diffraction spot pattern of the tensile strained specimen D_2. Linearly ordered sharp and weak spots in the suitable 3-beam conditions are noteworthy features. The sharp, and weak spots are of the diffracted g-vector of the α-Al. The intensity of the g spot is high as compared to the 2g and 3g diffracted spots. The high-intensity spot depicts the strong beam. On the other hand, less intense spots illustrate the weak beams.

Figs. 3.14b-c displays bright-field (BF) TEM micrographs from the same region. Dislocation loops along with the low-density tangled dislocations were seen in the former. Whereas, forest dislocations along with the high-density dislocation tangles were noticed in the latter. Figs. 3.14d-e represents the weak-beam dark-field TEM (WBDF-TEM) micrographs. The presence of dislocation loops and the tangled dislocations were seen respectively. The former is related to the weak diffraction spot 2g, DF-1. On the other hand, the latter is of the weak diffraction spot 3g, DF-2 (as encircled in yellow).

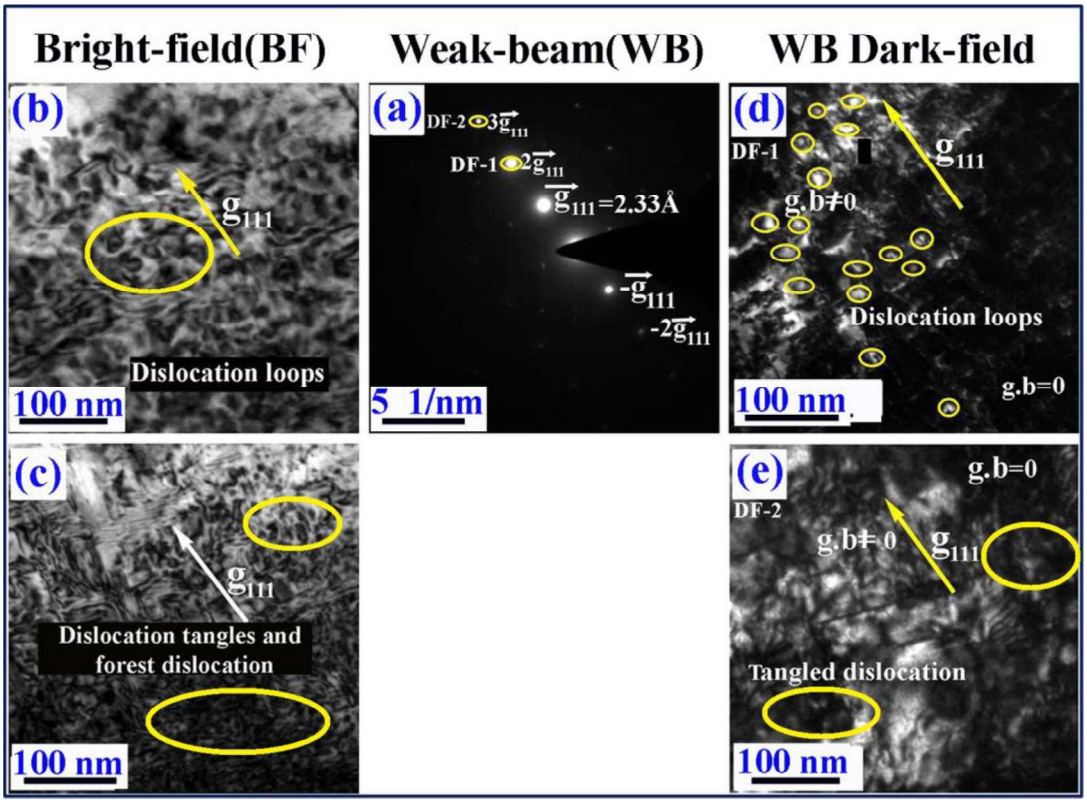

Figs. 3.14 a-e. Dislocation behavior of D1 (true strain~ 0.02): **(**a) diffracted, 111 g – vector, when after tilting, (b,c) bright-field TEM micrographs from the same region, b showing dislocation loops, c showing forest dislocation and high-density dislocation tangles, (d,e) weak beam dark field (WBDF) TEM Micrograph from 2g, DF-1 and 3g, DF-2(encircled in yellow) respectively, dislocation loops and tangled dislocations are observed respectively.

Fig. 3.15a illustrates the diffraction spot pattern of the tensile strained specimen D_3. The ordered sharp, and weak spots in a 3-beam condition were also notable in this. The diffracted spots are related to the g-vector of α-Al. The intensity of the g spot is higher as compared to the 2g and 3g diffracted spots in this state. Hence, the former (g spot) depicts the strong beam. However, later spots (2g and 3g) are weak diffracted spots. Figs. 3.15b-c represents the bright-field (BF) TEM micrographs from the region. Low- and high-density Taylor lattice structures were seen respectively. The presence of dislocation structure was also notable in the checker-board type patterns of the Taylor-lattice structures. Figs. 3.15d-e reveals the weak-beam dark-field (WB-DF) TEM micrographs. Low-, and high-density Taylor lattice structures were also clearly seen respectively. The former is related to the WBDFTEM micrograph from the spot 2g, DF-3. On the other hand, the latter reveals the WBDF-TEM micrograph from the weak spot 3g, DF-4 (as encircled in yellow).

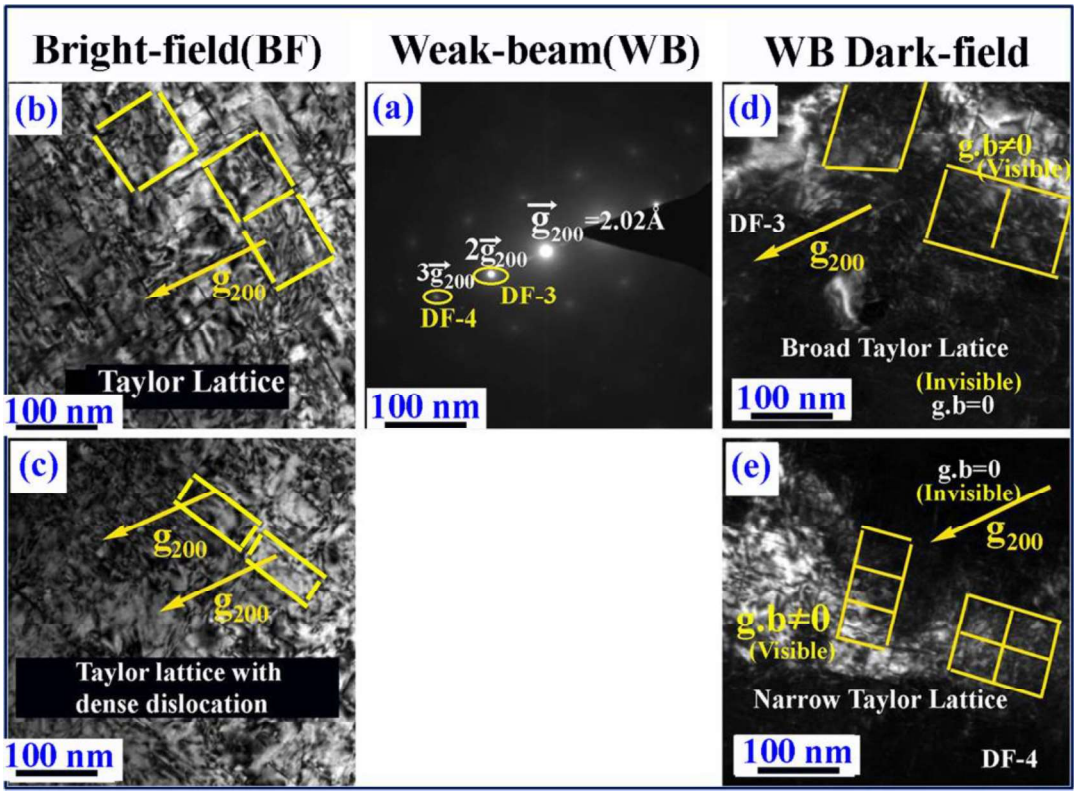

Figs. 3.15 a-e. Dislocation behavior of D2 (true strain 0.06): **(**a) diffracted, 200 g – vector after suitable tilting for weak beam condition. (b,c) bright-field TEM micrographs from the same region, showing Taylor Lattice structures with low and high dislocation density respectively, (d,e) WBDF TEM micrographs from 2g, DF-3, and 3g, DF-4 (encircled in yellow) showing broad and narrow Taylor lattices respectively.

Fig. 3.16a displays the diffraction spot pattern of the tensile strained specimen D_4. Sequentially arranged sharp and feeble spots were note-worthy features. The diffracted spots are related to the g-vector of α-Al. The intensity of the g spot is high as compared to the 2g diffraction spot. On the other hand, the intensity of the –g and -2g spots is less. Therefore, less intense spots depict the weak beam whereas high-intensity spot shows the strong beam. Figs. 3.16b-c presents bright-field (BF) TEM micrographs from the same region. Low-, and high-density dislocation cell structures are note-worthy micrographic features respectively. The cell size also becomes sharp in the latter as compared to the former micrograph. Figs. 3.16d-e shows the weak-beam dark-field TEM micrograph. Low-, and high-density

dislocation cell structures were also observed. The former is related to –g, DF-5 weak spot. On the other hand, the latter is of the -2g, DF-6 (encircled in yellow) weak diffraction spot. Invisibilities of the dislocations were also seen in some of the regions. Finally, three stages of dislocation rearrangements were noticed in Figs. 14-16. They are dislocation loops to the tangled dislocation in the 1st stage, at 0.02 tensile true straining. The tangled dislocation to the Taylor lattice/slip-band type structures into the 2nd stage, at 0.06 tensile true straining. Whereas, Taylor-lattices to dislocation cell structures in the 3rd stage, at 0.1 tensile true straining.

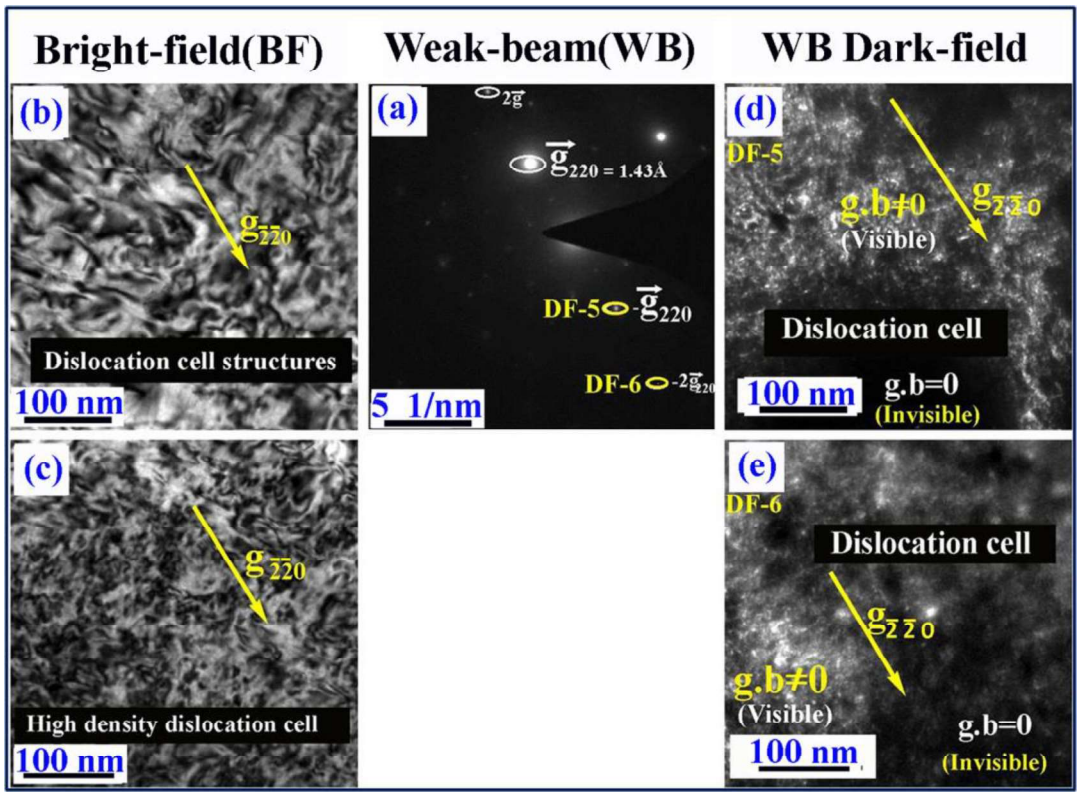

Figs. 3.16a-e. Dislocation behavior of D3 (true strain ~0.1): **(**a) diffracted, 220 g – vector after suitable tilting. (b,c) bright-field TEM micrographs from the same region, b showing low-density dislocation cell structure, c showing high-density dislocation cell structures (d,e) Weak beam dark field TEM Micrograph from the –g, DF-5 and -2g, DF-6(encircled in yellow) diffracted beam, Low and high-density dislocation cell structures were seen respectively (color figure online).

Fig. 3.17 shows the projected Burger vector of dislocation corresponding to the diffracted g-vector of α-Al, considering that the Burger vector is [110] type of α-Al because dislocation moves along the close-packed direction of the α-Al. The d-spacing value of the 1st spot of the diffracted g-vector at 0.02, 0.06, and 0.1 tensile true straining, in Figs. 14a,15a, and 16a are 2.33Å, 2.02Å, and 1.43Å respectively. The subsequent spots following ordered multiplicity respective to the 1st spot. All these are identified as 111, 200, and 220 diffracted g-vectors respectively of the α-Al (PDF#85-1327). The Burger vectors were characterized using the invisibility criteria (g.b=0). One notices that projected Burger vectors respective to 111 diffracted g-vector are ~$a_0/2[\bar{1}10]$, $a_0/2[1\bar{1}0]$ $a_0/2[\bar{1}01]$, $a_0/2[10\bar{1}]$. Whereas, $a_0/2[\bar{1}10]$, $a_0/2[1\bar{1}0]$, $a_0/2[0\ \bar{1}\ \bar{1}]$ are Burger vectors corresponding to 200 diffracted g-vectors. On the other hand, $a_0/2[\bar{1}10]$, and $a_0/2[1\bar{1}0]$ are Burger vectors of the 220 diffracted g-vector of the α-Al.

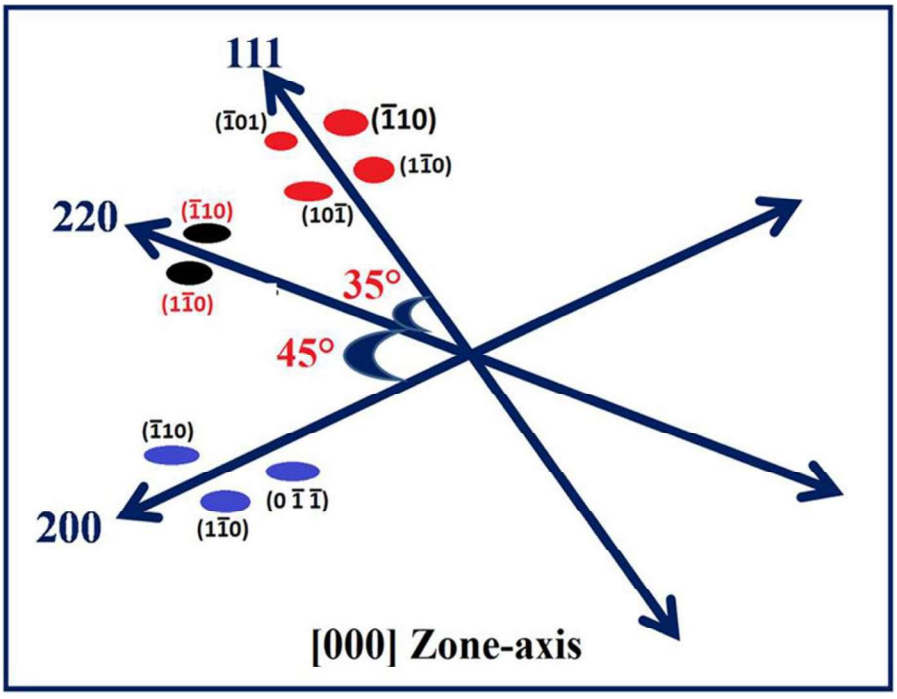

Fig. 3.17. Schematic of diffracted g-vector and Burger vectors of the dislocation loops projected along the [000] zone-axis.

The mechanical properties of fractured specimen D_1, are shown in Table 3. One observed that the yield strength (YS) and ultimate tensile strength (UTS) of the D_1 are 385±7 MPa, and 438±2 MPa respectively. In addition to this, a high ratio of ultimate tensile strength to yield strength (UTS/YS~1.±0.2) is also noticed in this. Figs. 3.18a-b displays the engineering stress vs. engineering strain curve of the fractured specimen D_1. The consistent increase of engineering stress after the elastic limit is the notable feature up to UTS. Fig. 3.18c depicts a log-log plot of the true stress versus the true strain curve. The sharp changes in slope characteristics are observed in the high-strain regimes. Fig. 3.18b shows the fitted flow curve of the log-log plot of true stress vs. true plastic strain data of the failed tensile specimen D_1. One notices the best fitting with the Ludwigson-relationship [$\boldsymbol{\sigma} = K_1\varepsilon^{n1}+\exp(k_2+n_2\varepsilon)$] of the failed specimen D_1. The mathematical terms k_1 and n_1 are the strength co-efficient, and hardening exponent in the high strain regimes. Whereas, k_2 and n_2 are the respective terms that indicate the low-strain regimes. The fitting parameters of the best-fitted curve are derived using the Ludwigson relationship. One noticed a sharp change in the hardening exponent from low strain regimes, n_2 (- 48.93) to the high strain regimes, n_1(0.87). The fixed strain value, at which slope changes from low strain regime to high strain regime, is known as the transition true-strain, which is denoted by the ε_L, and their value is near ~ 0.05. The very high variation, of strength co-efficient is also observed from k_2(4.61) to k_1 (3392). The Adj(R^2) value of the best-fitted flow curve is very close to 1(0.99687), which shows one of the best fittings with the flow curves. Fig. 3.18e displays the hardening rate ($d\sigma/d\varepsilon_p$) versus the true plastic strain (ε_p) curve. The three stages of the hardening characteristics are observed in this. These are sharp decline in the 1st-stage, dip, and hump nature in the 2nd-stage, and linear decrease in the 3rd-stage.

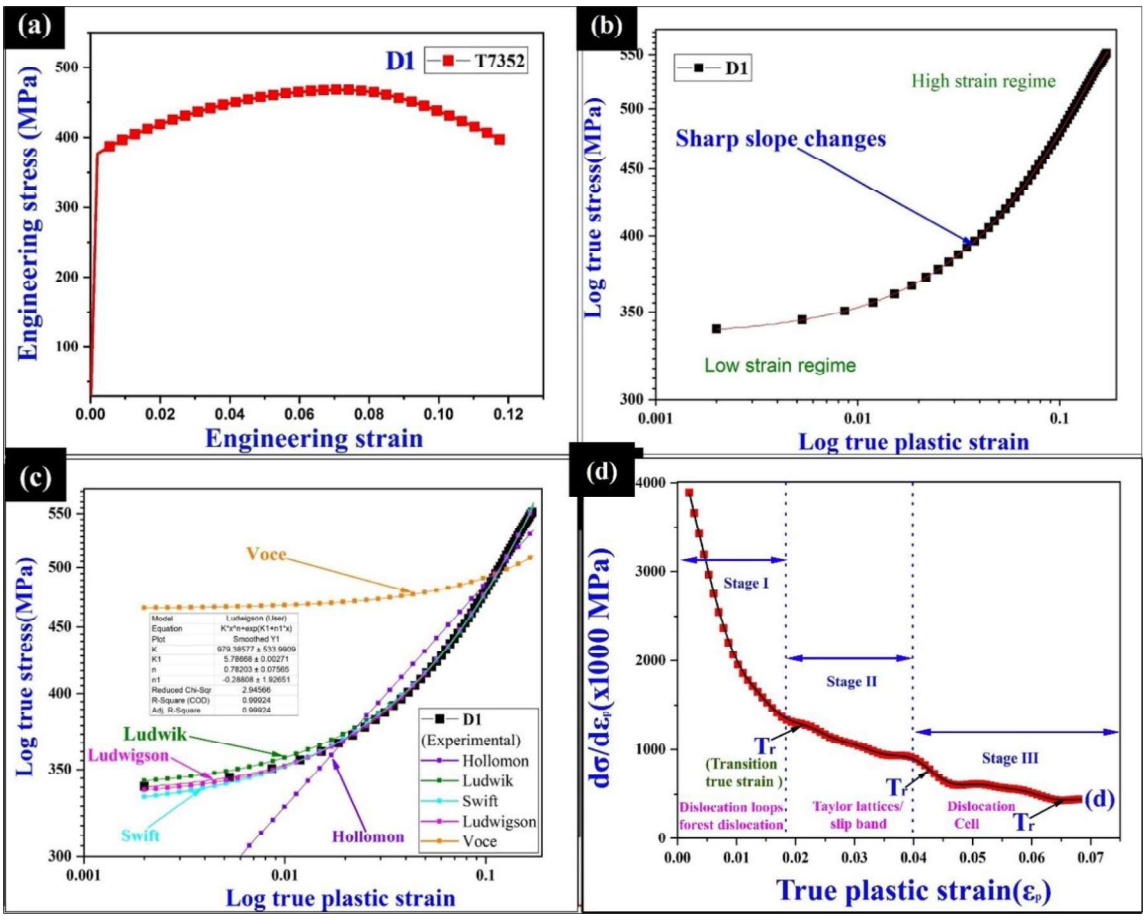

Figs. 3.18a-e. Tensile properties of the elongated specimen ***D1***till the fracture: (a) engineering stress-engineering strain plot, (b) true stress-true strain, (c) logarithmic plot of the true stress-true strain (d) Ludwigson curve fitting of the logarithmic plot (true stress-true plastic strain), (e) hardening rate- true plastic strain curve behavior.

Fig. 3.19 shows a linear fitting curve in the last stage (3rd stage) of hardening curves. One of the best fittings of the Kocks-Mecking and Esterin (KME) based dislocation model *[n = θ_0+mσ]* was seen. The mathematical term, θ_0 is a constant that describes dislocation storage capacity. Whereas, the remaining terms, σ, and m pertain to true stress, and slope of the linear portion respectively. Fitting curve parameters are derived using the KME-based dislocation models. High dislocation storage capacity (θ_0= 4921), and large negative slope value (m = -26735) were obtained. Ajd (R^2) value of the fitted curve is very close to 1(~0.9978).

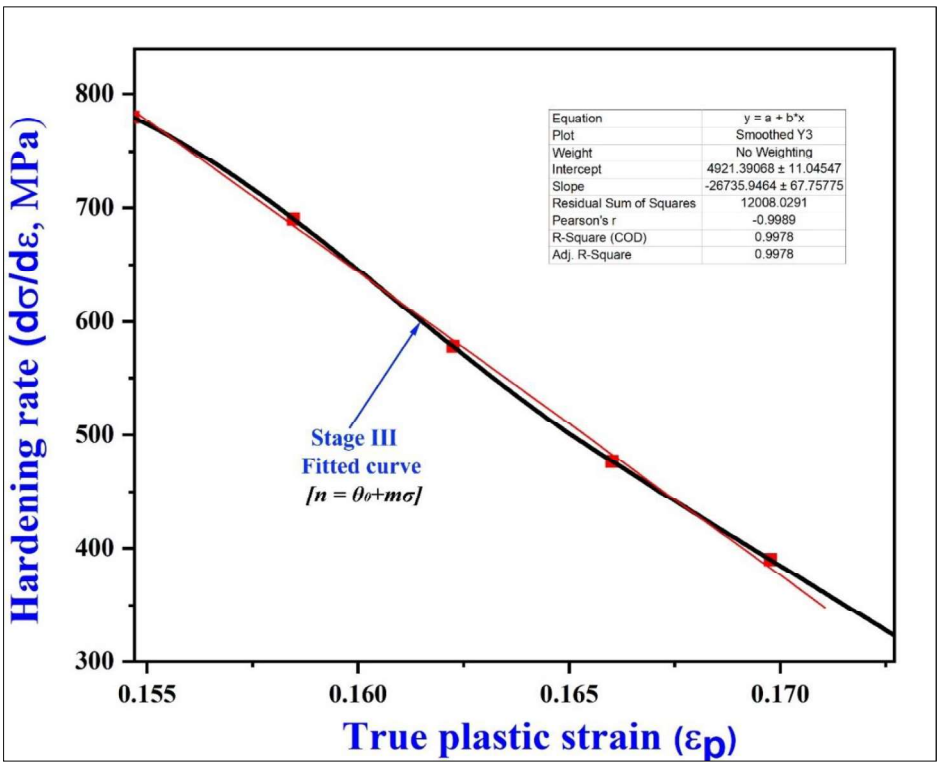

Fig. 3.19. Hardening rate (θ) vs. true plastic strain (ε_p) in the 3rd- stage shows a linear relationship with slight fluctuations

Figs. 3.20a-c display fracture morphologies of fractured tensile specimen D_1. One noticed the facet/cleavage morphology in Fig. 3.20a. Whereas, dimples and microvoids as well as particle cracks were observed in Fig. 3.20b. The dimple ruptures were seen in Fig. 3.20c.

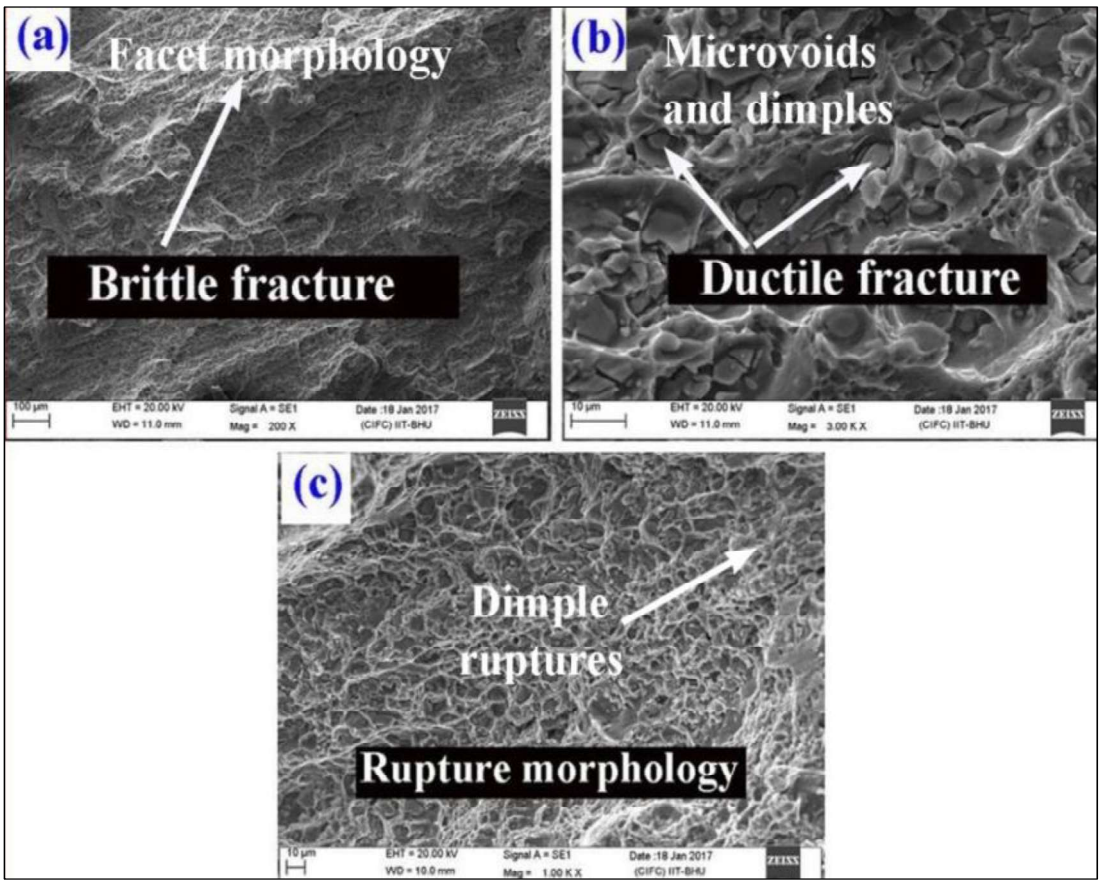

Figs. 3.20a-c. Fracture morphologies of the tensile specimen D_1. One sees the facet/cleavage morphology in Fig. 3.20a. Whereas, dimples and microvoids, as well as particle cracks, were noted in Fig. 3.20b. On the other hand, dimple ruptures were seen in Fig. 3.20c.

3.2.3 Part III Microstructure evolution, Texture characteristics, Flow behaviors and Mechanical properties of the aged 7075 Al-Alloy

3.2.3.1 XRD analysis

Fig. 3.21a displays the XRD pattern of the under-aged (T4) 7075 Al-alloys. The presence of the sharp crystalline peaks, 111, 200, 220, and 311 of α-Al (Lattice parameter, a = 4.08 Å), is only seen respective to d-spacing values of ~2.33 Å, 2.02 Å, 1.43 Å, and 1.21 Å (PDF#77-1177&652504). This belongs to the space group of $Fm\bar{3}m$ (225) and is attributed to the Pearson symbol of cF_4. Fig. 3.21b portrays the XRD pattern of the peak-aged (T6) 7075 Al-alloy. The presence of the sharp crystalline peaks, 111, 200, 220, and 311 of α-Al (Lattice

parameter, a= 4.08Å), are also observed, along with the less intense crystalline peaks, 002, 112, and 201 of the GP zones (4.29 Å), η'(2.34 Å), and η (2.31 Å, $MgZn_2$, Laves phases of C14 type). The η phase belongs to the space group of $P6_3/mmc$ (194) and is related to the Pearson symbol of AB_2 type. Added to this, a minor 002 crystalline peak of the Al_2Cu phase (*Pearson symbol:* tI_{12}) is also observed at d~ 2.98 Å (2θ~30^o). This phase belongs to the space group of I4/mcm (140), having lattice parameters, a = 6.06 Å, and c = 4.87 Å, respectively. Fig. 3.21c shows the XRD pattern of over-aged (7075-T73) alloy. The sharp crystalline peaks of α-Al, and less intense crystalline peaks of η' and η areobserved. However, one of the less intense crystalline peaks of the η zone (4.29Å) is found absent in this. Fig. 3.21d shows the XRD pattern, of T7352 tempered alloy. The sharp crystalline peaks of α-Al, and minor crystalline peaks of η' (2.34 Å), η (2.31 Å), and Al_2Cu (2.98Å) are observed in this. The phases of the ηare noticed, respective to the slightly shifted new 2θ peak position (d~4.24 Å). In addition to this, the relative intensity of the 2θ peak position of ~38.9° (d~2.31Å) is less than the T6 temper but higher than the T73 temper. Lattice parameters of the GP zone, η', and η are measured by 4.28 Å, 4.90 Å, and 5.46 Å respectively.

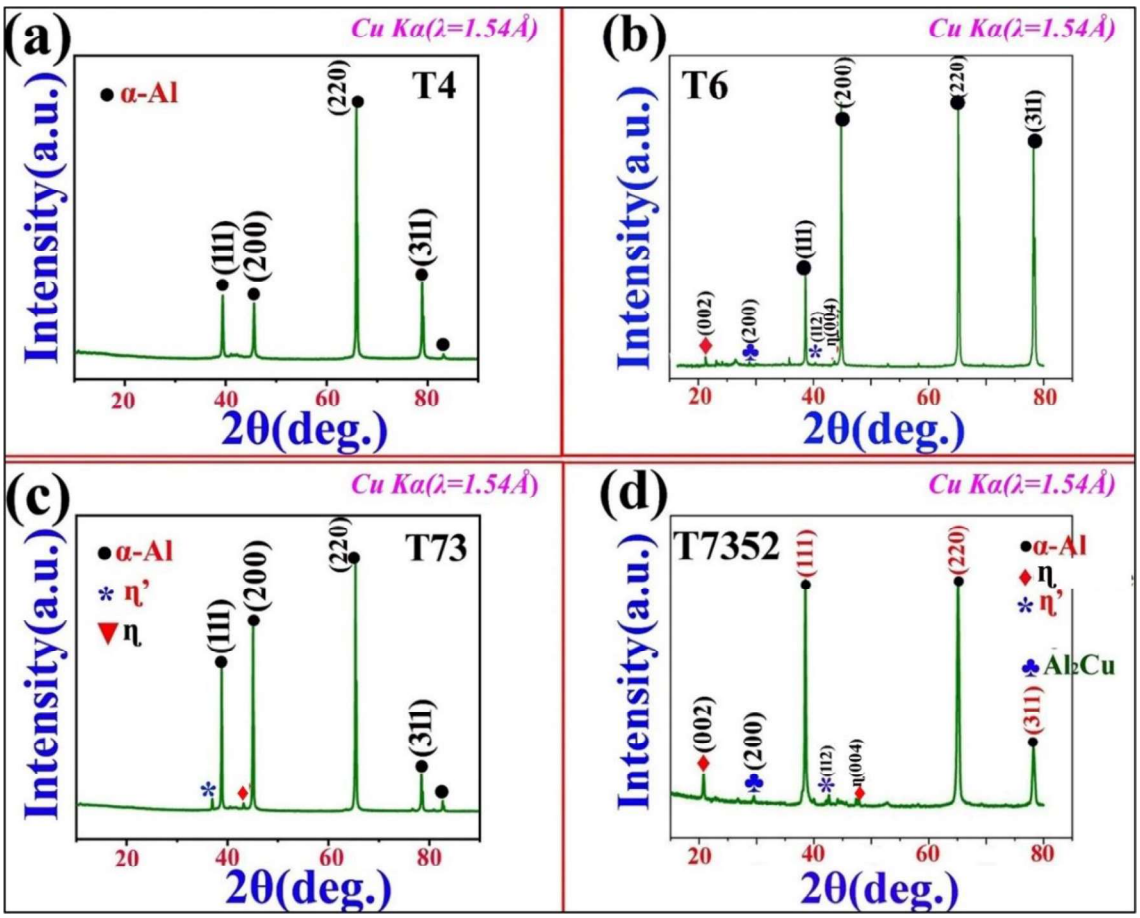

Figs. 3.21a-d XRD pattern of heat-treated 7075 Al-alloy: (a) under-aged(T4) state, (b) peak-aged (T6) condition, (c) over-aged (T73) state, and (d) T7352 temper.

Lattice micro-strain (ε), crystallite size (*D*, in Å), and dislocation density(ρ/m^2) measurement are done by the x-ray line profile analysis with the help of Leibenberg Marquardt's least square regression fitting method and it is found that the crystallite size (*D in Å*) of T4 and T6 samples are 13.5 Å, and 20.18 Å, respectively, whereas, it is measured to be 15.13 Å, and 7.8 Å, for T73 and T7352 tempers. Similarly, lattice-micro strain for T4 and T6 tempers are~ 0.1443 and 0.0704 respectively. It was measured to be 0.0618 and 0.090 in the case of T73 and T7352 tempers. Under-aged (T4) alloy shows high dislocation density, which is found to be ~13x10^{17}/m^2 (Table 2). After peak-ageing (T6 temper), dislocation density decreases significantly (~5.5x10^{17}/m^2). Over-ageing (T73 temper) further displays lower dislocation

density which is measured to be $4.5x10^{17}/m^2$. Such reduced dislocation density shows that dislocation becomes the driving force for nucleation of the metastable (η') and equilibrium (η) precipitates. Compressive deformation (10%) at T7352 temper, further increases dislocation density up to~14.2 $x10^{17}/m^2$. The current investigation does texture characterization with the help of typical f.c.c. deformation texture [114–116], as well as deformation + recrystallization textures reported in the literature [116 A, 116 B].

3.2.3.2 Microtexture

Figs. 3.22a-d display micro-texture characteristics, orientation distribution function (ODF), Φ_2=0º, 45º, 65º, and 90º sections of T4, T6, T73, and T7352 tempered alloy. The presence of the Goss {011} <100> recrystallization textures with the same intensities (x14.8 R) are noticed respective to the Φ_2=0º, and 90º sections at T4, T6, and T73 tempers (Figs. 3.22a-c). However, at T7352 temper, the evolution of the Goss {011} <100> recrystallization texture, with 21 times random (x21 R), is noticed corresponding to Φ_2 = 0º and 90º sections (Fig. 3.22d). Added to this, evolution of Rotated Cube {013} <100>, and S {123} <634> textures were also seen respective to the Φ_2 =45º, and 65º sections, with 21 times random (x21 R).

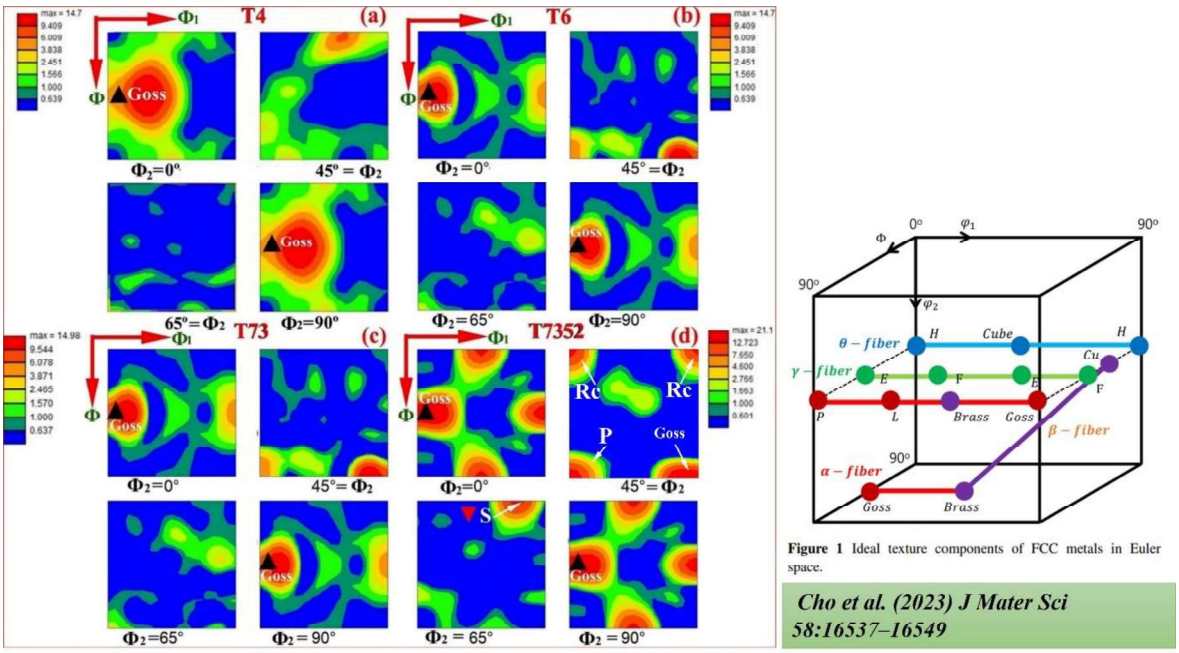

Figs. 3.22a-d Orientation distribution function (ODF) Φ_2 = 0º, 45º, 65º and 90º sections (Bunge notation) of the T4 (a), T6 (b), T73 (c), and T7352 temper (d).

Fig. 3.23a-d shows grain size vs. area fraction map of T4, T6, T73, and T7352 tempered alloys. The average grain size for T4, T6, and T73 tempers does not change, which is measured to be 46±5 μm (Fig. 3.23a-c). Grain size only changes for T7352 and is measured to be 28±3 μm (Fig.3.24d), which is smaller than T4, T6, and T73 tempers. Grain size alters for T7352 temper, but it remains the same in the case of T4, T6, and T73 tempers. Therefore, the color-coded grain map, and IPF map of T73 (among same grain), and T7352 (different grain) temper is only shown in Fig. 3.24e, and f. Former, displays color-coded grain map of T73 temper. Preferred orientation along RD and 110 crystal planes (Fig. 3.24e) are observed. Whereas, the latter depicts a color-coded grain map of T7352 temper. Preferred orientation in this case is also along RD, and 001 crystal plane (Fig. 3.24f).

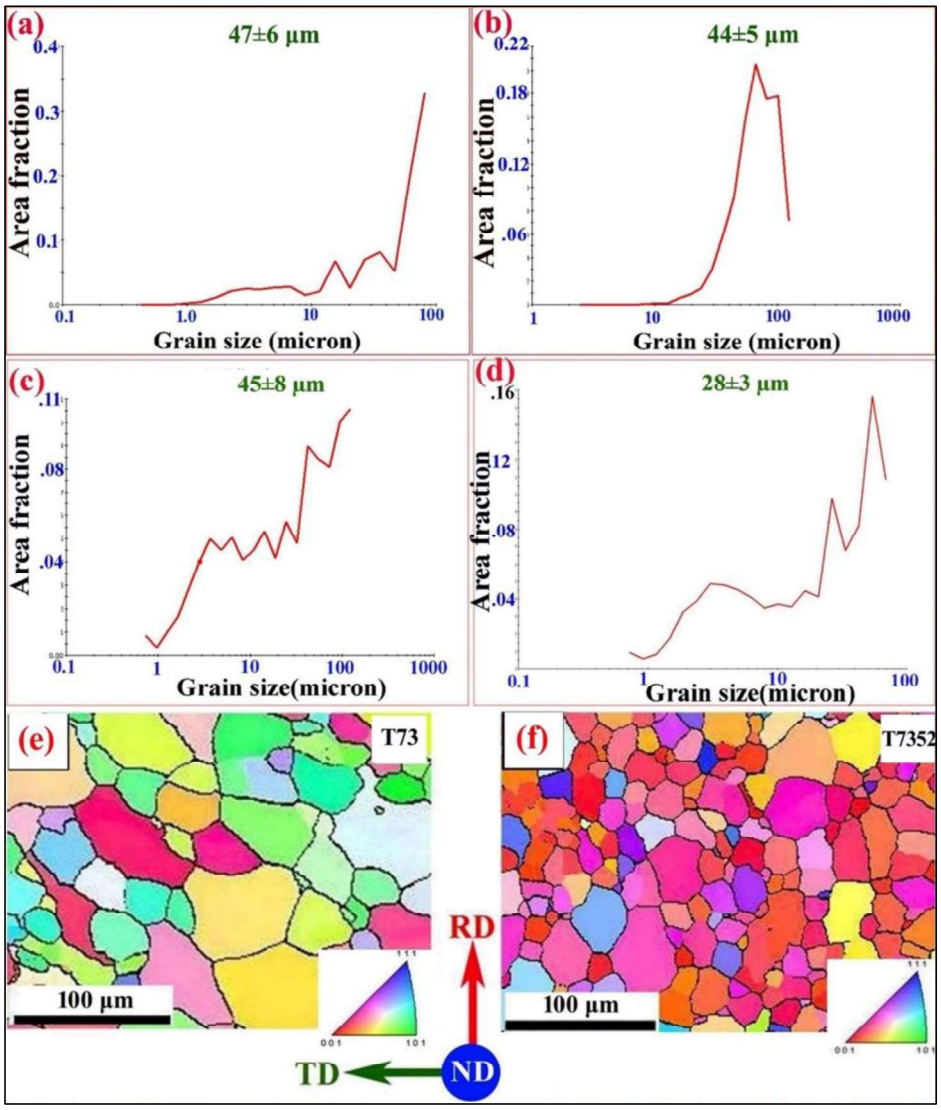

Figs. 3.23a-f Grain size variation: (a, b, c, d) T4, T6, T73 and T7352 tempers, (e, f) color-coded grain map/ inverse pole figure of T73 and T7352.

Fig. 3.24a shows a grain boundary map for T4 temper. High angle grain boundary fraction in this case is 66%, whereas low angle grain boundary fraction is 34%. Fig. 3.24b displays the grain boundary map for the peak-aged (T6) alloy. No significant changes, in grain boundary fractions are noticed in this. The low-angle grain boundary fraction is 35%, and the high-angle grain boundary fraction is 65%, which closely matches the T4 temper. Fig. 3.24c illustrates the grain boundary map of T73 tempered alloy. Significant changes in grain

boundary fractions can be seen. The low-angle grain boundary fraction is 66%, whereas the high-angle grain boundary fraction is 34%. Fig. 3.24d shows the grain boundary map of T7352 temper. The increased low-angle grain boundary fractions are 74%, whereas the high-angle grain boundary fraction is 26%.

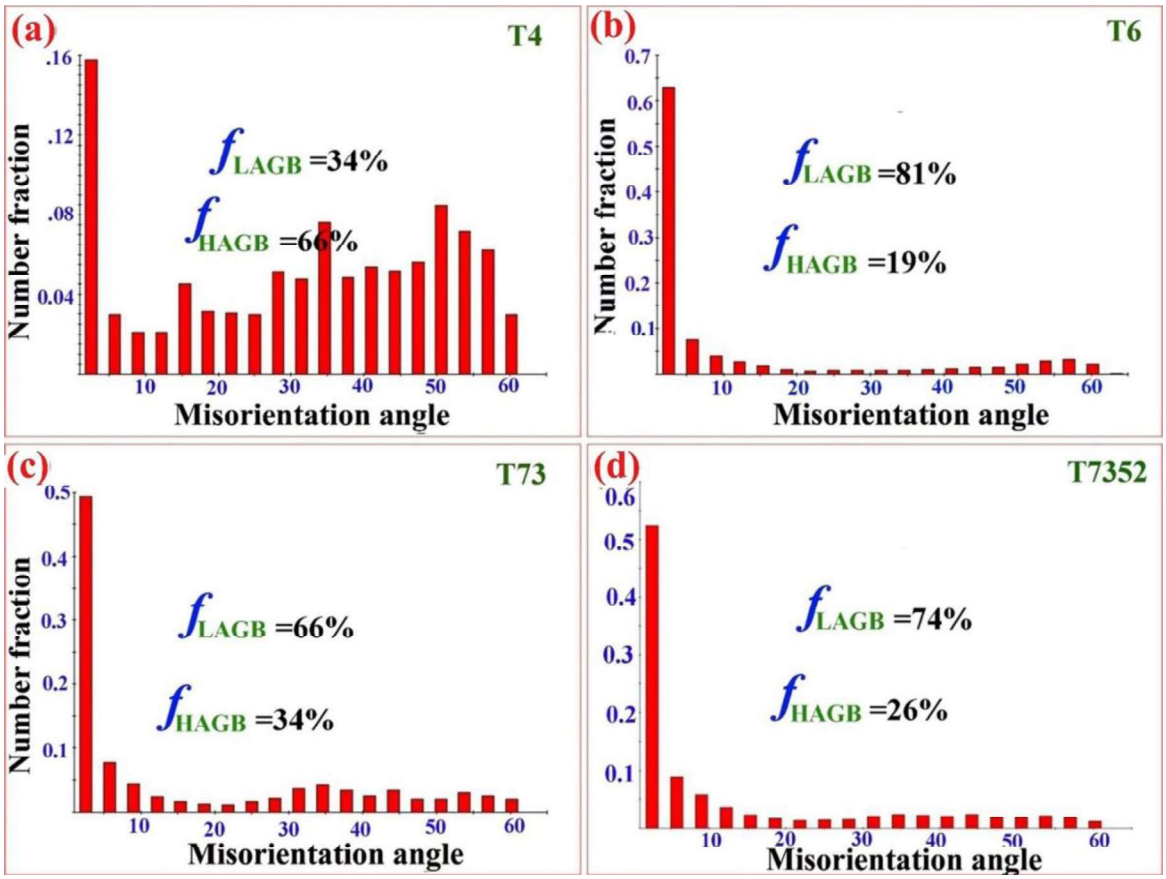

Figs. 3.24a-d. Misorientation angle of (a) under-aged (T4) alloy, (b) peak-aged (T6) alloy, (c) over-aged (T73) alloy, and (d) T7352 tempered alloy.

3.2.3.3 TEM Analysis

Fig. 3.25a depicts a bright field TEM micrograph of T4. This shows an absence of precipitate morphologies and indicates that room temperature aging is not enough for the decomposition of supersaturated solid solution. Corresponding selected area electron diffraction patterns (SAEDPs~) are given in Fig. 3.25b. Sharp crystalline diffraction spots of the α-Al, with 6-fold symmetry, and the absence of weak diffraction spots (DPs~) of precipitates are noticed in this. Fig. 3.25c shows the bright field TEM microstructure of the peak-aged (T6) alloy. This displays fine but randomly distributed rod-like (η'), and plate-type (η) precipitates. In addition to this, grain boundary precipitates (shown in the inset), and dark contrast of high atomic mass containing precipitates are observed. Corresponding SAEDPs~ are given in Fig. 3.25d. The presence of the sharp crystalline DPs~ of α-Al, and less intense DPs~ of precipitates with 6-fold symmetry are observed. Similarly, Fig. 3.25e shows a bright field TEM micrograph of T73-tempered alloy. Coarse but randomly distributed precipitates with rod (η') and plate (η) type morphologies are seen. Respective SAEDPs~ are given in Fig. 3.25f. This shows sharp crystalline DPs~ of α-Al, and weak crystalline DPs~ of the precipitates, which is denoted by the white arrow. Fig. 3.25g shows a bright field TEM micrograph of T7352-temper. The rod (η'), and plate (η) like precipitate morphologies are observed. However, their size differs from the other cases. Corresponding SAEDPs~ are given in Fig. 3.25h. This displays sharp crystalline superlattice DPs~ of α-Al and weak crystalline satellite-like DPs~ of precipitates with 4-fold symmetry.

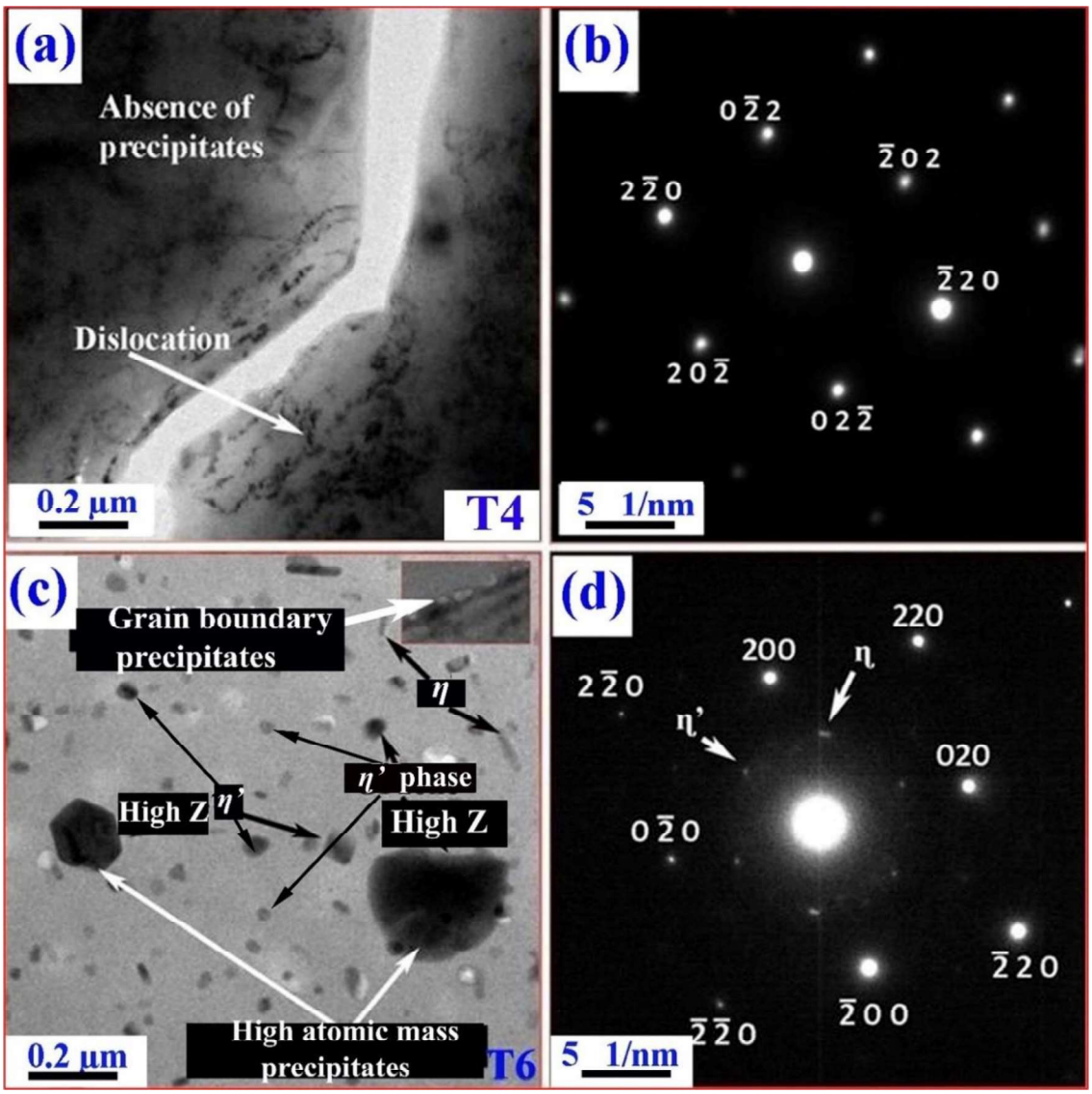

Figs. 3.25 a-h TEM microstructure: (a, c, e, g) bright-field TEM micrograph at T4, T6, T73, and T7352 tempers, (b, d, f, h) respective selected area electron diffraction patterns (SAEDPs~).

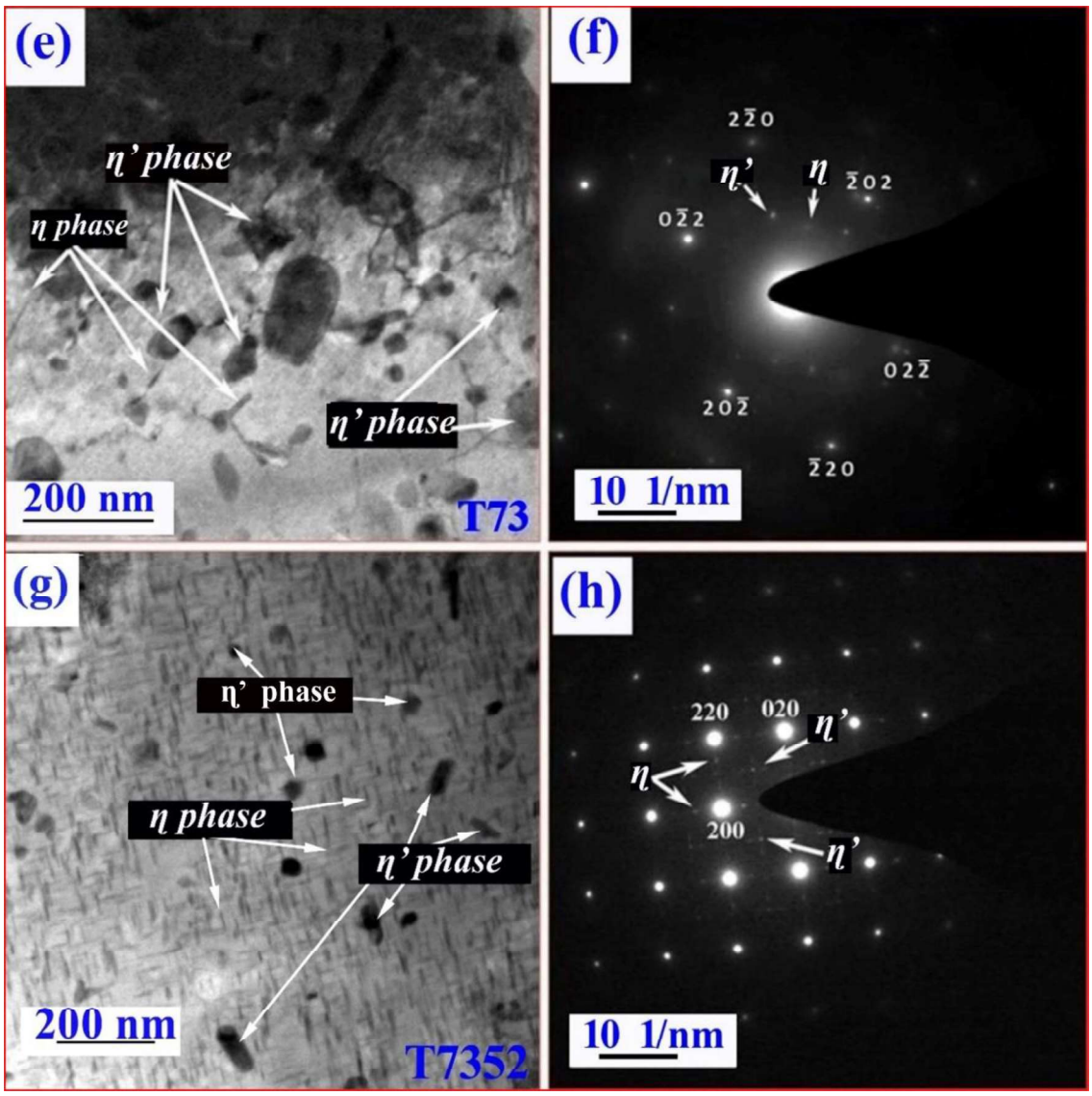

Figs. 3.25a-h. Continued……

The size of precipitates at various tempers are calculated using Image-J software, and their values are given in Table 3.4.

Table 3.4 Precipitates size in T4, T6, T73 and T7352 tempered Al-alloys

Aging state	η' (rod, nm)	η (plate, nm)
Under-aged, T4	Not formed	Not formed
Peak-aged, T6	Length = 20±3 Width = 8±1	Length=105±8 Width = 3±0.5
Over-aged, T73	Length = 85±5 Width =25±7	Length =120±6 Width=8±1
T7352 temper	Length = 72±4 Width = 18±3	Length =98±9 Width= 3±0.5

3.2.3.4 Nature of grain boundary precipitates

Fig. 3.25.1a displays the TEM micrograph, for T4 temper. No grain boundary precipitates and those of significant bulk precipitates were observed in the T4 state. Fig. 3.25.1b shows grain boundary precipitates (GBPts), of T6 temper. Major observations show continuously distributed η precipitates with an average length of 7.0±0.8 nm and an average width of 2.0 ±0.5 nm. Fig. 3.25.1c portrays GBPts of T73 temper. Discontinuously distributed η phase with an average length of 42±6 nm and an average width of 21±4 nm can be seen. Fig. 1d shows GBPts for T7352. The size of the grain boundary η increased, and the precipitate-free zones (PFZs) became narrow. The average length and width of the grain boundary η precipitates increased to 150±10 nm and 90±12 nm, respectively.

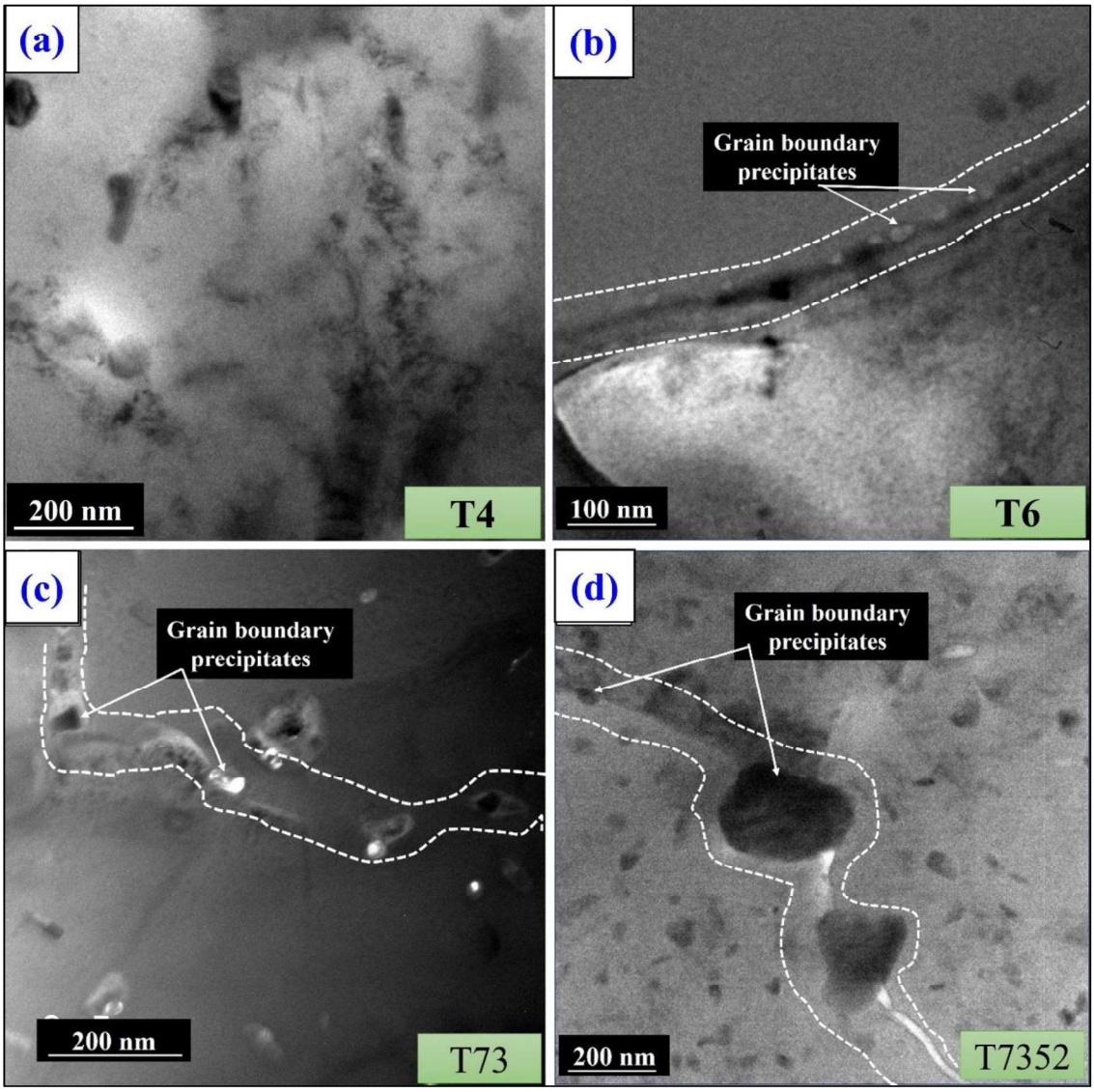

Figs. 3.25.1a-d Nature of grain boundary precipitates: (a) T4, (b) T6, (c) T73, and (d) T7352 tempers.

3.2.3.5 Nature of dislocation structures

Figs. 3.26a-b shows bright field TEM microstructure from another region of T7352 temper. Dislocation entrapment at the hetero-phase interfaces of the η, and α-Al, matrix is noticed in the former (Fig. 3.26a). In contrast, dense dislocation walls (DDWs~) are observed in the latter (Fig. 3.26b). Bright-field TEM imaging is not a reliable, and straightforward technique, to study the dislocation behavior of the alloy. Therefore, systematic dislocation

characterization is done with the help of weak-beam dark field (WBDF) TEM imaging. Fig. 3.26c displays diffracted spots (DPs~), after suitable tilting (α and β) to get the weak beam. The ordered sharp, and weak spots are found after suitable tilting. Diffracted spots show two-beam conditions of the α-Al. The intense spot indicates the strong beam, whereas weak spots show the weak beam. The d-spacing value of the first spot is around ~2.02Å, and the next spots follow the ordered multiplicity respective to their previous counterpart. Fig. 3.26d shows a weak beam dark field (WBDF) TEM micrograph taken from the 2g weak diffracted spot (Fig. 3.26c). This displays dense dislocation walls (DDWs~), and broad slip-band. The burger vector corresponding to the diffracted g-vector is calculated to be $a_0/2[011]$, using the in-visibility criteria (g.b = 0), considering that the Burger vector is [110] type of the α-Al. Dislocation becomes glissile (mobile), which follows the hu+kv+lw = 0 condition. At the same time, it becomes sessile (immobile) for the remaining slip systems. Here, {hkl} is the set of slip planes, whereas <uvw> shows the set of the direction.

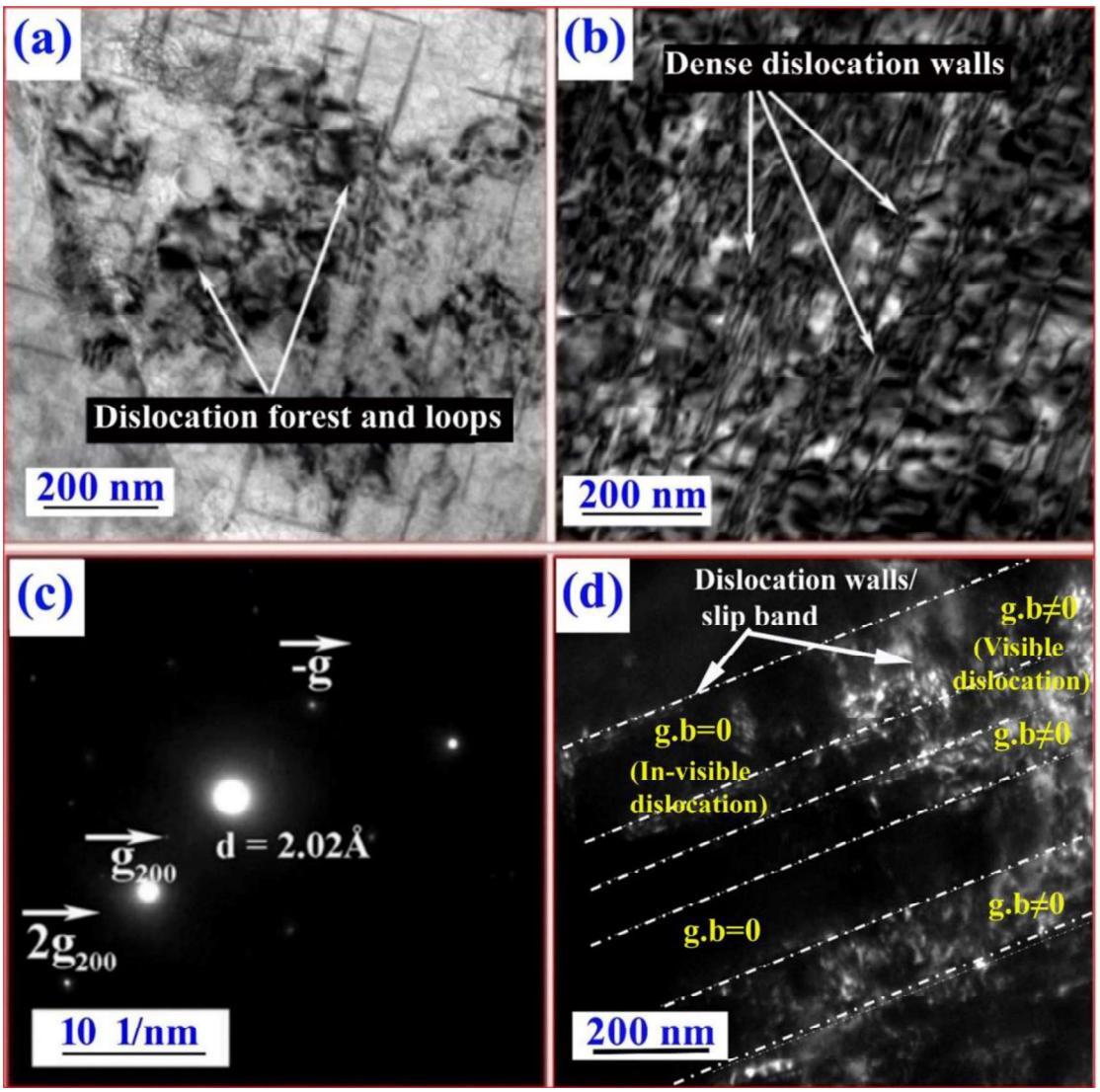

Figs. 3.26 a-d TEM microstructure: (a, b) bright-field TEM micrograph, (c) diffracted weak beam (2-beam), and, (d) weak beam dark-field (WBDF) TEM images from "2g" show dense dislocation walls (DDWs~) and slip-band.

3.2.3.5 Hardness and residual stress

Fig. 3.27 shows variation of hardness, and residual stress for T4, T6, T73, and T7352 tempered alloys. The average hardness for T4 and T6 are 176±2 Hv and 212±8 Hv respectively. One notices that the average hardness decreases as the over-aging start, and the hardness of T73, and T7352 tempers are 160±4 Hv, and 144±5 Hv alternatively. A higher drop in hardness, for T7352 temper, suggests formation of the soft phases. Residual stress

for all heat treatments is compressive by nature, which is measured to be -57±8 MPa, for T4 temper. The analyzed residual stress for T6 and T73 tempers are -42±10 MPa, and 78±5.7 MPa respectively. The residual stress for T7352 temper is measured to be -96±9 MPa.

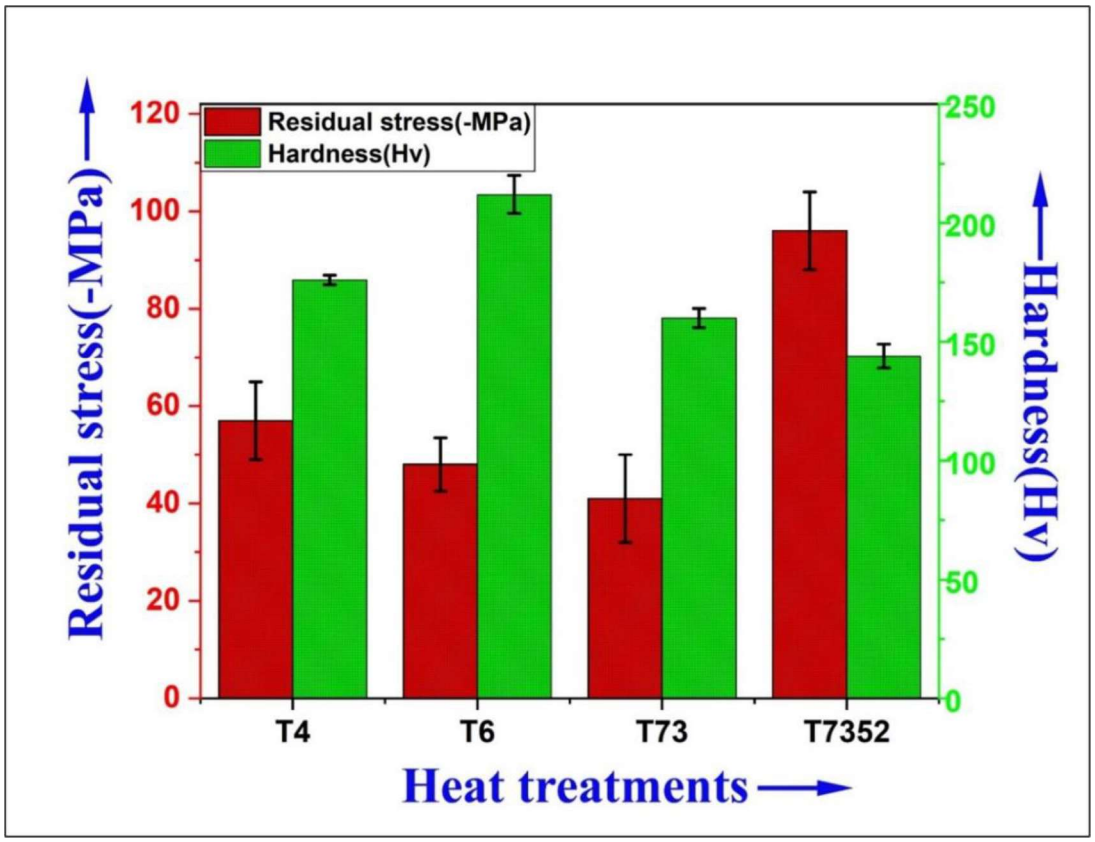

Fig. 3.27 Variation of hardness (Hv), and residual stress (MPa) of heat-treated 7075 Al alloy

3.2.3.6 Tensile properties

Fig. 3.28 shows engineering stress vs. engineering strain plots for T4, T6, T73, and T7352 tempers. Consistently increasing tensile stress (in MPa) after elastic limit and up to UTS is mainly observed for all the conditions.

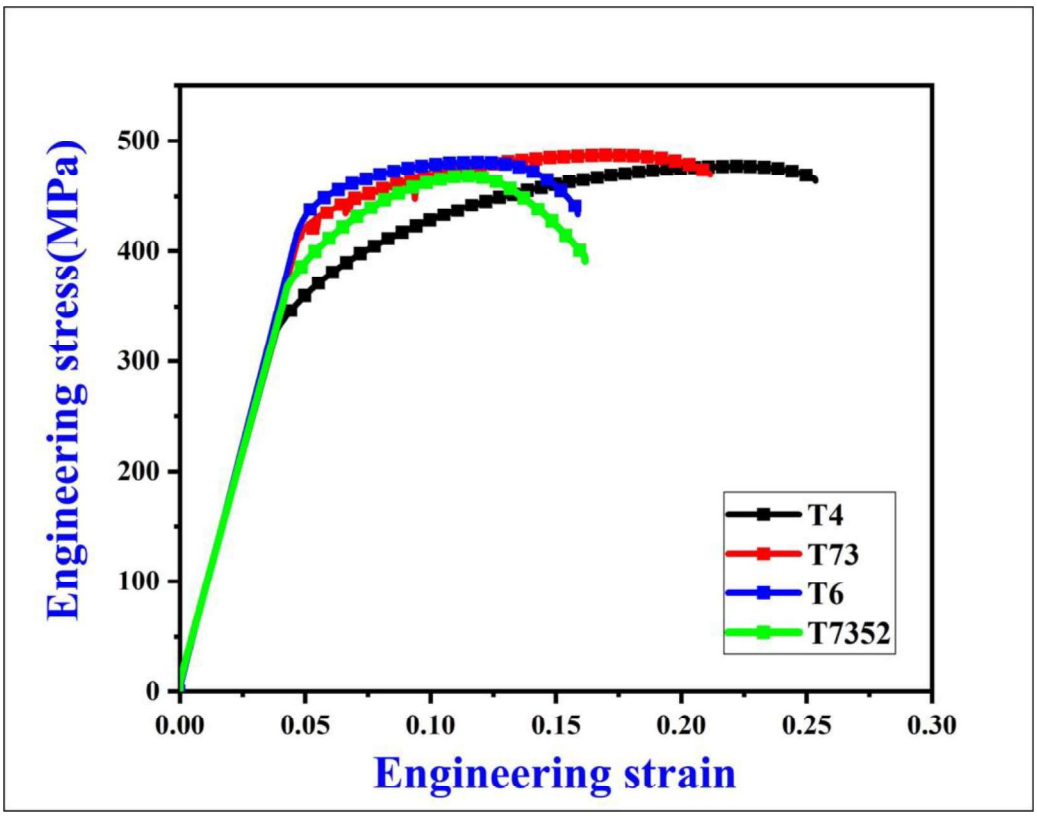

Fig. 3.28. Tensile properties: engineering stress-engineering strain behaviors of heat-treated alloy.

Respective tensile properties were determined following the standard procedures mentioned in the literature and their values are given in Table 3.5.

Table 3.5 Tensile properties of the heat-treated 7075 Al-alloy

Temper schedules	YS (MPa)	UTS (MPa)	%El (total)	UTS/YS
T4	384±4	468±5	25±2	~1.23±.05
T6	464±3	480±7	15±2	~1.03±.06
T73	448±5	485±1	21±1	~1.07±.04
T7352	425±7	472±6	18±3	~1.12±.09

3.2.3.7 Flow behaviors

Various relationships, proposed by Ludwik [61], Ludwigson [62], Hollomon [63], Swift [64], and Voce [65] are employed to study the flow and hardening behaviors of T4, T6, T73, and T7352 tempers and their details are given b

Hollomon Equation:

In the uniform strain regime, hardening behaviors with a single slope are determined using the Hollomon, [63] relationship given by Eq. 3.1.

$\sigma = K\varepsilon^n$ ……..……..Eq.3.1

Here, K is the strength coefficient, n is the work-hardening exponent, ε is a logarithmic plastic strain (ε_p), and σ depicts the true stress.

Ludwik Equation:

The Ludwik, added external stress term, σ_0 (yielding at lower strain) in the Hollomon equation to represent the flow behavior of those materials showing variation in yield-strength, uniformity in strain, and variation in strain hardening exponent (n) but similarity in yield-strength. The strain strain hardening behaviors of such materials are given by Eq. 3.2.

$\sigma = \sigma_0 + K\varepsilon^n$ ……..….Eq.3.2.

Where σ_0 represents the yield strength, K is the strength coefficient, ε is true-plastic strain, and n is the strain hardening exponent.

Ludwigson Equation:

Ludwigson [62], noticed that strain hardening behavior of FCC materials with low stacking fault energy, and austenitic stainless steel cannot be simply explained using the Hollomon relationship due to large deviation of stress during the tensile plastic deformation. Therefore, an additional term K_2 and n_2 were added in the Hollomon relation, to describe the deviation in the flow curve, given by Eq. 3.3.

$\sigma = K_1\varepsilon^{n1} + exp\,(K_2 + n_2\varepsilon)$ ……..……..Eq.3.3.

Where, K_1 and K_2 are the strength coefficients in a lower, and higher strain regime, n_1 and n_2 are respective strain-hardening exponents. The additional terms, K_2 and n_2 account for the large positive deviation in the flow curves from the lower strain regime to the higher strain regime, which is separated by a fixed plastic strain value, known as a true transition strain (ε_L).

Swift Equation:

The strain hardening behavior, of materials with pre-strain ε_0, can be given, after the addition of the pre-strain (ε_0) term in the Hollomon relation, which is given by Eq. 3.4.

$\sigma = K\,(\varepsilon_0 + \varepsilon)^n$ ……..……..3.4.

Where, ε_0 = pre-strain of materials, ε = logarithmic plastic strain.

Voce Equation:

The strain hardening behavior of alloys with saturation stress at higher stress/strain levels is explained using the Voce [65], relationship given by Eq. 3.5.

$\sigma = \sigma_s - (\sigma_s - \sigma_1)\,exp(n\varepsilon)$ ……..……3.5.

Where, σ_I is the true plastic stress, and σ_s represents the saturation stress of materials. Using the Levenberg Marquardt Least square regression method, the Eq. 3.1 to Eq. 3.5 were employed to fit the flow curves, and best-fitted flow curves are judged on the account of the least chi-square (χ^2) value (sum of squares of the deviation of calculated stress value from the experimental stress value), and highest Adj(R^2) value (coefficient of determination or goodness of fit).

Figs. 3.29a-d display log true stress vs. log true strain curves of the T4, T6, T73, and T7352 tempered alloys applying the mathematical models proposed by Hollomon, Ludwik, Ludwigson, Swift, and Voce for the curve fitting. All the curves depict an upward concave shape except applying the Hollomon and Voce relation for the fitting. The former gives the linear fit, but the latter results in much deviation from the experimental plot.

The T4, T6, and T73 heat-treated alloys show the best fitting with a Swift equation *($\sigma = K(\varepsilon_0 + \varepsilon)^n$, Figs. 3.29a-c)*. While, T7352 temper gives the best fitting with the Ludwigson equation *($\sigma = K_1\varepsilon^{n1} + exp(K_2 + n_2\varepsilon)$, Fig. 3.29d)* with two different sets of work hardening parameters. Strain hardening parameters of all heat-treated alloys were derived on the account of the best fitting with mathematical models, and given in Table 3.6.

Table 3.6 Work hardening parameters of the heat-treated 7075 Al alloy

Materials	**Strength co-efficient K, MPa**	**Pre-strain (ε_0)**	**Strain hardening Exponent (n)**	**Flow stress (MPa) $K(\varepsilon_0^n)$**	**Yield strength (MPa)**	**Adj(R^2)**	**Best fitting**
AA7075-T4	879	0.032	0.26	359	384±4	0.9934	Swift
AA7075-T6	773	0.025	0.18	400	464±3	0.99967	Swift
AA7075-T73	762	0.017	0.23	299	448±5	0.9983	Swift
AA7075-T7352	$K_1 = 695$ $K_2 = 6.02$		$n_1=0.59$ $n_2=-1.47$		425±7	0.99973	Ludwigson

The strength coefficient (K), and work hardening exponent (n) for T4 are 879 MPa, and 0.26 respectively. The pre-strain value of this material is 0.032 (Table 4). The measured flow stress (if $\varepsilon = 0$) using strain hardening parameter is 359 MPa. The strength coefficient (K), and strain hardening exponent *(n)* for T6 temper are 773 MPa and 0.23 respectively. The

pre-strain value (ε_0) of this material is 0.0254. The T73 temper gives a strength coefficient (K), of 762 MPa, and a work hardening exponent (n) of 0.18 respectively. The pre-strain value (ε_0) of this material is 0.017 (Table 4). The T7352 tempered alloy gives two different sets of strength co-efficient, K_1= 695 MPa, and K_2= 6.022 MPa, and work hardening exponent of n_1 = 0.59, and n_2 = -1.47. The Adj(R^2) values of all heat-treatments are close to 1 (0.9934 for T4, 0.99967 for T6, 0.9983 for T73, and 0.99973 for T7352), and chi-square values are least (67.2 for T4, 0.488 for T6, 2.35 for T73, and 2.65 for T7352) showing one of the best fittings of flow curves

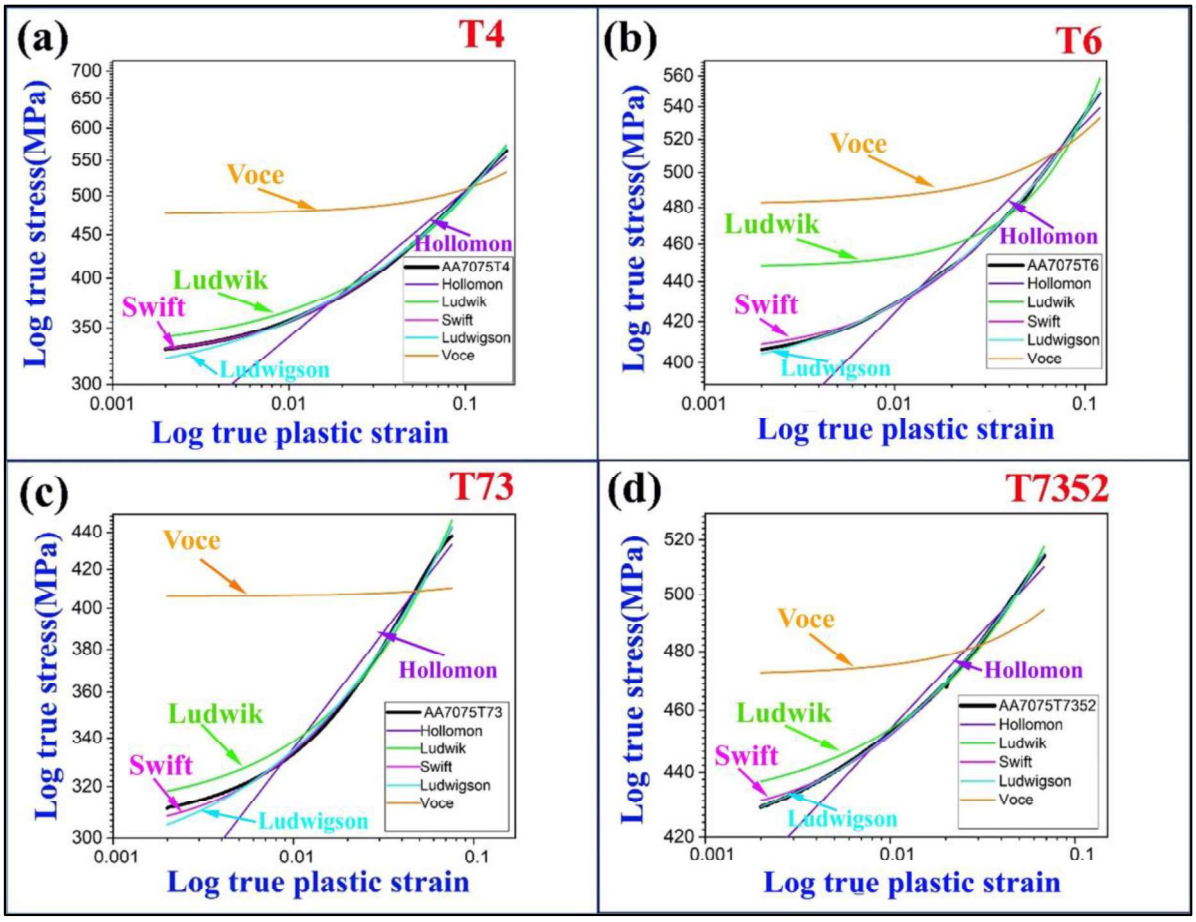

Fig. 3.29a-d. Logarithmic true stress vs. logarithmic true plastic strain curve (Log 10 scale): (a) T4, under-aged, (b) T6, Peak-aged, (c) T73, over-aged, and (d) T7352 temper, deformed after solution treatment and two steps of the aging treatment.

Strain hardening rate ***(Θ)***, of best-fitted Swift curves (T4, T6, and T73) can be obtained, after numerical differentiation of the Swift curve (Eq. 4) concerning the true plastic strain (ε_p) that is given by Eq. 3.6.

Strain hardening rate, $\boldsymbol{d\sigma/d\varepsilon\ (\theta)} = Kn(\varepsilon_0+\varepsilon)^{n-1}$…….....Eq. 3.6.

After, taking the natural logarithm of Eq. 6, the differential form can be summarized as:

$ln(\theta) = ln(kn)+(n-1)\ ln(\varepsilon_0+\varepsilon)$…… ……... Eq. 3.7.

Where, θ represents the work hardening rate, which can be obtained, by differentiation of true stress (σ) concerning true plastic strain (ε_p).

Figs. 3.30a-c display log-log plots of the work hardening rate $(d\sigma/d\varepsilon,\ \theta)$ and the corrected true plastic strain $(\varepsilon_0+\varepsilon)$ of T4, T6, and T73 tempered alloys (best fitted with Swift relationship $(\sigma = K\ (\varepsilon_0+\ \varepsilon)^n)$. All the alloys show three stages of hardening rate ($d\sigma/d\varepsilon,\ \theta$) concerning corrected true plastic strain $(\varepsilon_0+\varepsilon)$.

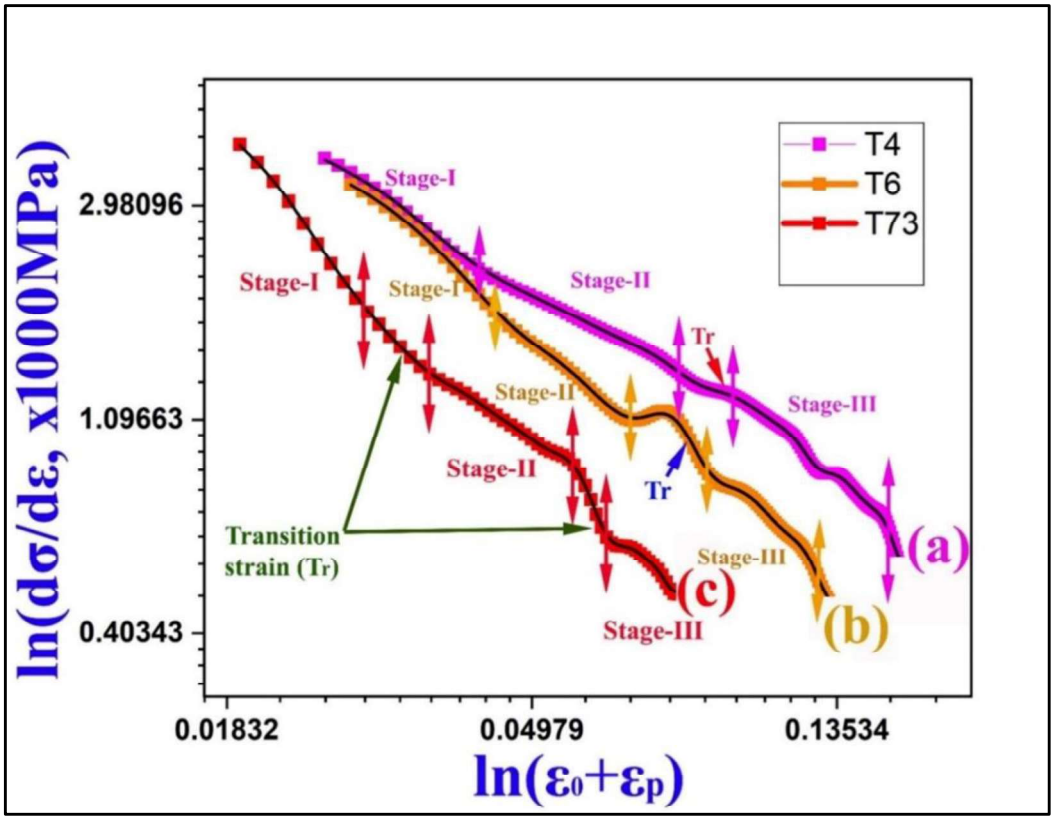

Figs. 3.30a-d Variation of logarithmic strain hardening rate *ln(dσ/dε, θ)* concerning logarithmic corrected true plastic strain ln*(ε0+εp)* : (a) T4, (b) T6, and (c) T73, (d) Strain hardening rate, *dσ/dεp (Θ)* concerning true plastic strain (*εp)*.

The magnitude of slope (n-1), transition strain (ε_r), and work hardening rate (Θ) in all three stages were determined, by applying the linear curve fittings, and the derived parameters are given in Table 3.7.

Table 3.7 Work hardening parameters of slopes, transition strain, and work hardening rates.

Materials	**Slope (n-1)**			**Transition strain (ε_r)**			**Work hardening rates (Θ, MPa)**		
	I	II	III	ε_1	ε_2	ε_3	Θ_1	Θ_2	Θ_3
AA7075-T4	-3.13	-1.5	-1.10	0.13	0.15	0.17	854	714	538
AA7075-T6	-1.39	-1.4	-1.56	0.04	0.07	0.11	1613	1041	795
AA7075-T73	-0.81	-0.41	-1.095	0.02	0.05	0.06	2772	1993	1447

For T4 temper, stage I depicts a gradual decrease in hardening rate (Θ) concerning corrected true plastic strain ($\varepsilon_0+\varepsilon$). Stage II further shows a decreased hardening rate, but their rate is slower than stage I. Stage III pertains to the softening stage, where the hardening rate (Θ) decreases gradually concerning ($\varepsilon_0+\varepsilon$) but at a rate faster than stage II. At the end of stage II, there is a transition strain (ε_r= 0.1552), and the magnitude of the slope in stage I (-3.13) is more than the slope of stage II (-1.5), and stage III (-1.08).

For T6 temper, stage-I shows a gradual decrease of hardening rate (Θ) respective to true plastic strain ($\varepsilon_0+\varepsilon$) with the transition stage at slightly higher true strain. Stage II, again shows a decreasing hardening rate (Θ), corresponding to ($\varepsilon_0+\varepsilon$), but the decreasing trend in this stage is sharper than the T4. There is a wide range of transition strain between stage-II, and stage-III beginning of which displays the transition true strain (ε) of 0.0715. Stage-III, again shows decreasing Θ concerning ($\varepsilon_0+\varepsilon$), and decreasing behavior is faster than the T4. The magnitude of the slope (n-1) in Stage I is -1.39, which is less than Stage II (-1.4) & Stage III (-1.56). The transition true strain (ε_r), after Stages I, II, and III are 0.0484, 0.0715, and 0.11 respectively.

In the T73 temper, a sharp decrease in stage I, with a wide range of transition strain (ε_r) at the beginning of stage II, is noticed. The hardening rate further decreases in stages II and III, but the rate is higher than the stage II. The magnitude of the slope (n-1) in stage I is -0.8, which is more than stage II (-0.41) but less than stage III (-1.095). The transition true strain (ε_r) at the end of stage I, stage II, and stage III are 0.024, 0.049, and 0.06 respectively. For T4 temper, the work hardening rate (Θ), at the end of stage I, II, and III are 854 MPa (Θ_1), 714 MPa (Θ_2), and 538 MPa(Θ_3). The hardening rates of T6 temper are Θ_1= 1613 MPa at the end of stage I, Θ_2 = 1041MPa, at the end of stage II, and Θ_3= 795 MPa, at the end of stage III. The T73 temper depicts a hardening rate of Θ_1 = 2772 MPa, Θ_2 = 1993 MPa, and Θ_3 = 1447 MPa,

at the end of stages I, II, and III. Fig. 3.30d shows strain hardening rate **($d\sigma/d\varepsilon$, Θ)** vs. true plastic strain ***(ε_p)*** plot of T7352 tempered alloy (best fitted with Ludwigson flow behavior). Three stages of hardening behavior are noticed in this. Stage I, displays a sharp/ concave shape decreasing behavior. Stage II shows slight dip and hump features. The stage-III depicts a linear decreasing trend. Work hardening rate(Θ), and transition true strain were calculated at the end of every stage. But slope and intercept values were calculated in stage III only, following the linear decreasing nature of the hardening rate (***Θ***) concerning true plastic strain ***(ε_p)***.

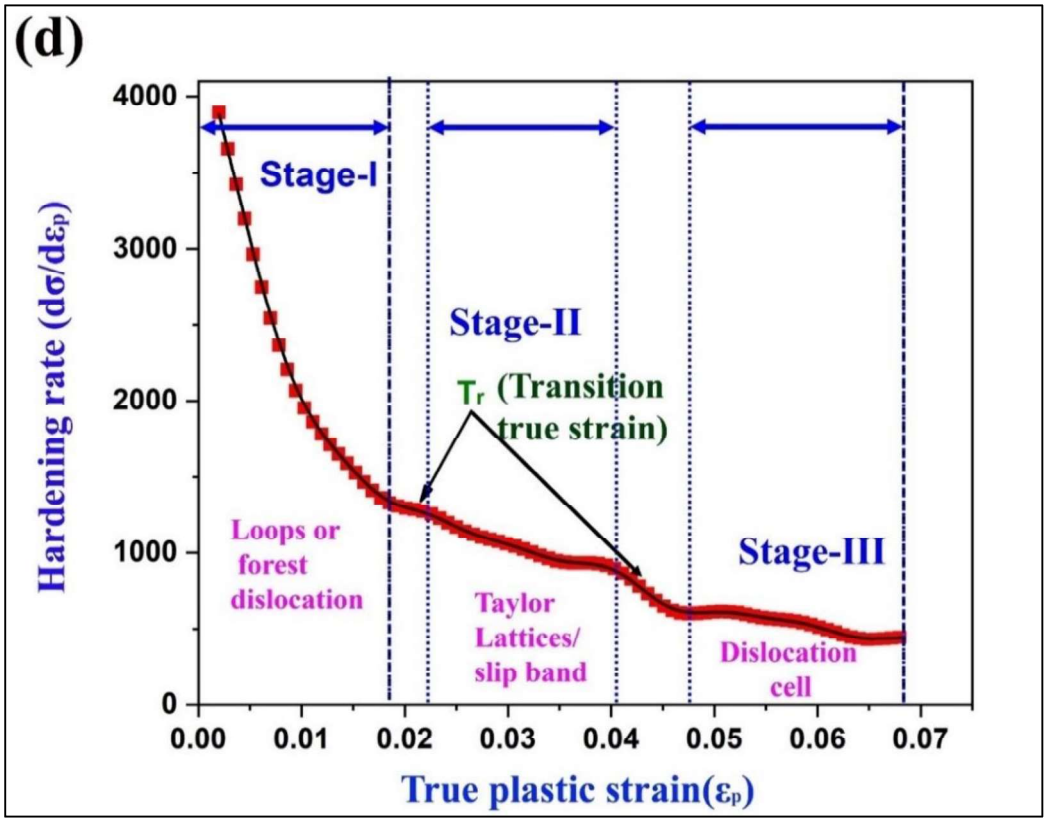

Figs. 3.30a-d Continued……

The calculated work hardening rate *(Θ)*, transition true strain *(ε)*, and slope, and intercept value of the linear fitted curve in stage III, are given in Table 3.8.

Table 3.8 Slope (*m*), and intercept of stage III, hardening rate (Θ), and transition true strain (ε_r) after every stage of Ludwigson fitted curve.

Materials	**Slope (*n*)& Intercept value**		**Transition true strain (ε_r)**			**Work hardening rates (MPa)**		
	Intercept (Θ_0)	Slope (*m*)	ε_1	ε_2	ε_3	Θ_1	Θ_2	Θ_3
AA7075-T7352	128415	-12967	0.019	0.042	0.062	1568	930	430

The magnitude of the slope of the linear fitted curve is -12967 (slope, *m*), and the intercept (Θ_0) is 128415. The work hardening rate, (Θ, $d\sigma/d\varepsilon$) at the end of stage I is 1568 MPa (Θ_1), and at the end of stage II is 430 MPa (Θ_2, *Table 7*). The transition true strain (ε_r) at the end of stage I is 0.019, which is found to be 0.062 at the end of stage II. The Adj(R^2) value of the linear fitted curve is close to 1 (0.9932 in stage 1 and 0.985 in stage 2), and the chi-square (χ^2) value is the least showing one of the best-fitted flow curves.

3.2.3.8 Fractography

Figs. 3.31a-d shows SEM secondary electron images of fracture surface of T4, T6, T73, and T7352 tempered 7075 Al alloys. Micro voids, dimples, and dimple ruptures were observed for T4 in Fig. 3.31a. The average size of dimples is less than 1±0.2 μm. Few regions, also contain micro dimples of size less than 0.02±0.005 μm. Fig. 3.31b, shows the fracture surface of T6 temper. The dimples, micro-dimples, and micro-voids are observed in most of the region. Added to this, transgranular crack is noticed in a few regions. The average size of dimples is 2.02 ±0.34 μm, and micro dimples with size of 0.45± .023 μm are densely distributed in some regions. Fig. 3.31c displays the fracture surface of sample T73. Micro voids, dimples, and dimple ruptures are seen in this. The average size of the dimple is 5.7± 0.92 μm, and microdimples are very small. The presence of the particle crack is also seen.

Fig. 3.31d shows the fracture surface, for T7352 temper. Dimples, microdimples, and dimple ruptures were noticed and their estimated size is 2.6±0.74 μm.

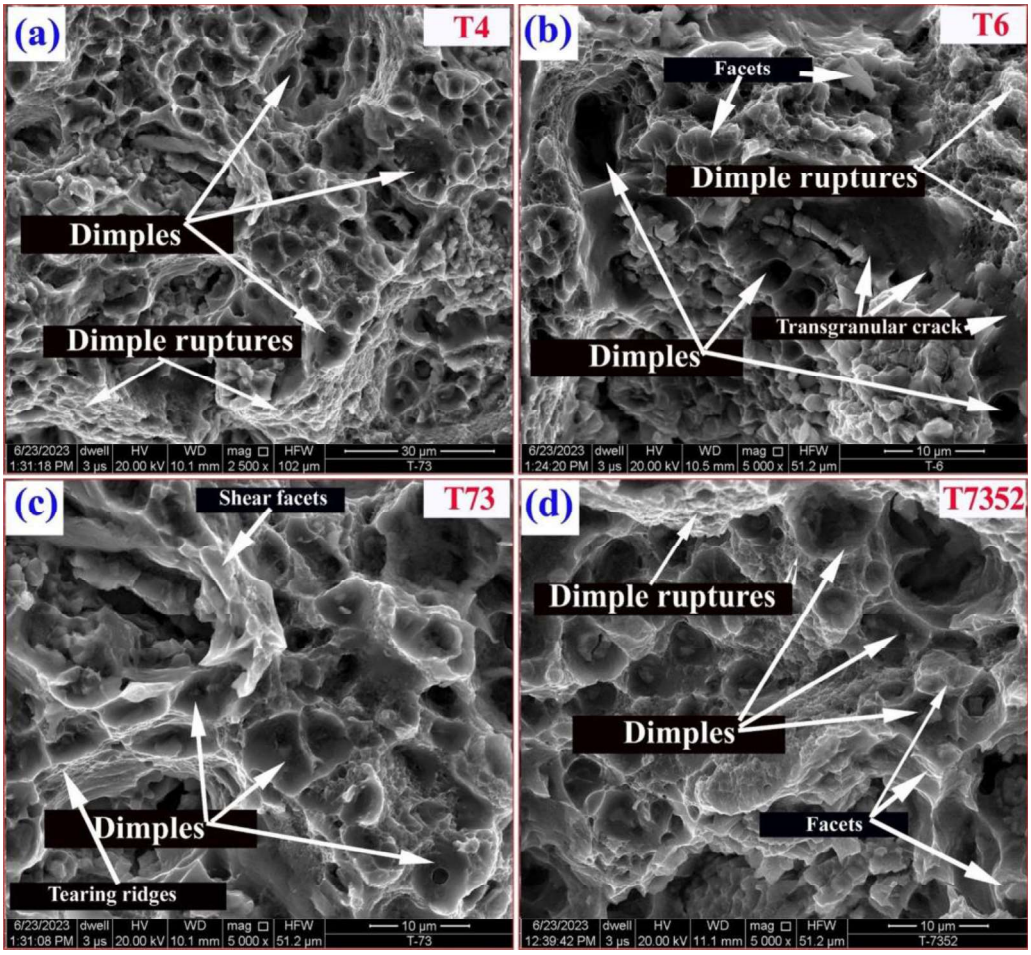

Figs. 3.31a-d. Fracture behavior, SEM secondary electron images: (a) T4, (b) T6, (c) T73, and (d) T7352 tempers.

Fig. 3.32 shows load vs. elongation curves of 7075 Al-alloys in T73, and T7352 temper conditions. The elongation (in mm) for T73 temper, in the 3.5 % NaCl solution is 10.6, but in the air is 12.5. For T7352 temper, elongation (in mm) of 3.5% NaCl solution is 9.8, but elongation (in mm) in the air is measured to be 11.5. Therefore, stress corrosion cracking susceptibility (*Iscc*) was calculated using Eq.3.8, and its values are given in Table 3.9.

Table 3.9 Stress corrosion severity of AA7075 at T4, T6, T73, and T7352 tempers

S.N.	Heat treatments	Elongation (mm, 3.5 % NaCl)	Elongation (mm, in air)	Iscc
01	T73	10.6	12.5	15.3
02	T7352	9.7	11.5	14%

$I_{scc} = 1-(\delta_{sol}/\delta_{air}) * 100\%$.....Eq. 3.8.

Among all the heat treatments, e.g. T6, T73, and T7352, tempers display the least stress corrosion cracking susceptibility and indicate the coarse grain boundary precipitate formation or dislocation entrapment in the interface of the η precipitates.

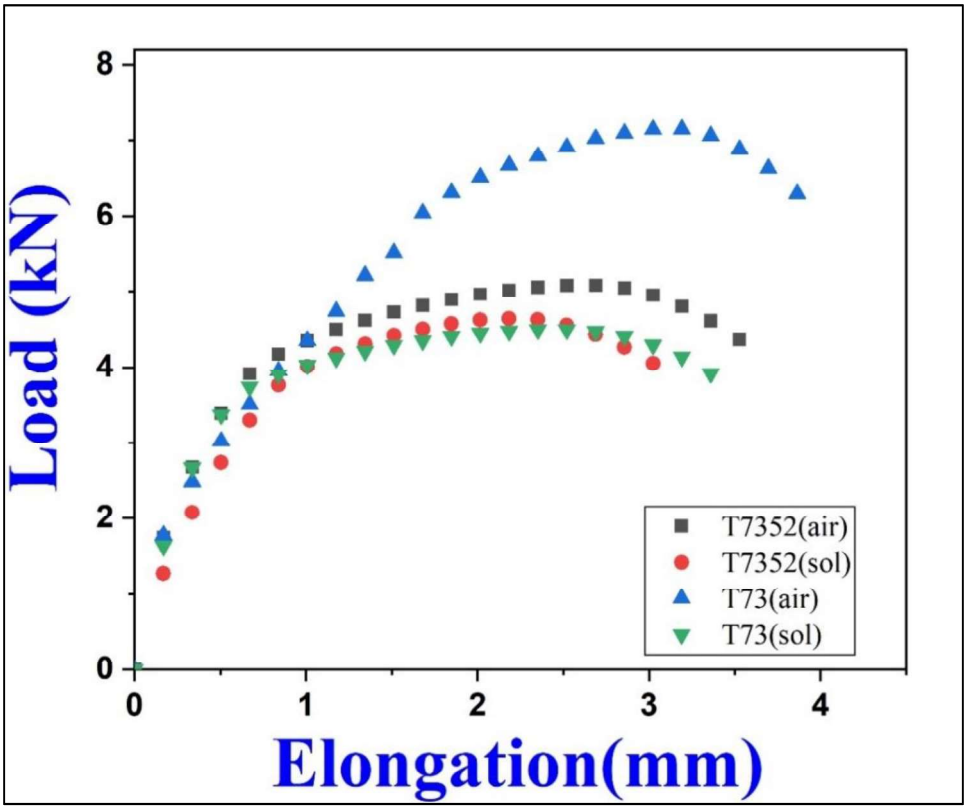

Fig. 3.32. Load vs. elongation behavior of AA7075, at T7352 and T73 tempers in the air, and 3.5% NaCl solution.

3.4. Discussion

3.4.1 Part I electron microscopy of precipitates in AA7075T7352 alloy

Formation of the metastable precipitates (η' and η) is related to solid-to-solid structural phase transformations of continuous type. The composition, and crystal structures of the parent phase (supersaturated solid solution (α)), and product phase (saturated (α)) remain the same as the transformations proceed. The metastable precipitates form on account of interfacial energy between the matrix-precipitate interface. The critical radius, for the nucleation barrier, in terms of the interfacial energy is given by the following relationship:

Nucleation barrier, $r^* = 16\pi\gamma^3 / 3(\Delta g)^2$…….*Eq. 3.9*

The GP zone is a coherent precipitate, and their interfacial energy is low in the range of 0.01 to 0.04 J/m^2. Therefore, nucleation of it starts at the beginning of the precipitation process, followed by the interfacial energy (0.04 to 0.08 J/m^2) of η' semi-coherent, and η (> 1J/m^2) in-coherent precipitates, displaying their nucleation in the intermediate and the final stages. The nucleation mechanisms have been involved in two separate types separated nucleation and in-situ nucleation. After the dissolution of precipitates (solution zing temperature of 470 ºC, for 1 hr), the matrix instantly becomes rich with supersaturated solute atoms, and new differently structured precipitates can separately nucleate elsewhere in the matrix, which is denoted as separated nucleation. Moreover, a new precipitate may gradually develop from the pre-existing precipitates and be found to be connected during their further transformations on account of the thermal effect of deformation. Therefore, the chemistry and lattices of the original precipitates are replaced by the new ones at the interfaces. This is known as the in-situ nucleation mechanism. The GP zone generally form in the low-temperature ageing (below<70 °C), by spinodal decomposition [121]. Whereas η' and η evolve at elevated temperature ageing (120 °C, for 24hrs) by diffusion-assisted nucleation

and growth process [74]. In the first type of transformation, long-range solute transport occurs, after a long period. Moreover, in the latter kind of transformation, sharp composition fluctuation emerges in a small period [76]. The dislocation collects solute atoms from the surrounding matrix and assists in the formation of new precipitates on the account of their chemistry by pipe-diffusion, and dislocation sweeping mechanisms [178,187]. Observation of rod types η' precipitates (L=50±5 nm, and W=18± 2 nm, Fig. 3.3a and c), showing preferred orientation along $2\bar{2}0$ of α-Al, is due to elastically soft direction assisted preferred nucleation. Most of the rod-like η' precipitates join in the interfaces after complete nucleation and increase their length in 5-fold magnitude (L=250±12 nm) along the preferred direction, in Fig. 3.3c. Such precipitates may change lattice structures at the interface and indicate in-situ nucleation-assisted η' precipitation [74]. The formation of such precipitates is due to enhanced solute diffusion, on account of increased quench in vacancy concentration [135]. Calculated high dislocation density using the XRD peak line broadening method, also supports the presence of dislocation in the α-Al matrix, which is a characteristic feature of 10% compressive deformation given during the alloy casting. Streaking along (Fig. 3.3b) along $2\bar{0}2$ of α-Al shows the presence of stacking fault-type homophase interface formation during nucleation of η precipitates [188].

The dark field TEM micrograph taken from streaking spots display plate/ strip type η precipitates (Fig.3.3d), showing preferred nucleation along the $2\bar{0}2$ of α-Al. The HR TEM images taken from η precipitates show zig-zag stacking sequence of RR^{-1}…. RR^{-1}…...RR^{-1} [74,148]. In total 13 layer of atomic column of η precipitates, the bright contrast in atomic column is due to high atomic mass of Zn, whereas dark contrast arises due to the less atomic mass of Mg. In the sequence of atomic column presence of fault is noticed due to the increased lattice misfit between the α-Al and η-$MgZn_2$ precipitate (Fig. 3.4a-c). The FFT

diffractogram taken from the faulted region displays clear streaking along $\bar{2}02$ of α-Al (Fig. 3.4b), and the facts reported in the literature [148] support the presence of stacking fault shown in Fig. 3.4c during nucleation of η precipitates. The analyzed chemistry from adjoining rods like η' precipitates and strip type η (in Figs. 3.5a-g) display the presence of precipitates rich in Zn and Mg confirming the η' and η precipitation. Intersecting η precipitates (at 90°,) are due to two different elastically soft directions of α-Al along 110 and 111 of α-Al, which may change lattices at the interface, and may form, homophase type of interface during their nucleation [74]. Chung et al. [189] further reported a twin boundary in the η precipitate of AA7050, due to in-situ nucleation-assisted η precipitation. Two differently oriented η precipitates join at the interface, and form twin-like boundaries during their nucleation process [74]. Two distinct orientations of η (Figs. 3.5a, c, d) show variants of η precipitates. The total 14 variants of η precipitates reported in combined works of Chung et al. [189], Marioara et al. [150], Xu et al.[151], and Bendo et al. [148], support variants of η precipitates in current investigation. The dark contrast of the η arises due to increased Zn concentration [74]. Moreover, feeble contrast emerges due to enhanced Mg concentration in the precipitates (Figs. 3.6a, c, d).

The mathematical relationship proposed by Nabarro [76] [58], mainly influences the shape of transition precipitates, which is given in Eq. 3.10:

$$\varepsilon = (2/3)\,\mu_m(\Delta V/V)^{2}\,\Phi(c/r) \quad \text{.....Eq. 3.10}$$

In this equation, μ_m is the shear modulus of α-*Al,* ΔV/V is changes in volume fraction, during structural phase transformations (SPT). The fractional volume change, associated with SPT highly influences the interfacial energy of metastable precipitates thereby the nucleation sequences. The function $\Phi(c/r)$ characterizes the shape of precipitates, Al-Alloy (Al-Cu system). The $\Phi(c/r)$ =1, shows formation of the spherical and rod-like precipitates

(considering oblate and prolate spheroidal particles with semi-axes r and c), $\Phi(c/r) << 1$, shows product phase formation with disc-like shape [68,76]. Some of the rod-like η' precipitates are differently oriented (4 different orientations) in the α-Al due to differences in the interfacial energy of lattice misfit during the nucleation process. The adjoining precipitates at the interface are possibly related to in-situ nucleation-assisted precipitation, whereas non-adjoining precipitates show separated nucleation-assisted η' precipitation, along two different elastically soft directions $\bar{2}02$, $\bar{2}\bar{2}0$, of α-Al in Fig. 3.3c, g. Such facts were also arising due to variations in the interfacial energy of the adjoining interface. Therefore, both in-situ nucleation and separated nucleation mechanisms are the possible cause of η' and η precipitation. The high atomic mass containing sharp Al_3Zr dispersoids is separately nucleated in the α-Al matrix. The lath morphology of precipitates was characterized as Al_2CuMg intermetallic, on account of the SAEDPs and morphology reported in the literature [46], which is separately nucleated along the elastically soft direction of $\bar{1}11$ of α-Al.

The group's theoretical point of view can be employed to study the morphology and number of precipitate variants [68]. The common point group between the matrix and precipitates is called the intersection point group. The η' has $P6_3/mmc$, space group belongs to the 6/mmm point group. The point group of the α-Al matrix is $m\bar{3}m$, with an order of 48. Symmetry elements of the intersection point group can be calculated from the orientation relationship between η' and the α-Al matrix. The resulting intersection point group is $\bar{3}m$, with an order of 12 for the η' and 4 in the case of the η precipitates. Therefore, the precipitate variants could be determined as the ratio of the order of the matrix point group to that of the intersection point group and result in the total 4 variants (48/12=4) of the η' precipitates. The morphology of the resulting η' resulting from the intersection point group of $\bar{3}m$ was

suggested to be the di-hexahedron shape, in the nucleation stage. The analyzed chemistry of transition precipitates (η' and η) using STEM EDS area mapping (Fig. 3.8a-f), and HAADF-STEM-EDS area elemental mapping (Figs.3.9a-g) display the presence of precipitates rich in Mg, Zn supports the analyzed chemistry of $MgZn_2$ (η' and η) in the current investigation. Moreover, the spectrum mapping of precipitates with a light and dark contrast show the formation of precipitates rich in Mg, Zn, and Cu suggesting different chemistry of precipitates.

The appearance of Moire fringes (in Fig.11a, c, e) arises due to interference between a pair of the diffracted electron beams, g_1 and g_2 due to the presence of a defect [190]. If g_1 is generated in the upper crystal/ plane, and g_2 in the lower crystal, then reflection g_1 in the first crystal acts as an incident beam for the lower crystal and gives the DPs attributed to plane2/ crystal 2 around the g_1. Such interference, in the electron beams also causes double diffraction. The twinning spots observed in the FFT pattern of Figs. 11b and d, support, formation of rotational moire fringes. The spacing between two moire fringes gives the lattice a misfit. Lattice misfit between the matrix and precipitates also governs the shape and nature of precipitates. The increased spacing displays enhanced lattice misfit and thus pertains to the formation of incoherent (η) precipitates (region 1), with slightly reduced spacing depicting semi-coherent (η') precipitate formation [190].

3.4.2 Part II effect of tensile strain on the precipitation and dislocation behaviors of AA7075T7352 alloy

Analysis of the XRD patterns of the as-received specimen (Fig. 3.12a) ensures presence of the transition precipitates of η' and η along with the intermetallic of Al_2Cu *(θ)* in the solid solution phases of the α-Al. Reduction in the intensity of η and η' precipitates at 0.02 tensile true straining are attributed to partial dissolution of phases (Fig. 3.12b). Whereas, the

disappearance of the η peak at 2θ=20°, at tensile true strain corresponding to the 0.06 pertains to the complete dissolution of the η (Fig.3.12c). Re-appearance of the low-intensity XRD peak of η at 2θ= 20° and 2θ= 42° and η' and η diffraction peak supports the re-precipitation of the η' and η phases (Fig. 3.12d, h). Analyzes of the precipitate's morphologies and their SAEDPs~ in as-received material (Figs. 3.13a-b) confirm the presence of *η'* (rod) and *η* (plate) precipitates in the *α*-Al matrix which is the most commonly observed second phase particles in the 7xxx series Al-Alloy [5,32]. 3rd –order lattice multiplicity of 220 spots of α-Al with respect to η of the $MgZn_2$ phases support the co-existence of η spot into the 220 spots of α-Al. Sharp change (330 nm to 65 nm, Table 2***)*** in the size of spherical precipitates (Fig. 3.13c), at 0.02 tensile straining, indicates nearly 80% or complete dissolution of the η. On the other hand, a change in the size of the *η'* precipitates (L= 380 to 150 nm and W= 180 to 85 nm, Table 2) confirms nearly 50% or partial dissolution of the phases. No obvious change in the size of the *η($MgZn_2$)* precipitate supports shear resistant nature of the phases. Low-intensity diffraction spots of the *η* as well as 220 of α-Al and *η'* phases (Fig.3.13d), also depict dissolution of the η' or η. It was observed that dislocation entrapment into the plate and rod type phases (Fig. 3.13e), at 0.06 tensile true straining reveals the shear-resistant nature of the *η', and η p*hases.

The absence of the spherical precipitates indicates the complete dissolution of the GP zones. The non-appearance of diffraction spots of the η' and η phases (Fig.3.13f) also shows the entrapment of the precipitates by dislocation. The formation of many small spherical precipitates in the size range of 10 nm to 15 nm, as encircled in white (Fig. 3.13g), is in great agreement with the dynamic formation of the η'*(*$MgZn_2$). Whereas, a reduction in the size of η'*(*$MgZn_2$*)* phase also supports the dissolution of the phases. Further, no obvious changes in the size of the *η* ($MgZn_2$) precipitate depict the resistant nature of the phase. Similar nature

of the $\eta'(MgZn_2)$ and $\eta(MgZn_2)$ phases were also reported in the literature [178,191,192]. Randomly distributed large numbers of the low-intensity DPs (Fig.3.13h) also support the dynamic formation of the precipitates or partition of the solute atoms. Whereas one of the very high intensity 220 diffraction spots of α-Al, as encircled in white, indicates a growth of spherical precipitates. The two opposing effects of precipitate dissolution and the dynamic formation of small spherical precipitates were revealed (Figs. 3.13b-d). These could be best explained by the time of subsequent dislocation arriving at the precipitates/second phase particles. If time is less, η'/η gets dissolved due to shear-induced dislocation. On the other hand, if the time is sufficiently large, the new spherical precipitates are formed by the dynamic partition of solute atoms. The nucleation is assisted by dislocation, but growth is achieved through pipe diffusion and solute transport by sweeping mechanisms. Similar mechanisms are also reported in the literature in the case of the Al-Cu and the 7xxx series of Al alloy system [177,178]. Dissolution of the phases may be either dislocation shear (strain) induced or pertaining to the thermal activation. Therefore, one needs to understand the associated mechanisms behind this. The amount of heat released due to internal friction between atoms during monotonic tensile loading is related to the function of the applied strain. However, in the current study maximum of ~0.1 tensile training (corresponding to a true strain of 0.1) is given to the materials which is not enough to release sufficient heat required for the dissolution of the η', considering the facts reported in the literature [178]. Therefore, the present investigation shows the dislocation-shear-induced dissolution of the phases. The stress corrosion cracking (SCC) behavior of the alloy is analogous to the microstructure evolution during mechanical operation. Therefore, an investigation of the SCC behavior of the alloy is also needed.

The literature stated that either the dissolution of some of the phases or the formation of the new phases, their growth, and coarsening improves the stress corrosion cracking performance of the alloy [4]. Therefore, the dissolution of the η'/η at the 0.02 and 0.06 tensile true straining (Figs. 3.13c,e) as well as nucleation and growth of the new spherical precipitates, from the dynamically partitioned solute atoms [177,178], at 0.1 tensile true straining (Figs. 3.13b-d), noted in the current investigation would be helpful to improve the stress corrosion cracking (SCC) as well as the other mechanical performances of the alloy [4]. More negative corrosion potential values of $MgZn_2$(η), Al_2CuMg, and Mg_2Si phases confirm the anodic behavior respective to the α-Al. Whereas, the positive corrosion potential value of Al_7Cu_2Fe phase ensures the cathodic behavior respective to it. Hence, the presence of the η ($MgZn_2$) precipitates at various amounts of tensile straining (Figs. 3.13a,c,e,g) should reduce the corrosion performance of the alloy [91]. However, observed dislocation entrapment at the *η'* and *η* phases (Figs. 2c, e) make them isolated and changes their nature from anodic to cathodic. Isolation of η phase by dislocation entrapment, at tensile true straining of 0.02 and 0.06, (Figs. 3.13c, e) makes the alloy stress corrosion cracking (SCC) resistant and improves the performance of the alloy for structural applications. Dislocation-assisted isolation of *η*($MgZn_2$) phase in the retrogression and re-aged (RRA) state as reported in the literature [4,91] is also a great agreement with the present Investigations. The diffracted g-vector at 0.02 tensile true straining (Fig. 3.14a), with the d-spacing value of 2.33Å, was confirmed as 111- diffraction vector of *α*-Al. On the other hand, at 0.06 and 0.1tensile true straining (Fig.3.15a, and Fig.3.16a) the g-vectors correspond to the d-spacing value of 2.02Å and 1.43Å respectively were found to be 200 and 220 (PDF#85-1327). The projected Burger vectors of dislocation (Fig. 3.17) follow invisibility criteria, g.b = 0. Burger vectors (b) were also characterized in a similar way in the literature [134]. Formations of

dislocation loops (Figs.3.14b, d) at 0.02 tensile true straining, are the characteristic features of low to medium hardening. On the other hand, high-density dislocation tangles and forest dislocation (Figs. 3.14c,e) are the characteristic deformation features of high hardening[92,193]. Similarly, low-density Taylor lattice and dislocation cells observed (Figs. 3.15b, d and Figs.3.16b, d) at tensile true straining of 0.06 and 0.10 respectively are the characteristic deformation behavior in the low strain regimes. Whereas high-density Taylor-lattice and dislocation cell structures can be seen (Figs.3.15c,e, and Figs. 3.16c,e) at the tensile true straining of 0.06 and 0.1 respectively are characteristics of deformation behavior in high strain regimes [95,193]. Therefore, characteristic dislocation structures in high strain regimes as mentioned above (Figs. 3.14c,e Figs. 3.15c,e and Figs. 3.16c,e) strongly hinder the motion of the mobile dislocation by activating the multiple slip systems or trap the mobile dislocation inside the dense dislocation walls (DDWs/ cell structures) [95,194]. Therefore, dislocation experiences very high hindrance passing through the α-Al, which finally, causes very high hardening during the plastic deformation. One also noticed three stages of the dislocation re-organization/ re-arrangement during the tensile true straining. For examples, dislocation loops to the tangled dislocation, in the first stage, Tangled dislocation to the Taylor lattice structures, in the second stage, and Taylor lattice structures to the dislocation cell structures (Figs. 3.14 to 3.16) in the third stage. This is due to mutual interactions and re-organization of the dislocation structures during the partial tensile straining of the alloy [96]. A high UTS value as compared to the YS (Table 3) shows that materials can sustain maximum load during plastic deformation. This happens due to the evenly distributed micro-voids and dimples as shown in the fractography (Fig. 3.20b) of specimen D_1. The alloy, AA7075T7352 has been developed to get a high ratio of UTS to YS. Nearly, 2 to 3% compressive deformation is given to the alloy after solution quenching,

at T7352 temper, which reduces the peak hardening ability of the alloy [90] that decreases the yield strength sharply. Finally, reduced yield strength, without making any significant changes in UTS gives a high ratio of the UTS to YS, which is desirable for applying the materials to engineering structural applications. The presence of dip and hump in the engineering stress-engineering strain and true stress-true strain curves (Figs. 3.18a-b) are due to in homogeneously distributed precipitates/ second phase particles that block the motion of dislocation. A sharp change in the slope of the log-log plot of true stress vs. true strain curve (Fig.3.18c) indicates the two-slope deformation characteristics of the alloy. One noted, Ludwigson flow behavior of the failed specimen D_1(Fig. 3.18d) applying the curve fitting method. The Adj (R^2) value of the fitted curve is very close to 1(0.99678). This indicates one of the best fittings of the flow curve. Optimum fitting of the Ludwigson relationships attributed to the two-slope deformation characteristics of the alloy, which also depicts two distinct deformation mechanisms during tensile plastic deformation. Flow behavior with two-slope characteristics was first ever noticed by the D.C. Ludwigson in the year 1971 in austenitic stainless steel and other f.c.c. based alloys[172]. The planar flow of the dislocation was related to the low-strain regimes. Whereas, cross slip and dislocation cell formation were attributed to the high strain regimes[172]. They also modified the Ludwik relation *($\sigma = K\varepsilon^n$)* to extensively describe the plastic flow behavior of the materials. The modified relation is known as the Ludwigson relation which is given by Eq. 3.11 as [172]:

$$\sigma = K_1\varepsilon^{n_1} + exp\ (K_2 + n_2\varepsilon) \quad \text{.....Eq.3.11}$$

The mathematical terms k_1 and n_1 in Eq. 1 depict the strength co-efficient and hardening exponent in the high strain regime. Whereas, k_2 and are similar terms of the low strain regimes, which also describe the positive departure of the flow curve from the Ludwik - relationship. Further, Banumathy et al. [195] reported two-slope deformation characteristics

in the Ti-16Nb alloy, based on phase transformation. The transformation of β to α'' phase is attributed to the low strain regimes. Whereas, deformation of the prior α'' phase is related to the high strain regimes. Mehta et al. [180,181] reported two-slope deformation characteristics based on texture behavior and strain localization. Low-strain localization along with the formation of annealing twins is related to the low-strain regimes. Whereas, high strain localization, along with the deformation twins are of the high strain regimes. Dislocation-assisted two-slope characteristics were also reported by the authors [90,196]. Therefore, an investigation regarding the cause of two slope deformation characteristics in this work is needed. Formation of the dislocation structures and analysis of the precipitation behavior indicate that dislocation may be the major cause of two slope deformation characteristics. Therefore, systematic dislocation characterization was done using the bright-field (BF) and weak-beam dark-field (WBDF) TEM imaging techniques. Observed dislocation structures also support two slope deformation characteristics of the alloy which is confirmed by the Ludwigson curve fitting method in Fig. 3.18d. Hence, at 0.02 tensile true straining, the first stage of the two slope characteristics relates to the formation of dislocation loops (Figs.3.14b,d). Forest dislocation and tangled dislocation formation in Figs. 3c, e is pertaining to the second stage. Further, at 0.06 tensile true straining first stage is attributed to the formation of low-density Taylor-lattice structures (Figs. 3.15b, d). The high- density Taylor- lattice structure (Figs. 3.15c, e) is ascribed to the second stage of two-slope characteristics. Similarly, at 0.1tensile straining, the first stage is related to the formation of the low-density dislocation cell structures (Figs. 3.16b, d). The high-density dislocation cell structures (Figs. 3.16c, e) are pertaining to the second stage. The particular value of strain, which separates the deformation mechanisms from low strain regimes to the high strain regimes is known as the transition true strain that is denoted by ε_L. After these, materials

typically display deformation mechanisms of the Tangles dislocation, high-density Taylor lattice, and dislocation cell structures as noted in the different levels of straining (Figs. 3.14c, e, Figs. 3.15c, e, and Figs. 3.16c, e). Noticed- dislocation loops, low-density Taylor-lattice, and dislocation cell structures (Fig.3.14b, d, Fig. 3.15b, d and Fig. 3.16b, d) at 0.02,0.06, and 0.1 tensile straining shows that dislocation bypasses with less hindrance through the α-Al matrix. These cause low hardening. Whereas, the formation of forest dislocation, high-density Taylor-lattice, and dislocation cell structures (noted in Figs. 3.14c-e, Figs.3.15c-e, and Figs.3.16c-e, at a tensile true strain of 0.02, 0.06, and 0.1 respectively) activates the multiple slip systems. Therefore, dislocation experiences high hindrance passing through the α-Al matrix which causes very high hardening. A sharp decline in the hardening rate $(d\sigma/d\varepsilon)$ versus the true plastic strain (ε_p) curve in 1st-stage of Fig.7e is due to the formation of the dislocation structures [25]. This is attributed to the single slip system. The formation of dislocation loops and forest dislocations are characteristic micrographic features in this stage [92,95]. The sharp increase in hardening rate supports the transition from 1st -stage to 2nd-stage. The dip and hump nature in this stage indicates, obstruction in the motion of the dislocation [95]. The formations of slip band/ Taylor-lattice or checker-board type structures are the characteristic deformation features in this stage [197,198]. Similarly, formations of dislocation cell structures are attributed to the hardening behavior in the 3rd –stage. These, also support the linear decline of the flow curve. The linear relationship between the hardening rate versus true plastic strain curves in the 3rd-stage (Fig. 8) could be best explained with the help of *Kock, Mecking, and Esterin*, *(KME)* [199–201] based dislocation models [90,180] which are given by the linear Eq. 3.12.

$n = d\sigma/d\varepsilon_p = \theta_0 + m\sigma$ ……*Eq. 3.12.*

Here, n is the strain hardening rate of the materials and σ is the true stress. On the other hand, the term, m pertains to the slope of linear regimes, whereas, the constant θ_0 is related to the dislocation storage term. Parameters are derived using Eq. 3.12 and one noticed that the Adj(R^2) value of the fitted curve is nearly 1(~0.9987). This indicates one of the best fittings of Eq.2. A high value of θ_0 indicates a high dislocation storage capacity. In contrast, a high negative value of "m" displays a low dynamic recovery. The formation of high-density dislocation cell structures also supports the low dynamic recovery. Observed facet fracture in the fractography of specimen D_1 (Fig. 3.20a), indicating the brittle mode of failure. On the other hand, the formation of dimples and micro voids as well as those of particle cracks (noted in Fig. 3.20b) indicate the ductile failure mode. Moreover, a dimple rupture (Fig. 3.20c) is related to the coalescence of the micro-voids and dimples. Therefore, deformation mechanisms are related to the three stages, these are 1. Nucleation, 2. Growth, and 3. Coalescence of the precipitates. Fractured tensile specimen, D_1 belongs to the same batch of heat-treatment (T7352 temper). Therefore, one should not see any variations in the failure mechanisms. However, mixed ductile and brittle failures (Figs. 3.20a-c) are due to the presence of the various nature of metastable (η' and η) precipitates (Fig. 3.12a-h), and intermetallic of the Al_2Cu (θ), Al_2CuMg [90] that may also support various deformation mechanisms.

3.4.3 Part III microstructure evolution, texture characteristics, mechanical properties, and flow behaviors of the AA7075 at T4, T6, T73, and T7352 tempers

The absence of XRD peaks of transition (GP zone, η', and η) precipitates in the 7075 Al alloy for the T4 temper (Fig. 3.21a), arises because room temperature aging (30°C) is not enough for thermally assisted decomposition of solid solution (α) from the supersaturated solid solution (SSSS(α) [202]. In the peak-ageing (T6 temper, Fig. 3.21b) state, the

formation of the transition precipitates (η' and η) is attributed to the fact, that elevated temperature ageing (120°C, for 24 hrs) which is sufficient for the diffusion assisted nucleation and growth of precipitates [76]. Changes in the lattice parameters of α-Al (111), and shifting of the XRD peaks towards the left also support the formation of metastable precipitates. The absence of GP zone, in a XRD pattern, and TEM micrograph of T73 temper (Fig. 3.21c) arises due to thermally assisted dissolution (second stage ageing at 180 °C, for 30hrs) of the GP zone [203] because the thermal stability of GP zone is limited upto 150 °C [178]. No changes, in the XRD peak intensity of η' and η, and evolution of the rod and plate type precipitates are attributed to high thermal stability.

Observations of the XRD peak of η, close to 2θ peak position of 20° (d~4.24 Å) for T7352 temper (as shown in Fig. 3.21d) shows, re-precipitation of η (PDF#77-1177 & 652504), with same crystal structure, but different chemistry. Shifting of the η peak (Fig. 2d), towards the left in comparison to T6 tempered alloy supports the η precipitation with a different chemistry. At 10% compressive deformation (T7352 temper), dislocation density increases in the Al matrix, which promotes precipitation of the η due to increased solute diffusion and dislocation sweeping mechanisms after the subsequent stage of ageing [24,48]. The lattice parameter (a = 4.1 Å) of both α-Al and GP zone was nearly identical, with only 3.5% lattice misfit, resulting in a coherent interface. In contrast, the increased lattice misfit of 17% between η' and α-Al, and 25% lattice misfit between η and α-Al support the formation of semi-coherent (η') and incoherent (η) hetero-phase interfaces, respectively [68].

Compared to the other heat treatments, the higher calculated dislocation density of T4 temper arises due to solute supersaturation in α-Al. These lead to lattice mismatch between α-Al and the solute atoms and create the micro-strain increasing the dislocation density [1]. Furthermore, if the temperature is raised to 120°C for 24 hours (at T6 temper) or when

employing the over ageing (120°C for 24 hrs, and 160°C for 30 hrs, at T73 temper), the dislocation acts as a driving force for the formation of a transition (η' and η) precipitates. These support reduced dislocation density at T6 and T73 tempers. The thermal exposure associated with the T6 and T73 tempers promotes the recovery mechanisms [1], which may be another cause of decreased dislocation density. Further, slightly increased dislocation density for T7352 temper), as compared to T6, and T73 arises due to 10% compressive deformation [49,50]. Heat treatment does not change the texture significantly, and the evolution of the recrystallization textures is noticed in most of the literature [21,45]. Therefore, development of the Goss {011} <100> re-crystallization textures with same intensities (x 15R) are observed at T4, T6, and T73 tempers (Figs. 3.22a-c). Moreover, compressive deformation (10%) dominated S {123} <634>, Brass {011} <211>, and Cube {001} <100> deformation texture components were formed, added to the Goss {011} <100>, re-crystallization textures at T7352 temper (Fig. 3.22d). Such texture evolution changes the deformation mode by changing the slip systems thereby causing high hardening [204]. Moreover, intense (x 21R) Goss {011} <100> re-crystallization texture (at T7352, Fig. 3.22d) creates twist angle grain boundaries between Goss{011}<100> oriented grains, and the nearby grains [42], thus making crack propagation torturous, thereby improving mechanical and SCC performances [205–207]. Therefore, materials typically display recrystallization texture in T4, T6, and T73 tempers. In addition to this, the presence of the deformation textures S {123} <634>, and R-Cube {100} <011>, in T7352. Sharp crystalline, 220 XRD reflection of α-Al, at T4, T6, and T73 tempers (Figs.3.21a-c) show no variation of preferred crystal orientation, thereby texture components (Figs. 3a-c). Whereas sharp crystalline 220 peaks of α-Al (at T7352 temper, Fig. 3.21d) support texture changes from re-crystallization to deformation texture due to 10% compressive deformation.

The relationship between grain size and yield strength was described using the Hall-Petch relationship given by Eq. 3.13 [122]:

$\sigma = kd^{-1/2}$…..……..…*Eq. 3.13*

Where σ represents yield strength, k is the Hall-Petch constant, and d is the grain size of the heat-treated alloy. Consequently, if grain size remains similar (46±5 μm, Fig. 3.22a-c) for T4, T6, and T73 tempers, there will not be any significant changes in the yield strength of the alloys. Hence, variation in the yield strength of alloys mainly emerges due to changes in the size of precipitates (Table 2). Notably, the grain size of T7352 temper is smaller (Fig. 3.23d), compared to other heat treatments should result in higher yield strength, but precipitation mainly causes strengthening in 7xxx series Al alloy. Hence, reduced YS and UTS, in this state, may arise due to enhanced formation of soft phases (Fig. 3.21d). Due to its small size and coherence, the soft phase does not impede the dislocation motion significantly, thus reducing the YS and UTS (Table 2) [208]. Arafin et al. [209], reported that low-angle grain boundaries are crucial in preserving corrosion resistance and resistance to stress corrosion cracking. Additionally, these may also influence the hardening behaviors of the alloy. The high-angle grain boundaries were more susceptible to corrosion [64]. Consequently, the higher proportion of low-angle boundaries (F_{lagb} ~74%) observed in the T7352 temper (Fig. 3.24d) concerning other heat treatments is likely to enhance the mechanical properties and resistance to stress corrosion cracking (SCC). Chen et al. [31] [50], also corroborated such findings in their research, providing further support for the current investigation.

The spherical, rod-like, and plate-type precipitate morphology is attributed to the characteristic features of GP zone (spherical, morphology), η’ (rod, morphology), and η (plate, morphology) precipitates [46,122,149]. Such analyses are made on account of the

SAEDPs and reported precipitate morphology in a few pieces of literature [46–48,68,149]. Therefore, the absence of the spherical (GP zones), rod (η'), and plate (η) type precipitates for T4 temper (Fig. 3.25a), emerges because room temperature (~25°C) is not enough for the precipitation. The absence of weak-diffraction spots (Fig. 5b) of precipitates also supports the investigation. For T6 temper (aging at 120°C for 24 hours), evolution of η', and η (Fig. 3.25c) arises because peak ageing (120 °C, for 24 hrs) is sufficient for matrix and grain boundary precipitation. The presence of weak DPs~, marked by the arrow, also confirms the evolution of the η' (rod-like) and η (plate-like) precipitates [46]. It is important to note that the η shows 3rd-order multiplicity with the d-spacing value of 220 of α-Al (where, η (d ~4.29Å) = 3*d220 (1.43Å)), resulting in the η spots coinciding with the 220 spots of α-Al. The interfacial energy barrier between the matrix precipitates interface plays a crucial role in determining the sequence of nucleation of precipitates, which is summarized in Eq. 3.14 [71,183]:

$\Delta G^* = 16\pi\sigma^3 / 3(\Delta g)^2$ ……..……..Eq. 3.14.

Here, σ is the interfacial energy between the matrix-precipitate interfaces. The GP zone forms a coherent interface with α-Al, and their interfacial energy is very low, in the range of 0.01 to 0.05 J/m² [23]. Therefore, GP zones form early in the precipitation process. Moreover, the η phase (Laves phase of C14 type) has an incoherent interface, and their interfacial energy is high in the range of 0.4 to 1.0 J/m² [23]. The high interfacial energy causes a substantial barrier to the nucleation of precipitates, thus resulting η phase formation in the last stage of the precipitation process. Semi-coherent η' has interfacial energy between the GP zone and η phase, ranging from 0.1 to 0.3 J/m² [23]. Thus, its nucleation occurs in the intermediate stage. Therefore, the precipitation sequence in the current investigation can be summarized with the help of Eq.3.15 as [58]:

Supersaturated solid solution (SSSS, α) → *GP zones* (coherent) →*η'*(semi-coherent) →*η* (in-coherent)…….. …….....*Eq. 3.15*

The mathematical relationship proposed by Naborro [58] mainly helps to determine the shape and morphology of precipitates, which is summarized in Eq. 3.16:

$\varepsilon = (2/3)\,\mu_m(\Delta V/V)^2\,\Phi(c/r)$ ……..……*Eq. 3.16*

Where μm = shear modulus of α-Al, ΔV/V = fractional volume change associated with the structural phase transformations. The function, $\Phi(c/r)$, mainly determines the shape of precipitates. For instance, $\Phi(c/r)$ =1 shows the evolution of spherical and rod-like precipitates (considering oblate and prolate spheroidal particles with semi-axes r and c). In contrast, Φ(c/r) <<1 depicts the formation of the product phase with a disc shape [58, 75]. As a result, the rod-shaped precipitates depict the formation of η', but plate morphology shows the evolution of η precipitates. At T6 temper (Fig. 3.255c), rod-like precipitates depict η' phase, and plate-type precipitates display η precipitates. The coarsening of these precipitates at the T73 temper (Table 2, Fig. 3.25e) can be attributed to a two-step ageing process involving ageing at 120°C for 24 h and over-ageing at 160°C for 30 hours. The second stage, ageing, promotes the growth of these precipitates [59]. A slightly reduced precipitate size at T7352 temper is due to 10% compressive deformation. The deformation increases the dislocation density, resulting in the fast nucleation of precipitates, thus reducing the size. The weak spots marked by a white arrow in Fig. 3.25c, e, g (at T6, T73, and T7352) support the formation of a η' and η phases. Changes in the size and chemistry of precipitates in the T6 and T73 tempers (Table 2, Figs. 3.25c and e) are due to the aging-assisted thermal process. Moreover, the size of phases at T7352 temper changes due to the combined effect of a deformation-assisted dislocation environment and an ageing-induced thermal process. Re-precipitation of the η, with different chemistry but the same crystal structure, at T7352

temper (Fig. 3.25g), is due to phase transformations assisted by pipe diffusion and dislocation sweeping mechanisms.

The evolution of microstructures is closely linked to stress corrosion cracking (SCC) and mechanical properties [84,86]. For instance, the dissolution of existing precipitates and in-situ nucleation dominated the formation of new phases, leading to modification in the lattice parameter of the Al [48, 58]. Such changes in precipitate size, chemistry, and phase transformations mainly influence the SCC and mechanical properties [58]. On the other hand, size, interspaces, and chemistry of grain boundary precipitates and the width of PFZs also influence the SCC performances of 7xxx series Al alloy. The discontinuously distributed grain boundary η precipitates and precipitates free zones (PFZs) with less width enhance the SCC performances [84, 86]. On the other hand, continuous distribution with more interspace and large width of PFZs decreases the SCC performances [84, 86]. The interspacing of η in the T6 condition is less than the T73 and T7352 tempers, which gives a high value of Iscc. On the other hand, interspaces and size of η precipitates in the T7352 state are more than that of T6 and T73 tempers, resulting in less Iscc value. The interspacing of η for T73 temper is between the T6 and T7352 tempers, resulting in an intermediate value of Iscc.

Among all the transition precipitates (GP zones, η', and η), the η has a positive corrosion potential value (E°= 1095 mV) concerning α-Al (E° = -767 mV), categorized it anodic by nature [43]. Therefore, the presence of η phase in T6, T73, and T7352 tempers shows a detrimental effect on stress corrosion cracking (SCC) behaviors of alloy. However, at T7352 temper (Fig. 3.26a), dislocation entrapment in the hetero-phase interface of η precipitates and α-Al alters the nature of η from anodic to cathodic. Hence, such phase formation likely improves SCC resistance and a few other mechanical properties [58]. Formation of dense dislocation walls (DDWs), and slip-band structures (Fig. 3.26b and d) in T7352 temper are

characteristic features of the high hardening [60]. The diffracted spots in 2-beam conditions (Fig. 3.26c) also support complex dislocation structure evolution. The diffracted g-vector follows invisibility criteria (g.b.=0), where b displays the Burger vector of α-Al of $a_0/2$[110] type (because close-packed direction, of α-Al, is 110).

The low hardness value of T4 temper (Fig. 3.27) is due to the absence of the transition precipitates (GP zones, η', η). Conversely, the improved hardness for T6 temper arises due to the presence of hard η' and η phases, including the grain boundary precipitates. Low hardness values of T73, and T7352 tempers, concerning T6 (Fig. 3.27) appear due to over-aging. Over ageing, promotes the formation of the coarse, and soft phases. This leads to decreased intensity of the strain field thus reducing the hardness. Additionally, for T7352 temper, application of compressive deformation (~10%) gives lower peak hardening ability, thus reducing the hardness of the alloy. Further, second-stage aging (160°C for 30 hrs) in T7352 temper leads to the formation of soft phases, which may be another possible cause of reduced hardness [33, 38]. More compressive residual stress for T4 temper (-57±8 MPa, Fig. 3.27), in comparison to T6, and T73 (-41± 9 MPa) tempers occur due to the absence of transition precipitates. Reduced compressive residual stress, at T6 temper (-48± 6 MPa) is due formation of transition precipitates (η’ and η). Further reduction at T73 temper (-41± 9 MPa) appears due to two steps of over-aging. Over ageing/ thermal environment reduces the residual stress of alloy [13]. Further, an increase of residual stress at T7352 emerges due to 10% compressive deformation and increased dislocation density assisted precipitation of η precipitates. Gradual increase of hardening behavior for T4 temper (Fig. 3.28) is due to SSSS(α). Moreover, for T6, T73, and T7352 tempers, the gradually increasing trend is due to the presence of metastable precipitates (GP zone, η’ and η, Figs. 3.25c, e,g). The metastable precipitates block the dislocation motion, thus causing strain hardening [33, 60].

Compressive residual stress resists the crack propagation in the α-Al matrix. Consequently, the higher compressive behavior observed in the T7352 temper (-96±9 MPa) is likely to enhance stress corrosion cracking (SCC) resistance and few other mechanical properties in comparison to other heat treatments. The T6 temper shows high yield strength (450±3MPa, Fig.3.28), and ultimate tensile strength (487±7MPa) owing to the presence of fine and evenly distributed η', and η precipitates. At the T7352 temper, a high ultimate tensile strength to yield strength ratio (UTS/YS) was observed, primarily due to the application of 10% compressive deformation. This compression reduces the peak hardening capacity of the material, consequently lowering the yield strength. Additionally, the formation of a soft phase as a result of over-aging further reduces yield strength. Therefore, an increase in ultimate tensile strength, with minimal impact on the yield strength, gives a high UTS to YS ratio. At T4 temper, calculated high dislocation density led to reduced percentage elongation. However, increased percentage elongation in this case arises due to the absence of the second-phase particles. Further, the transition (η', and η) precipitates in the T6 and T73 tempers stop the dislocation motion thus reducing the percentage elongation. The lower elongation at T7352 temper, in comparison to T4 and T73 tempers, is due to 10% compressive deformation, which increases dislocation density in α-Al, thus reducing the elongation.

The best-fitted Swift flow behavior, for T4, T6, and T73 tempers (Figs. 3.29a-c, Table 4) show the presence of pre-strain (ε_0) in materials. Such variations are due to changes in the size and chemistry of precipitates. More pre-strain *(ε_0),* and strain hardening exponent *($n=0.26$)* for T4 temper (Fig. 3.29a, Table 4) emerges due to the absence of precipitates, and single phase super-saturated solid solution (SSSS(α)). The latter causes increased lattice micro-strain thereby pre-strain (ε_0) and hardening exponent of materials. Reduced pre-strain

(ε_0) and hardening exponent (n) for T6 (ε_0 = .0254, n=0.23), and T73 (ε_0 = 0.017, n=0.18) tempers occur due to transition precipitate (η' and η) formation. These decrease supersaturated solute atoms thus reducing pre-strain for T6 and T73 tempers. Less strain hardening rate ($d\sigma/d\varepsilon$, Θ), at the end of stage I, stage II, and stage III for T4 temper alloy (Fig.3.30a, Table 5) is due to the absence of transition precipitates. Slightly high hardening rate (Θ), at T6 temper (Fig. 3.30b) in all stages of transition precipitate formation, including the hardening phases of η' and η' and the soft phases. Further, increased hardening rate (Θ), of T73 temper (Fig.3.30c), in all stages arise due to the absence of GP zone, and increased presence of hardening phases of η' and η. Increased transition true strain (ε) at T6 and T73 tempers (Table 5) in comparison to T4 is due to the presence of transition precipitates which hinder the dislocation motion and shift the transition strain at the higher side. The best fitted Ludwigson flow behavior, for T7352 temper (Fig. 3.30d, Table 5) displays two slope deformation characteristics. Two different strain hardening exponents *(n_1=0.59, n_2= -1.47),* and strength co-efficient *(K_1=695 MPa, K_2=6.02 MPa)*, in the lower and higher strain regime is attributed to two different types of dislocation structure formation (Figs. 3.26a-d). Dislocation loops and forest dislocation are attributed to the low-strain regime. Moreover, the dense dislocation wall (DDW) structure is of the high strain regime. The glide dislocation bypasses with ease from the loops/ forest dislocation and causes less hardening. Moreover, DDWs trap the glide dislocation in dislocation walls thus resulting in high strain hardening exponent (n) by activating the multiple slip system. Another possible cause of high hardening on the higher side may be due to the presence of hardening phases of η' and η. Mehta et al. [68, 70], reported dislocation-assisted two-slope deformation in Ni-based super-alloy, which justifies the current investigation.

The AA7075 subjected to T4, T6, and T73 tempers display three stages of hardening behavior between $ln(d\sigma/d\varepsilon)$ vs. $ln(\varepsilon_0+\varepsilon)$ (Figs. 3.30a-c). The sharp decline in stage I, shows a region of easy glide. This stage relates to a single active slip system and pertains to the formation of dislocation loops, and forest dislocations [36]. Stage I hardening of T4 is above, in comparison to T6, and T73 tempers due to single phase supersaturated solid solution (α) which may cause more hardening effects in the initial stage, followed by the T6 and T73 tempers. The gradual decrease of hardening rate, $(d\sigma/d\varepsilon(\Theta))$, concerning the $ln(\varepsilon+\varepsilon_0)$ in stage II, of T4, T6, and T73 tempers show multiple active slip systems. A sharp decrease in T6 temper, concerning T4 and T73 relates to the formation of the soft phases of Al_2Cu. Moreover, a static decrease of hardening rate (Θ), at T4 and T73 tempers is due to presence of the single-phase supersaturated solid solution (SSSS(α)) and coarse η' and η respectively. Gradual increase of transition strain (ε) in all stages from T4 to T73 arises due to increased precipitates size and interparticle spacing between them. Further, a linear decreasing behavior, in stage III of the T4, T6, and T73 tempers are attributed to the softening stage and pertain to the recovery mechanisms. The cellular dislocation structure is the characteristic feature of this stage [71]. More softening at T4 is due to the absence of precipitates. The gradual decrease of softening, for T6 and T73 tempers occurs due to the presence of hardening precipitates, of η' and η. Least softening at T73 temper emerges due to increased η precipitates. For T7352 temper, a sharp decrease in stage I of hardening rate (Θ, $d\sigma/d\varepsilon$) vs. true plastic strain (ε_p) (Fig. 3.30d) shows a region of easy glide, and single active slip system. The gradual decrease in stage II depicts the multiple active slip system. However, a linear and steady decrease in stage III displays the recovery of materials during plastic deformation. The linear relationship in stage III, between hardening rate $(\Theta, d\sigma/d\varepsilon)$ vs. true plastic strain

(ε_p) could be best explained using the Kock–*Mecking, and Esterin (KME)* [72, 73] based dislocation model, which is given by Eq. 3.17:

$$\Theta_3 = d\sigma/d\varepsilon_p = \Theta_0 + m\sigma \ldots\ldots\ldots\ldots\ldots\ldots\ldots\ldots\ldots\ldots\ldots\ldots Eq.3.17$$

In this equation, Θ_3 is the strain hardening rate, σ is true stress, *m* is the slope of the linear portion, and Θ_0 is the dislocation storage term. The Adj(R^2) value of the linear fitted curve is close to 1 (0.9895), showing one of the best fittings with Eq. 3.17. A high intercept (Θ_0) value depicts high dislocation storage capacity. A more negative slope value (*m = -12967*) is due to less dynamic recovery during plastic deformation. Facet, and dimple fractures, as observed in the under-aged T4 (Fig. 3.31a) alloy, show the brittle and ductile mode of failures, respectively [90,180]. Micro voids, dimples, and trans-granular cracks, at T6 temper (Fig. 3.31b) display ductile failure mode [90,180]. The trans-granular crack is related to failure along the grain boundaries [210]. Similarly, micro-voids and dimples, as shown at T73 temper (Fig. 3.31c), show the ductile failure mode [163]. The gradual increase of dimple size from T4 to T73 (Fig. 3.31a-c) is due to the increased size of precipitates. A slightly decreased dimple size (Fig. 3.31d) at T7352, is due to reduced precipitate size. Moreover, various sizes of microvoids and dimples, and dimple rupture, as shown in Fig. 3.31d (at T7352 temper), support three stages of the deformation characteristics [126]. This could be best explained with the help of nucleation and growth of micro voids and dimples in the first and second-stages. Whereas, evolution of the dimple ruptures in the third-stage. This also shows coalescence of the precipitate particles. High SCC sensitivity in T6 tempers which is less than T73 is due to continuous grain boundary precipitation, but least at 7352 temper is due to dislocation entrapment in the interface of η and the α-Al matrix. The intermediate Iscc of T73 is due to coarse grain boundary η precipitation.

3.5 Conclusions

3.5.1 Part I

1. The Al_3Zr dispersoids co-exist in some of the 220 spots of α-Al.
2. Diffusion-assisted nucleation and growth are responsible for the metastable precipitation of the η' and η.
3. Streaking along the 110 peak of α-Al arises due to diffusion-assisted preferred nucleation of the η precipitates.
4. The η' precipitates are separately nucleated, whereas precipitation of η occurs by the in-situ as well as the separated nucleation mechanisms by changing the lattices at the interface of edges.

3.5.2 Part II

The AA7075T7352 **a**luminum alloy was tensile strained to a true strain corresponding to 0.02, 0.06, and 0.1, and their effects on the precipitation and dislocation behaviors were studied. The findings are summarized below:

5. Dislocation-assisted two-slope deformation characteristics were noted while tensile straining of the AA7075T7352 aluminum alloy. Dislocation loops along with tangled dislocations were formed, at a low amount of tensile straining corresponding to 0.02. Whereas, low- and high-density Taylor-lattice and dislocation cell structures were developed at a higher amount of tensile true straining of 0.06 and 0.1 respectively.
6. Re-arrangement of dislocation is accelerated by the dynamic strain-hardening due to the presence of second phase particles, in the over-aged state.
7. Microstructural inhomogeneities and dissolution of the phases reduce the hardening performance of the alloy. However, the formation of the dislocation tangles, high-density Taylor lattice, and dislocation cell structures at various amounts of tensile

straining helps to activate the multiple slip systems and causes high hardening in the high strain regimes.

8. The η phase partially dissolves during the early stage of tensile straining (0.02). Re-precipitation has been observed at later stages of straining at 0.1.
9. Dissolution of the η'as well as formation, growth, and coarsening of the new precipitates from the dynamically partitioned solute atoms, dislocation entrapment into the η precipitates occurred.
10. The coexistence of Al_3Zr into 220 spots of α-Al is reported in this work. At the low amount of tensile straining, dissolution of the η' occurred, but dynamic precipitations resulted in a higher amount of tensile straining.
11. Microstructural inhomogeneities and dissolution of the phases reduce the hardening performance of the alloy, however, the formation of the dislocation tangles, high-density Taylor lattice, and dislocation cell structures at the various amounts of tensile strain help to activate the multiple slip systems and cause high hardening in the high strain regimes.
12. Dislocation-assisted two-slope deformation characteristics were noted while tensile straining of the AA7075T7352 aluminum alloy. Dislocation loops along with tangled dislocations were formed, at a low amount of tensile straining corresponding to 0.02. Whereas, low and high-density Taylor-lattice and dislocation cell structures were developed at a higher amount of tensile true strain of 0.06 and 0.1 respectively.
13. Re-arrangement of dislocation is accelerated by the dynamic strain-hardening due to the presence of second phase particles, in the over-aged state.

3.5.3 Part III

14. The supersaturated alloy is stable under natural ageing or T4 treatment for at least 3 months. In contrast, metastable (coherent GP zone, semi-coherent η'), and incoherent equilibrium (η) precipitates were formed at T6 temper due to elevated temperature aging but GP zones were absent in T73 tempered condition due to over-aging assisted

dissolution. On the other hand, metastable (η') and equilibrium (η) precipitates were found at T73 temper and their sizes were more as compared to that of T6 condition. However, in the T7352 temper, the η' and η precipitates are formed out of which η' and η are marginally finer than the T73 temper but it is coarser than that of the T6 condition.

15. The T4 tempered material is in soft condition, but hardness reaches a maximum value at T6, due to the presence of a coherent metastable semi-coherent fine η' and equilibrium incoherent η precipitates. On over-aging T73, hardness decreases due to the coarsening of metastable η' and equilibrium η precipitates. The hardness of the T7352 alloy is lower than that of the T73 condition due to changes in precipitate characteristics and the formation of the soft phases
16. The T6 temper alloy displays the highest yield strength (450±3 MPa), ultimate tensile strength (487±7 MPa), and hardness (180±8 Hv) among all the heat-treated alloys due to aging-assisted fine precipitation and their nature. Over-aging reduces strength due to the dissolution of the GP zone and coarsened metastable η' and equilibrium η precipitates.
17. Under-aged, peak-aged, and over-aged alloys display Swift flow behavior ($\sigma = K (\varepsilon_0 + \varepsilon)^n$), even though their work hardening exponents(n), were different: (0.26 for T4), (0.63 for T6), and (0.23 for T73), due to a difference in nature and size of precipitates. Moreover, T7352 temper displays Ludwigson flow behavior. The evolution of two distinct dislocation structures contributes to the two-slope deformation characteristics. The low-strain regime is linked to the development of dislocation loops and forest structures, while dense dislocation walls and slip band structures characterize the high-strain regime.

18. The strain hardening at T4 temper was assisted by the supersaturated solid solution, at T6 by metastable and equilibrium precipitate, and at T73 by coarse (η' and η) as well as over-aging assisted soft phases like Al_2Cu.
19. Three stages of hardening characteristics were observed in the aged alloy, the initial stage high reduction in work hardening rate, followed by a decreased rate of reduction but at the final stage it decreased rapidly. Deformation before peak aging changes the work hardening behavior due to changes in precipitation characteristics and its size and distribution. T7352 temper displays on two slopes in the work hardening rate curve. Initially work hardening rate decreases much rapidly than that of under-aged, peak-aged, and overaged alloys but there after work hardening rate decreases much lower rate but almost constant slope with true plastic strain.
20. Residual stresses in all the heat treatments were compressive. In an as-quenched structure, the residual stress is mostly arising due to rapid quenching. With ageing as precipitation increases stress level decreases marginally up to peak ageing but it continues to reduce significantly on over-aging. On the other hand, T7352 temper reports the highest value of compressive stress due to 10 % compressive deformation before ageing which is not relieved because of low-temperature ageing.
21. The T4 temper displays a mixed mode of ductile-brittle fracture but the T6 temper depicts ductile, and intergranular failures and the overaged T73 and T7352 tempered alloy follow the ductile mode of failure even though the size of the micro-voids and dimples are more as compared to the T6 temper.
22.